E.O. Paton Electric Welding Institute of the National Academy of Science of Ukraine
International Association «Welding»
LLC «Scientific Journals»

The Paton Welding Journal

06
2022

International Scientific-Technical and Production Journal ◊ Founded in January 2000 (12 Issues Per Year)

Address of Editorial Board
E.O. Paton Electric Welding Institute, 11 Kazymyr Malevych Str. (former Bozhenko), 03150, Kyiv, Ukraine
Tel./Fax: (38044) 205 23 90, E-mail: journal@paton.kiev.ua
https://patonpublishinghouse.com/eng/journals/tpwj

State Registration Certificate 24933-14873 ПР from 13.08.2021
ISSN 0957-798X, DOI: http://dx.doi.org/10.37434/tpwj

Subscriptions, 12 issues per year:
$384 — annual subscription for the printed (hard copy) version, air postage and packaging included;
$312 — annual subscription for the electronic version (sending issues in pdf format or providing access to IP addresses).

Representative Office of «The Paton Welding Journal» in China:
China-Ukraine Institute of Welding, Guangdong Academy of Sciences
Address: Room 210, No. 363 Changxing Road, Tianhe, Guangzhou, 510650, China.
Zhang Yupeng, Tel: +86-20-61086791, E-mail: patonjournal@gwi.gd.cn

The content of the journal includes articles received from authors from around the world in the field of welding, metallurgy, material science and selectively includes translations into English of articles from the following journals, published by PWI in Ukrainian:
- Automatic Welding (https://patonpublishinghouse.com/eng/journals/as);
- Technical Diagnostics & Nondestructive Testing (https://patonpublishinghouse.com/eng/journals/tdnk);
- Electrometallurgy Today (https://patonpublishinghouse.com/eng/journals/sem).

CONTENTS

ORIGINAL ARTICLES

*Translated Article(s) from «Automatic Welding», No. 5, 2022.

**Translated Article(s) from «Electrometallurgy Today», No. 1, 2021.

***Translated Article(s) from «Technical Diagnostics & Nondestructive Testing», No. 2, 2022.

https://doi.org/10.37434/tpwj2022.06.01

INFLUENCE OF MICROALLOYING WITH BORON ON THE STRUCTURE AND PROPERTIES OF DEPOSITED METAL OF THE TYPE OF TOOL STEEL 25Kh5FMS

A.A. Babinets, I.O. Ryabtsev, I.P. Lentyugov, I.L. Bogaichuk

E.O. Paton Electric Welding Institute of the NASU
11 Kazymyr Malevych Str., 03150, Kyiv, Ukraine

ABSTRACT

In the work, the influence of different amounts of boron microadditives on the structure and operational properties of metal of the type of tool steel 25Kh5FMS, produced by arc surfacing using the experimental flux-cored wires, was experimentally determined. Microalloying additives were introduced directly into the charge of experimental flux-cored wires during their manufacture. It was found that microalloying of the deposited metal of the type of steel 25Kh5FMS with boron in the amount of 0.007–0.04 % does not deteriorate the quality of deposited beads formation and separation of the slag crust. At the same time, when the boron content in the deposited metal is ≥ 0.02 %, the formation of a large number of crystallization cracks is observed, which has an extremely negative effect on its operational properties. Moreover, it was experimentally found that the introduction of boron microadditives in the amount of 0.007–0.01 % to the deposited metal of the type 25Kh5FMS leads to an increase in its heat resistance and wear resistance at elevated temperatures by 1.2–2.0 times. With an optimal content of microalloying additives, a refinement of the structure of the deposited metal, some increase in microhardness and, probably, the formation of complex spherical carboborides in the alloy matrix occur. In view of the obtained data, it is recommended to use boron in the deposited metal of the type of tool steel 25Kh5FMS in the amount of 0.007–0.01 % in order to improve its operational properties.

KEYWORDS: arc surfacing, microalloying, deposited metal, flux-cored wire, wear resistance, heat resistance, microstructure

INTRODUCTION

Nowadays, in our country and abroad, a large number of materials in the form of solid and flux-cored wires, strips and coated electrodes for arc surfacing of parts of machines and mechanisms, operated in the conditions of different types of wear, cyclic mechanical and thermal loads, corrosion, etc., were developed [1–5]. In essence, the technical and economical capabilities to increase the operational properties of the deposited metal by conventional additional alloying of electrode materials are almost exhausted.

Great opportunities in the control of the structure and properties of the deposited metal are opened up by the use of microalloying and modification, which have almost not been used in surfacing production until now [6, 7]. Only certain works are known, mainly aimed at solving practical problems, such as, for example, for surfacing of propeller shafts of sea vessels [8] and other pasrts [9–11].

The aim of the work was to investigate the effect of boron microalloying on the structure and operational properties of metal of the type of tool semi-heat-resistant steel 25Kh5FMS, produced by arc surfacing using flux-cored wires with a charge containing microalloying additives.

MATERIALS USED TO CONDUCT STUDIES

For the experiments, a charge composition was calculated and four experimental flux-cored wires for surfacing were manufactured, which provide a deposited metal of the type of tool steel 25Kh5FMS. As a microalloying additive, FKhB-1 master alloy was used, which contains 12 % of boron. This master alloy in the form of powder was added directly to the charge of flux-cored wires during their manufacture with such calculation as to obtain the boron content in the charge of flux-cored wires from 0.01 to 0.1 %. As was shown in [6], such a method of introducing microalloying or modifying additives from a technological and economic point of view is the simplest and most rational in arc surfacing. As a reference, the flux-cored wire PP-Np-25Kh5FMS was used without adding microalloloying additives. The diameter of all designed wires is 1.8 mm, the fill factor is 25 %. Surfacing of the experimental specimens was performed under the flux AN-26P.

PROCEDURES AND SPECIMENS FOR CONDUCTING STUDIES OF OPERATIONAL PROPERTIES OF DEPOSITED METAL

Hot deforming tools during operation are mainly worn as a result of friction of metal against metal at elevated temperatures. In addition, as a result of periodic con-

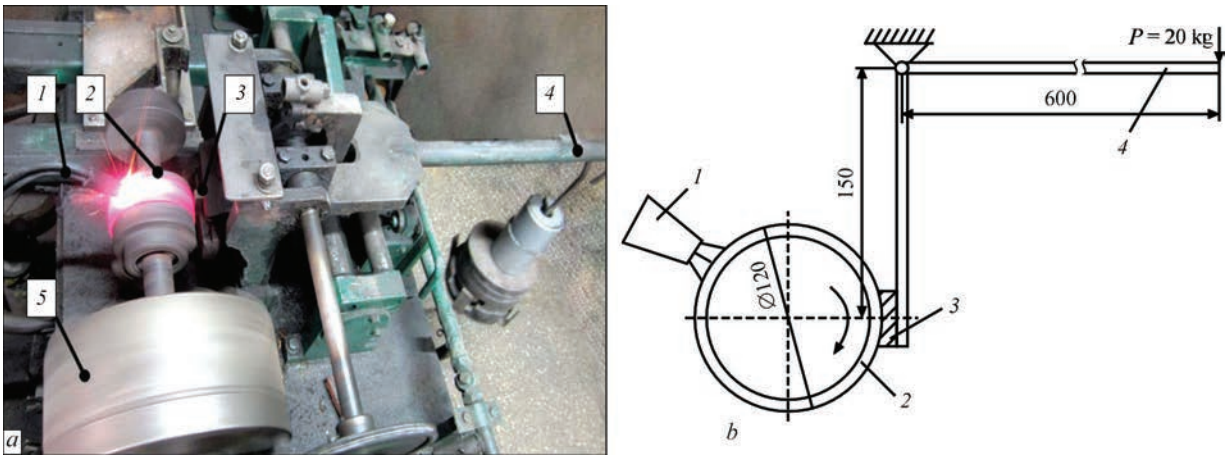

Figure 1. Appearance (*a*) and schematic diagram (*b*) of the installation unit for studying wear resistance of the deposited metal in friction of metal against metal at elevated temperatures: *1* — gas torch for heating of the ring (counterbody), which wears out the specimen; *2* — ring (counterbody); *3* — worn specimen; *4* — lever with loads for clamping the specimen to the ring (counterbody); *5* — drive for rotation of the ring (counterbody)

tact with the workpieces heated to high temperature, in the deposited metal, thermal fatigue cracks may occur. To conduct studies of wear-resistance during friction of metal against metal at elevated temperatures and thermal resistance of the deposited metal, an experimental block-module installation was used [12].

PROCEDURE FOR STUDYING WEAR IN FRICTION OF METAL AGAINST METAL AT ELEVATED TEMPERATURES

The main research parameters include specific pressure on a tested deposited specimen, heating temperature of this specimen, speed of relative movement of friction elements (friction rate), material of the ring (counterbody), which wear out the specimen, heating temperature of the ring.

In Figure 1, *a* the photo of the installation unit, and in Figure 1, *b* principal scheme of studying wear resistance of the deposited metal in friction of metal against metal at elevated temperatures are shown. The correlation of the shoulders of the lever mechanism at a load of 20 kg provides clamping of the specimen to the ring, which wears the specimen with a force of 800 N. When the cylindrical surface of the heated ring gets in contact with the plane of the specimen, the pressure at the point of contact is determined by the formula

$$P_{cl} = 0.798\sqrt{\frac{\rho}{D\left(\frac{1-\mu^2}{E_1}+\frac{1-\mu^2}{E_2}\right)}},$$

where $\rho = P/l$; P is the clamping force (800 N); l is the width of the specimen (10 mm); D is the diameter of the ring (120 mm).

Accepting the values of the Poisson's ratio and elasticity modules for heated steel and tested specimen equal respectively to $\mu = 0.3$; $E_1 = 25000$ MPa; $E_2 = 20000$ MPa, we obtain the value of specific pressure of 100 MPa. The friction rate was 20–22 m/min, which corresponds to the most used modes during hot deformation of metals.

The ring, which wears out the specimen, was heated by oxyfuel flame. Due to a rough certain ratio of gas and oxygen consumption, the temperature of the ring was maintained by constant — 950–980 °C, which was periodically controlled by means of the optical pyrometer. The temperature on the surface of the specimen in the area of contact of the specimen and the ring was approximately 600 °C. The wear resistance of the specimen is determined by weight loss before and after the test, the average value of which is calculated by three specimens of one type.

PROCEDURE OF RESEARCH OF DEPOSITED METAL THERMAL RESISTANCE

During evaluation of heat resistance, the cycles of heating and cooling of the deposited specimens were repeated till the initiation of thermal fatigue cracks or achieving a certain degree of cracking. In this case, the degree of thermal stability is a number of cycles before achieving these values. The installation unit for the study of heat resistance of the deposited specimens is shown in Figure 2.

The specimen being investigated is installed in the frame of the installation so that its deposited polished surface is directed to the heating source, in capacity of which, a oxyfuel torch is used. The reciprocating motion drive provides movement of the mandrel with a specimen fixed in it from the heating source to the place, where the specimen is cooled with water.

A uniform heating by the gas torch is successful in the spot on the surface of the specimen with a diameter of ≈ 15–20 mm. The heating lasts 12 s,

the cooling with a jet of water lasts 8 s. Under these conditions, the heating temperature of the specimen surface is stabilized before the 10th cycle and is in the range of 630–690 °C. Cooling of the specimen with water is carried out to 60–80 °C. The heating-cooling cycles are repeated before the appearance of the network of thermal cracks visible with a naked eye, after which the test was stopped, the deposited surface of the specimen was cleaned and photographed.

After that, to determine the depth and nature of propagation of thermal cracks in the deposited metal, the specimens of all types were continuously loaded by the cycles of heating-cooling until reaching 200 test cycles. Then, the specimens were cut perpendicular to the deposited surface, macrosections were made and the depth of crack propagation was measured. As a result, the heat resistance of each type of the deposited specimen was evaluated by two values — a number of cycles before appearance of a network of cracks, and the depth of their propagation upon reaching 200 cycles of heating-cooling. The determination of both values was calculated as an average value of three specimens of one type.

Metallographic examinations of the specimens of the deposited metal were performed according to standard methods. The specimens were prepared on high-speed polishing wheels using diamond pastes of different dispersion. The structure of the deposited metal was detected by electrolytic etching in a 20 % aqueous solution of chromic acid. Microstructure examinations were carried out in the metallographic optical microscope Neophot-32 at a magnification ×200. The hardness of phase components was measured in the M-400 microhardness meter of Leco Company, the load was 1 N, the load time was 10 s. Digital images of microstructures were obtained using the Olympus C-500 camera. The depth of thermal cracks was determined on produced macrosections in the metalographic MIM-7 microscope, equipped by the digital video eyepiece SIGETA MCMOS 3100 at a magnification ×90.

MANUFACTURE OF SPECIMENS, CONDUCTING EXPERIMENTAL STUDIES AND DISCUSSING THEIR RESULTS

To determine the impact of boron microalloying on welding and technological properties of flux-cored wires and the quality of the deposited metal formation, electric arc surfacing using experimental flux-cored wires PP-Np-25Kh5FMS on plates of 40Kh steel was performed. The surfacing of all specimens was performed under the flux AN-26P at the same mode: current — 220–230 A, voltage — 36–37 V, deposition rate — 25 m/h. The surfacing was performed with single beads with an overlapping of approximately 50 %. In order to avoid the effect of mixing base metal, surfacing of each specimen was performed in four layers.

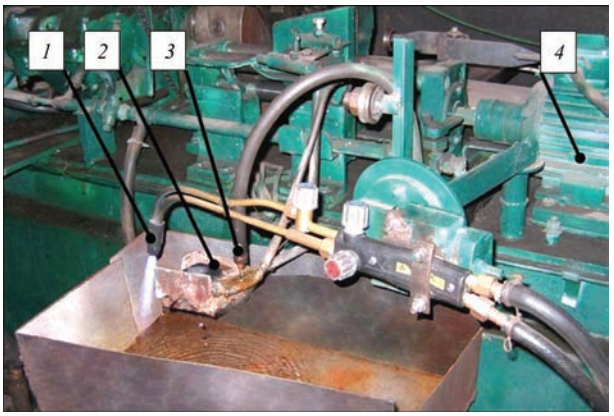

Figure 2. Appearance of the installation unit for studying heat resistance of the deposited specimens: *1* — gas torch for heating of the specimen; *2* — tested specimen; *3* — hose for supplying water that cools the specimen; *4* — drive for movement of the specimen

The appearance of the specimens after surfacing is shown in Figure 3, *a*, from which it is seen that the quality of metal formation deposited by all experimental wires is almost the same. The quality of slag crust separation in all cases was also at the same level and was satisfactory. After surfacing, the surface of the specimens was polished and investigated for the presence of pores, cracks and other defects (Figure 3, *b*). From the deposited specimens, templates were also cut out and transverse macrosections were prepared (Figure 4).

From the abovementioned figures it is seen that in all the deposited specimens the fusion line is clear, defects in the form of lacks of fusion, pores, etc. are absent. However, ≥ 0.02 % increase in boron content leads to the appearance of crystallization cracks in the deposited metal, which mostly pass through all the deposited layers and reach the base metal, but do not go into it.

Table 1 shows the data of X-ray spectral analysis of the boron content in the deposited metal, as well as the impact of boron microalloying on its hardness (specimens Nos 1–4). It was experimentally determined that in submerged-arc surfacing by flux-cored wires containing FKhB-1 master alloy, up to 70 % of boron goes into the deposited metal, which leads to a gradual increase in hardness of the deposited metal of the type of steel 25Kh5FMS. The additions of FKhB-1 master alloy do not deteriorate its welding and technological characteristics and do not affect the quality of the deposited metal formation and separation of the slag crust. At the same time, as is noted above, at a boron content in the deposited metal being ≥ 0.02 %, the appearance of a large number of cracks was noted.

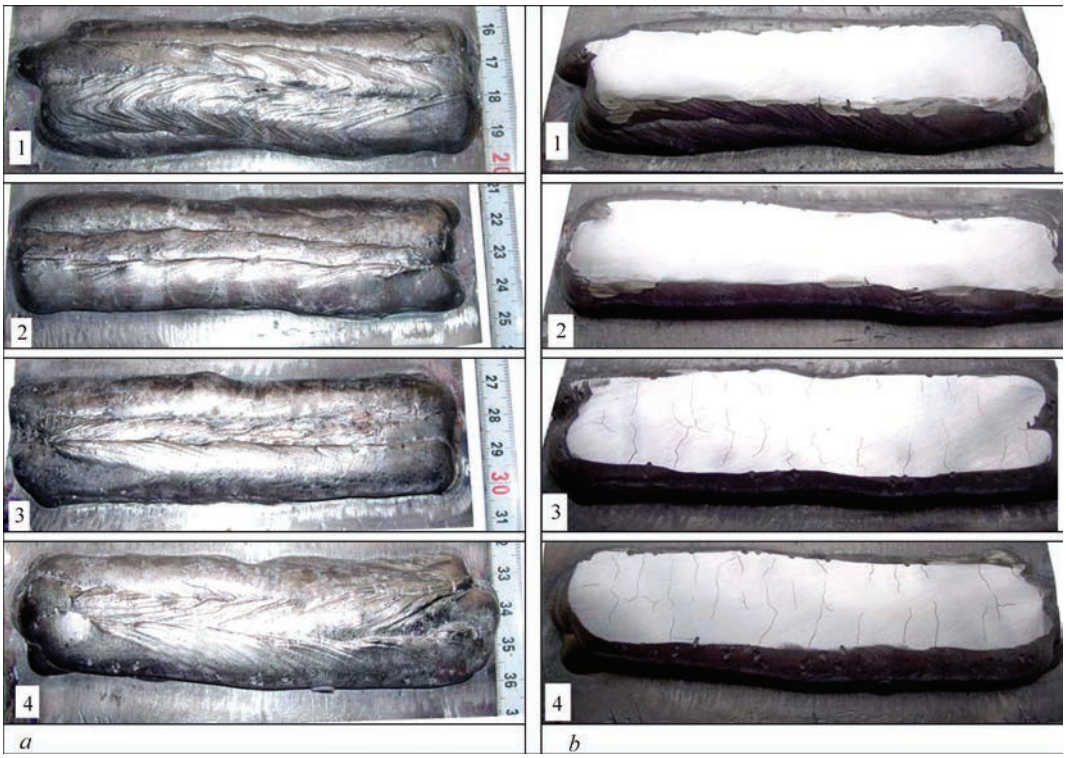

Figure 3. Appearance of the specimens of steel 40Kh after surfacing (*a*) and mechanical treatment (*b*). Boron content in the deposited metal, %: *1* — 0; *2* — 0.007; *3* — 0.02; *4* — 0.04

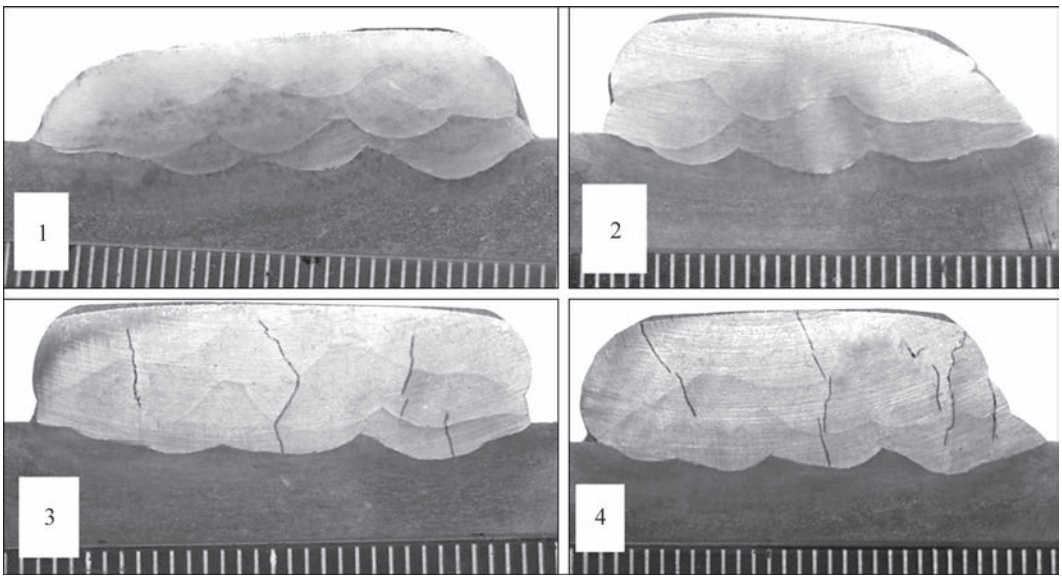

Figure 4. Transverse cross-sections of the deposited metal with different boron content, %: *1* — 0; *2* — 0.007; *3* — 0.02; *4* — 0.04

Table 1. Hardness of metal, deposited using experimental flux-cored wires of the type PP-Np-25Kh5FMS with different boron content

Specimen number	Mass fraction of boron in the deposited metal, %	Hardness of the deposited metal
1	–	50–54
2	0.007	54–55
3	0.02	54–56
4	0.04	55–57

Metallographic examinations of metal of the type of steel 25Kh5FMS, deposited by experimental flux-cored wires, showed that the structure of the deposited metal in its central part in the specimens of all types is cast, consists of columnar crystallites oriented in the direction of heat removal (Figure 5). The width of crystallites in the studied specimens is slightly different and has the following sizes: specimen No. 1 — 40–45 μm; specimen No. 2 — 20–22 μm; specimen No. 3 — 18–20 μm; specimen No. 4 — 15–20 μm. Thus, the introduction of boron microadditives into

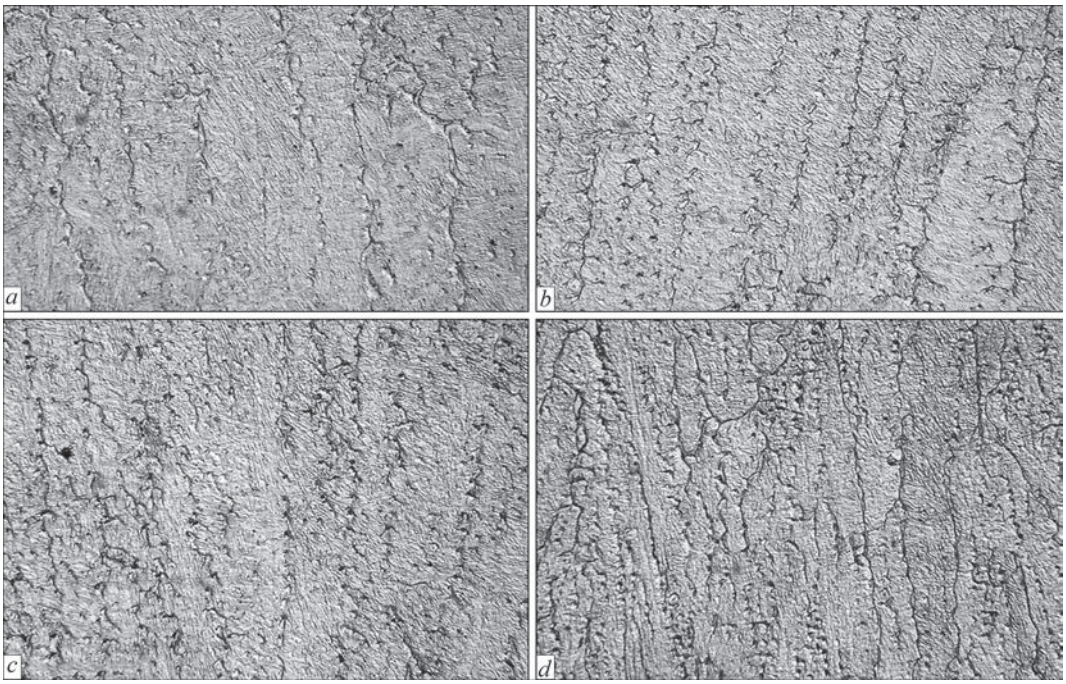

Figure 5. Microstructure (×200) of the central part of the deposited metal with different boron content, %: *a* — without boron; *b* — 0.007; *c* — 0.02; *d* — 0.04

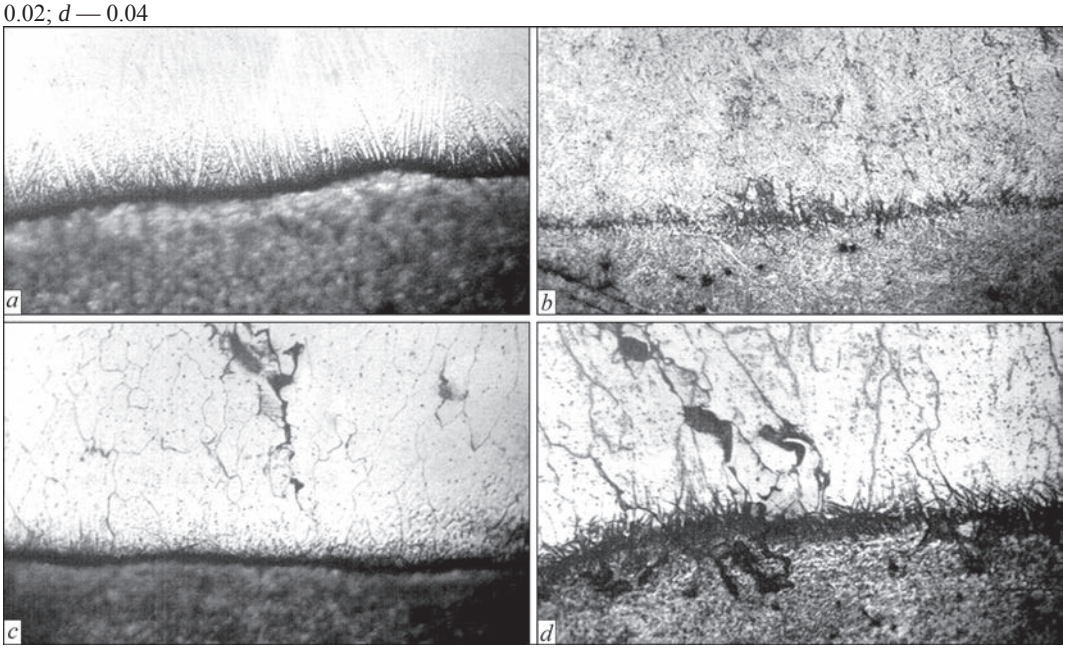

Figure 6. Microstructure (×200) of metal near the fusion line (top) and base metal (bottom) with different boron content, %: *a* — without boron; *b* — 0.007; *c* — 0.02; *4* — 0.04

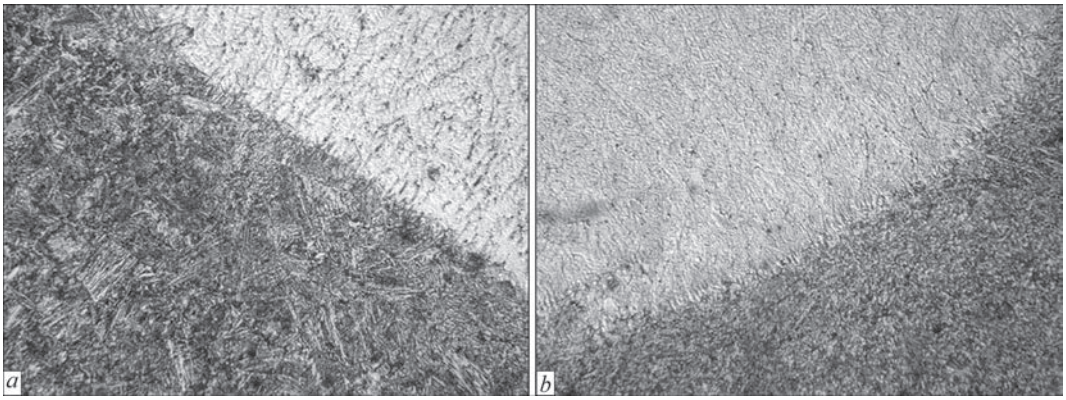

Figure 7. Microstructure (×200) of the deposited metal containing $B = 0.007$ % near the fusion line and HAZ (description *a*, *b* — see in the text)

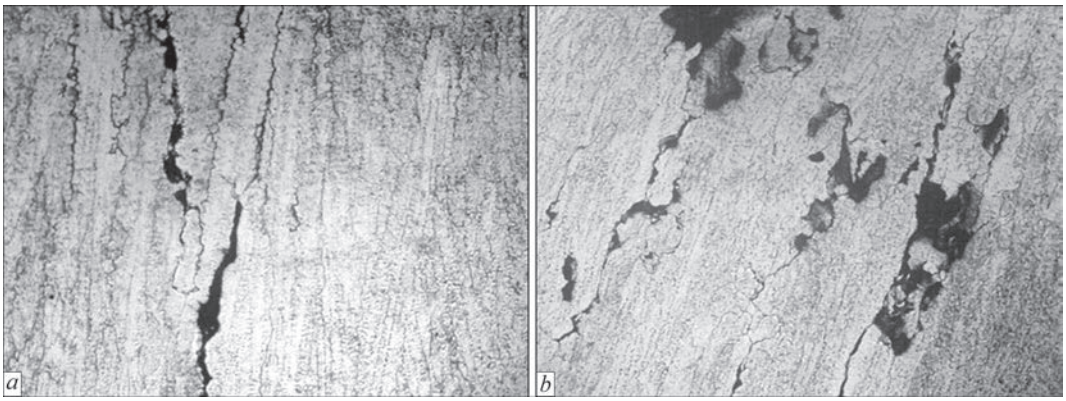

Figure 8. Microstructure (×200) of regions of a central part of the deposited metal with the boron content: *a* — 0.02 %; *b* — 0.04

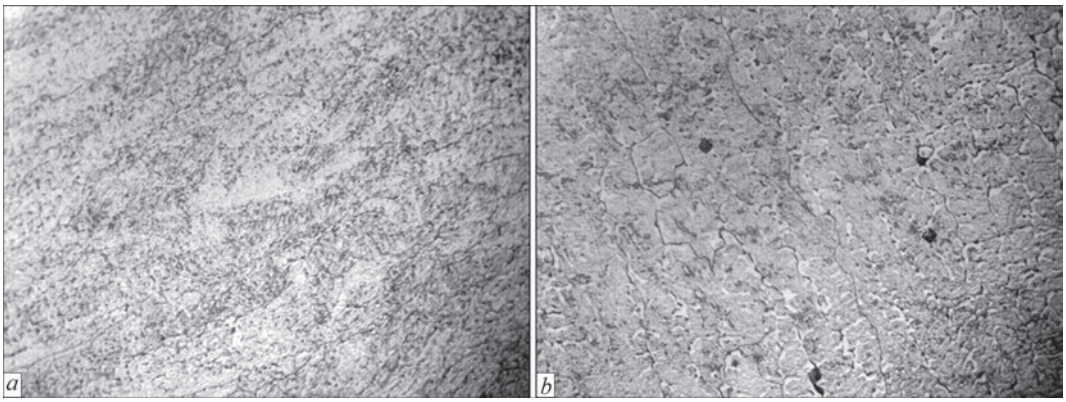

Figure 9. Microstructure (×200) of the upper part of the deposited metal in the specimens with the boron content: *a* — 0.02 %; *b* — 0.04

the deposited metal in the amount of up to 0.04 % leads to refinement of the microstructure of metal and reduction in the average grain size by 2.2–2.5 times.

Microstructure of the matrix is fine acicular martensite (Figure 5). In the specimens, microalloyed by boron, in the lower part of the deposited metal, closer to the fusion line, separate regions with coarser needles are observed (needles up to 50 μm) (Figure 6, *b*–*d*), the hardness of these regions is the same as the hardness of other zones of the deposited metal.

In the boundaries of crystallites in the structure of all studied specimens, smooth light precipitates are observed, which probably represent an alloyed austenite. The hardness of these precipitates amounts to *HV*1 — 6340–6420 MPa. Specimen No. 2 has the smallest number of such precipitates, and the specimen No. 4 has the largest one.

The structure of HAZ in the specimen No. 2 (0.007 % B) on the overheating area represents ferrite and pearlite (Figure 7, *a*). In HAZ some sections are observed, where the overheating area is absent, and on the side of base metal, the dispersion region of recrystallization is observed with fine-grained ferrite-pearlite structure (Figure 7, *b*), the metal hardness of which amounts to *HV*1 2380–2450 MPa. This structure is formed during repeated heating in the process of successive deposition of beads.

Defects on the fusion line and in HAZ in the specimens No. 1 (without B) and No. 2 (0.007 % B) were not detected. In the specimens Nos 3, 4 near the fusion line, a large number of microcracks was noted (Figure 6, *c*, *d*), which mostly pass along the boundaries of grains and propagate further into the deposited metal. As the boron content increases, a number of cracks and their size grow (Figure 8). The presence of precipitates of rounded shape in the body of crystallites also should be noted, which are probably complex carboborides. A number of these precipitates also grows with an increase in the boron additive content in the deposited metal (Figure 9).

Table 2. Microhardness of areas of metal, deposited using experimental flux-cored wires with different boron content

Area of deposited metal	Microhardness (*HV*1) with boron content:			
	– (Specimen No. 1)	0.007 % (Specimen No. 2)	0.02 % (Specimen No. 3)	0.04 % (Specimen No. 4)
Top	5720–6420	6130–6420	6420–7240	6490–7240
Center	5420–6420	5720–6490	5920–6630	6060–6420
Bottom	5660–5720	5480–5720	6060–6420	6130–7070

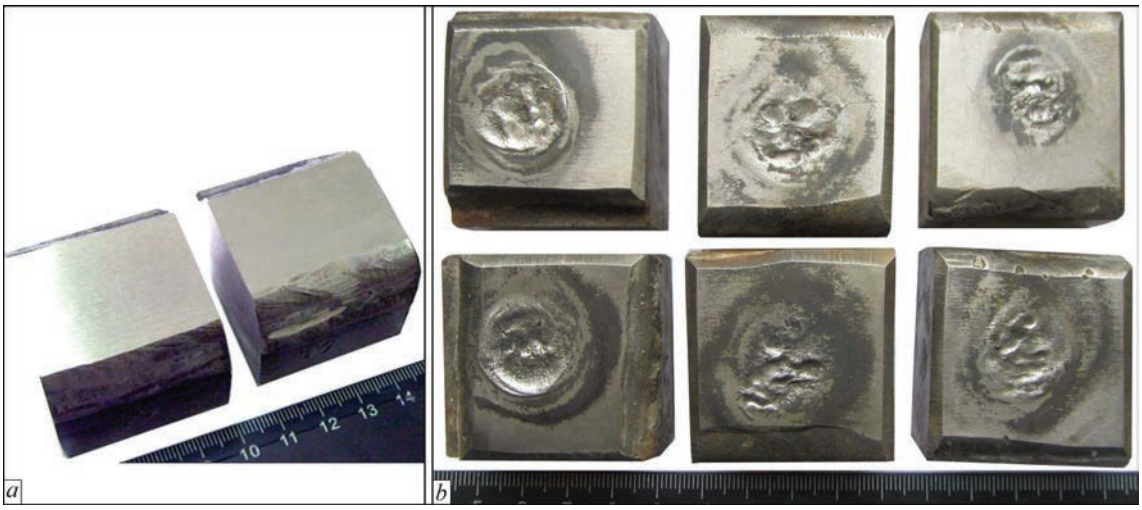

Figure 10. Appearance of the specimens for studying heat resistance of the deposited metal before (*a*) and after tests (*b*)

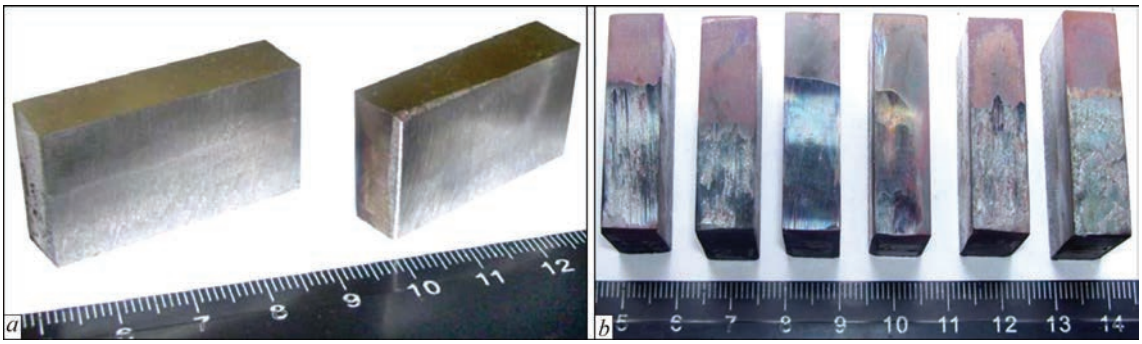

Figure 11. Appearance of the specimens for studying wear resistance of the deposited metal at elevated temperature before (*a*) and after tests (*b*)

An increase in the boron content in the deposited metal from 0.02 to 0.04 % leads to some increase in the microhardness of its matrix all over the volume of the deposited metal (Table 2).

Thus, microalloying of the deposited metal of the type of steel 25Kh5FMS by boron in the amount of 0.007–0.04 % leads to a significant refinement of the microstructure of the deposited metal and an increase in the microhardness of its matrix. At the same time, when the content of boron in the deposited metal is ≥ 0.02 %, microcracks begin to appear in it, which propagate from the fusion line with the base metal and pass through all the layers of the deposited metal. As the boron content grows to 0.04 %, a number and the branching of these cracks increases significantly.

Taken the abovementioned into account, while studying the impact of boron microalloying on the operational properties of the deposited metal, it was decided to limit the maximum boron content in the deposited metal at the level of 0.01 % to avoid cracking and reduce the operational properties of the deposited metal.

Surfacing of the specimens to determine thermal fatigue resistance was performed by single beads with overlapping of 40–50 % on the workpieces with the sizes 20×40×200 mm. For the manufacture of specimens to study the resistance of the deposited metal under the conditions of friction of metal against metal at elevated temperature, surfacing by single beads without overlapping on the end of the workpieces with the sizes of 15×25×200 mm was performed. Such surfacing technique was chosen based on the sizes and design of the specimens to determine the operational characteristics of the deposited metal according to the developed procedures of experimental studies.

Table 3. Results of studying heat resistance of the deposited metal (average values)

Specimen number	Number of cycles before appearance				Depth of cracks, mm	
	Of first crack	Of new cracks	Fine network of cracks	Propagated network of cracks	Medium	Maximum
1	70	100	140	175	0.07	0.13
2	100	130	170	200	0.04	0.07

Table 4. Results of studying wear resistance at elevated temperatures (average values)

Specimen number	Loss of mass, g	
	Of deposited specimen	Of ring (counterbody)
1	0.456	5.4
2	0.373	2.8

The specimens for studying thermal stability of the deposited metal had the sizes of 40×40×30 mm. Moreover, the heated surface had the sizes of 40×40 mm. The specimens for studying wear resistance at elevated temperatures had the sizes of 10×17×40 mm. Moreover, a wear surface had the sizes of 10×17 mm. The appearance of the specimens before and after studies of heat resistance and wear resistance is shown in Figures 10 and 11, and the results of these studies are presented in Tables 3 and 4, respectively.

Microalloying of the deposited metal 25Kh5MFS by boron in the range of 0.007–0.01 % has a positive effect on heat resistance of the deposited metal of the type 25Kh5FMS. Thermal fatigue cracks in the metal of the deposited specimen microalloyed by boron, are initiated later, their average length and number is smaller than in the reference specimen. Also the positive effect of boron microalloying on wear resistance of metal in friction of metal against metal at elevated temperatures was noted — losses of weight of the specimen and the ring (counterbody), which wears out the specimen, decrease by 1.2 and 2.0 times respectively.

CONCLUSIONS

1. Microalloying of the deposited metal of the type 25Kh5FMS by boron in the range of 0.007–0.01 % leads to a significant refinement of its microstructure and some increase in the microhardness of its matrix. In this case, an increase in the boron content in the deposited metal being $\geq$ 0.02 % leads to the formation of a large number of crystallization cracks in it, that propagate through all the layers of the deposited metal.

2. Microalloloying of the deposited metal 25Kh5MFS by boron in an amount of 0.007–0.01 % increases its heat resistance and wear resistance at elevated temperatures by 1.4–1.75 and 1.2–2.0 times, respectively, which can be explained mainly by refinement of its microstructure and an increase in the microhardness of its matrix.

REFERENCES

1. Ryabtsev, I.A., Senchenkov, I.K., Turyk, E.V. (2015) *Surfacing. Materials, technologies, mathematical modeling*. Gliwice, Wydawnictwo Politechniki Śląskiej.
2. Kondratiev, I.A., Ryabtsev, I.A. (2014) Flux-cored wires for surfacing of steel hot mill rolls. *The Paton Welding J.*, **6–7**, 95–96. DOI: https://doi.org/10.15407/tpwj2014.06.20
3. Zhudra, A.P., Voronchuk, A.P. (2012) Cladding flux-cored strips (Review). *The Paton Welding J.*, **1**, 34–38.
4. Bely, A.I., Zhudra, A.P., Dzykovich, V.I., Petrov, V.V. (2018) Electrodes for arc hardfacing of composite alloys. *The Paton Welding J.*, **1**, 29–32. DOI: https://doi.org/10.15407/tpwj2018.01.06
5. Student, M.M., Voytovych, A.A., Sirak, Ya.Ya., Gvozdetskyi, V.M. (2020) Development of new electrode materials, methods of restoration and protection of thin-walled parts of equipment, which are operated under the conditions of abrasive and gas-abrasive wear. *The Paton Welding J.*, **10**, 31–34. DOI: https://doi.org/10.37434/tpwj2020.10.06
6. Babinets, A.A., Ryabtsev, I.O. (2021) Classification of methods of modification and microalloying of deposited metal (Review). *The Paton Welding J.*, **9**, 2–8. DOI: https://doi.org/10.37434/tpwj2021.09.01
7. Babinets, A.A., Ryabtsev, I.O. (2021) Influence of modification and microalloying on deposited metal structure and properties (Review). *The Paton Welding J.*, **10**, 3–10. DOI: https://doi.org/10.37434/tpwj2021.10.01
8. Gladky, P.V., Mikaelyan, G.S. (2015) *Microalloying and modification of wear-resistant deposited metal.* In: *Surfacing. Technologies, materials, equipment.* Kyiv, PWI, 71–73 [in Russian].
9. Stepnov, K.K., Matvienko, V.N., Oldakovsky, A.I. (2011) Modification of medium-chromium deposited metal. *The Paton Welding J.*, **8**, 10–12.
10. Krivchikov, S.Yu. (2012) Modification by boron of deposited metal of white cast iron type. *The Paton Welding J.*, **6**, 19–21.
11. Hou, Q.Y., Huang, Z., Wang, J.T. (2011) Influence of nano-Al_2O_3 particles on the microstructure and wear resistance of the nickel-based alloy coating deposited by plasma transferred arc overlay welding. *Surf. Coat. Technol.*, 206(**8–9**), 2806–2812. DOI: https://doi.org/10.1016/j.surfcoat.2010.10.047
12. Ryabtsev, I.I., Chernyak, Ya.P., Osin, V.V. (2004) Modular unit for testing of deposited metal. *Svarshchik*, **1**, 18–20 [in Russian].

ORCID

A.A. Babinets: 0000-0003-4432-8879
I.O. Ryabtsev: 0000-0001-7180-7782,
I.P. Lentyugov: 0000-0001-8474-6819

CONFLICT OF INTEREST

The Authors declare no conflict of interest

CORRESPONDING AUTHOR

I.O. Ryabtsev
E.O. Paton Electric Welding Institute of the NASU
11 Kazymyr Malevych Str., 03150, Kyiv, Ukraine.
E-mail: ryabtsev39@gmail.com

SUGGESTED CITATION

A.A. Babinets, I.O. Ryabtsev, I.P. Lentyugov, I.L. Bogaichuk (2022) Influence of microalloying with boron on the structure and properties of deposited metal of the type of tool steel 25Kh5FMS. *The Paton Welding J.*, **6**, 3–10.

JOURNAL HOME PAGE

https://pwj.com.ua/en

Received: 26.05.2022
Accepted: 15.08.2022

https://doi.org/10.37434/tpwj2022.06.02

FORMATION OF COMPOSITE COATINGS BY THE METHOD OF SUPERSONIC PLASMA SPRAYING OF POWDERS BASED ON TiAl INTERMETALLIC WITH NON-METALLIC REFRACTORY COMPOUNDS SiC AND Si_3N_4

Yu.S. Borysov, N.V. Vihilianska, M.V. Kolomytsev, K.V. Iantsevych, O.M. Burlachenko, T.V. Tsymbalista

E.O. Paton Electric Welding Institute of the NASU
11 Kazymyr Malevych Str., 03150, Kyiv, Ukraine

ABSTRACT

Studies of the structural-phase state, erosion and corrosion resistance of coatings of TiAl-SiC and TiAl–Si_3N_4 systems, produced by the method of supersonic air-gas plasma spraying, are presented. As materials for spraying, composite powders, produced by the method of mechanic and chemical synthesis based on TiAl intermetallic with the addition of non-metallic refractory compounds SiC and Si_3N_4 were used. Comparison of the phase composition of the produced coatings of TiAl-SiC and TiAl–Si_3N_4 systems with the phase composition of the composite powder after mechanic and chemical synthesis indicates proceeding of processes of interaction of TiAl with non-metallic refractory compounds, as a result of which the phases of SiC and Si_3N_4 are not observed in the coating. Due to the presence of strengthening phases in the coatings, the erosion resistance of the composite coatings increases by 1.3–1.5 times as compared to TiAl intermetallic coating. Electrochemical tests found that the coatings of TiAl—SiC and TiAl–Si_3N_4 systems are capable to provide the protection of steel, aluminium and titanium base in the environment containing sodium chloride with an increase in resistance by 5–155 times. On the basis of the conducted studies of functional properties of the developed composite coatings, the possibility of their use for the protection of parts subjected to erosive wear and corrosion is shown.

KEYWORDS: intermetallic, non-metallic refractory compound, supersonic air-gas plasma spraying, structure, phase composition, erosive wear, corrosion resistance

INTRODUCTION

Owing to low density, high specific strength, resistance to environmental impact, heat strength and heat resistance, titanium aluminides are used as materials in the manufacture of some components in automotive and aircraft industries, such as turbocompressors, cars turbocharges, blades of low-pressure turbines, etc. [1]. However, the main disadvantages that limit the widespread practical use of titanium aluminides, are their brittleness, low plasticity and crack resistance in a wide temperature range, and increased ductility complicates the use of TiAl alloys in the conditions of friction of surfaces being in contact [2].

In order to increase the physical and mechanical properties of products, composite materials are developed based on TiAl systems — non-metallic refractory compound (NRC) (e.g. B_4C, SiC, etc.), for whose production mainly the methods of powder metallurgy — hot isostatic pressing, reaction sintering and high-temperature synthesis are used [3, 4].

To produce TiAl-based coatings, vacuum deposition methods, such as magnetron, cathode-arc, electron beam and ionic deposition, have become the most widespread. Magnetron coatings of TiAl-BN system increase the wear- and heat resistance of a product as compared to TiAlN coatings [5]. Coatings of TiAl–SiC system, produced by electron beam deposition, have an increased resistance to cyclic oxidation due to a high adhesion between the coating and the base [6]. Coatings of TiAlSiN system, produced by cathode-arc, magnetron and ionic deposition, have high strength, microhardness and wear resistance [7, 8].

A challenging direction in producing protective coatings based on TiAl intermetallic is thermal spraying, which, unlike vacuum methods for deposition of coating, allows depositing coatings with the thickness of few millimeters. In addition, thermal spraying methods allow repairing local damages of parts that failed prematurely as a result of corrosion, erosion, abrasive wear or fatigue.

TiAl-based thermal coatings are produced by the methods of plasma, supersonic plasma, high-velocity oxyfuel and cold gas dynamic spraying [9]. It is possible to increase the resistance to oxidation and mechanical properties of coatings based on TiAl binary alloy by adding alloying elements such as Cr, Si, V, Nb, W, Mo or Ta, [9]. The use of composite coatings based on TiAl alloy with the addition of non-metallic refractory compounds such as SiC and Al_2O_3 components as strengthening components, allows increasing the hardness and wear resistance of titanium alloy

parts, while the wear resistance of composite coatings is 2.5 times higher than the resistance of TiAl intermetallic [10]. As spraying materials, composite powders are used, produced by mechanical alloying.

At present, the problems of increasing the reliability of operation of parts of gas turbine engines and elements of gas-compressor units, which during operation are prone to damages of both from the physical, in particular, erosion exposure of the dust-gas flow as well as from chemical effects: corrosion at high (turbine parts) and low temperatures (compressor parts, engine harness).

The aim of the work is the study of structure, phase composition and properties (erosion and corrosion resistance) of composite coatings based on titanium aluminides of TiAl–SiC and TiAl–Si_3N_4 systems, produced by the method of supersonic air-gas plasma spraying.

RESEARCH MATERIALS AND PROCEDURES

For supersonic air-gas plasma spraying (SAGPS) of coatings, powders based on TiAl intermetallic of TiAl–SiC and TiAl–Si_3N_4 systems were used. Composite powders were produced by the method of mechanochemical synthesis (MChS) of TiAl (PVT65Yu35), SiC and Si_3N_4 powders in the planetary mill within 1.5 h. The composition of initial mixtures of powders was chosen on the basis of thermodynamic calculations with the determination of the most probable reactions of interaction of titanium intermetallic with non-metallic refractory compounds (SiC and Si_3N_4):

- 88 TiAl + 12 SiC = 18 TiC + 32 Ti_5Si_3 + 50 $TiAl_3$ (wt.%);
- 83 TiAl + 17 Si_3N_4 = 8 TiN + 40 Ti_5Si_3 + 15 AlN + + 37 $TiAl_2$ (wt. %).

To provide a uniform feed of powder to the plasma jet before spraying, the powders were conglomerated by a 5 % solution of polyvinyl alcohol with a subsequent screening of particles with a size range of 40–63 μm. For comparison, a coating from initial TiAl powder was also sprayed. The characteristics of the powders used in the work are given in Table 1.

The spraying was carried out in the installation Kyiv-S for supersonic air-gas plasma spraying using the following technological parameters: current I = 230 A, voltage U = 380 V, consumption of plasma forming gas (air) Q_{pg} = 20 m^3/h, spraying distance L = = 160 mm. The coatings for investigations were deposited on the specimens made of St3.

Table 1. Characteristics of powders for SAGPS-coatings

Composition, wt.%	Particle size, μm	Phase composition
65Ti–35Al	<80	TiAl, Ti_3Al
88TiAl–12SiC	40–63	TiAl, Ti_3Al, SiC, TiC, Ti_5Si_3, Ti_3AlC, amorphous phase
83TiAl–17Si_3N_4	40–63	TiAl, Ti_3Al, Si_3N_4, Ti_5Si_3, AlN, TiN, amorphous phase

When conducting metallographic examinations, an optical Neophot-32 microscope with a digital photography device was used; the measurements of microhardness were carried out in the PMT-3 device. X-ray structural analysis (XRD) of the coatings was performed in the installation DRON-UM-1 in a monochromatized CuK_α-radiation.

The studies of the coatings to erosion wear resistance were performed in a centrifugal accelerator of solid particles of the TsUK-3M model at a rotation frequency of the installation rotor of 3000 ± 50 rpm/min. As an abrasive material, quartz sand with 0.2–0.4 mm particles was used, which corresponds to the real size of particles in the pumped gas flow and the size of particles, coming into the air and wearing blades of aircraft gas turbine engines [11, 12]. The studies were performed at fixed angles of the abrasive attack: 30° (tangent flow) and 60° (frontal collision). As an index of wear resistance, the intensity of wear in milligrams per kilogram (average weight loss of specimens per 1 kg of abrasive got into the specimen) was taken. The total amount of abrasive spent for each series of specimens was 2 kg, a number of specimens with a coating of one type (thickness of coating is approximately 500 μm) is 3 pcs. For comparison, the tests of specimens of titanium VT6 alloy and aluminium AMg3 alloy were conducted.

As a method of corrosion resistance of coatings, a potentiostatic method was selected. The coatings with 500 μm thickness were deposited on the specimens of St3. The tests were performed in the P-5827M potentiostate at a scanning rate of 20 mV/s, and a temperature of 18–20 °C. As an electrolyte, 3 % NaCl solution was used. Stationary potentials were measured relative to the chlorine-silver electrode. The rate and potential of corrosion of the coatings were found by the graphic method from polarization curves. Using the values of corrosion currents that were determined from the polarization curves, a deep corrosion index (K_c) was calculated [13]. For comparison, under the same conditions the corrosion resistance of St3 steel, VT6 and AMg3 alloys was conducted.

RESULTS OF STUDIES AND THEIR DISCUSSION

STRUCTURE AND PHASE COMPOSITION OF COATINGS

Metallographic analysis (Figure 1) found that as a result of spraying of composite powders TiAl–SiC and TiAl–Si_3N_4 by SAGPS method as in the case of

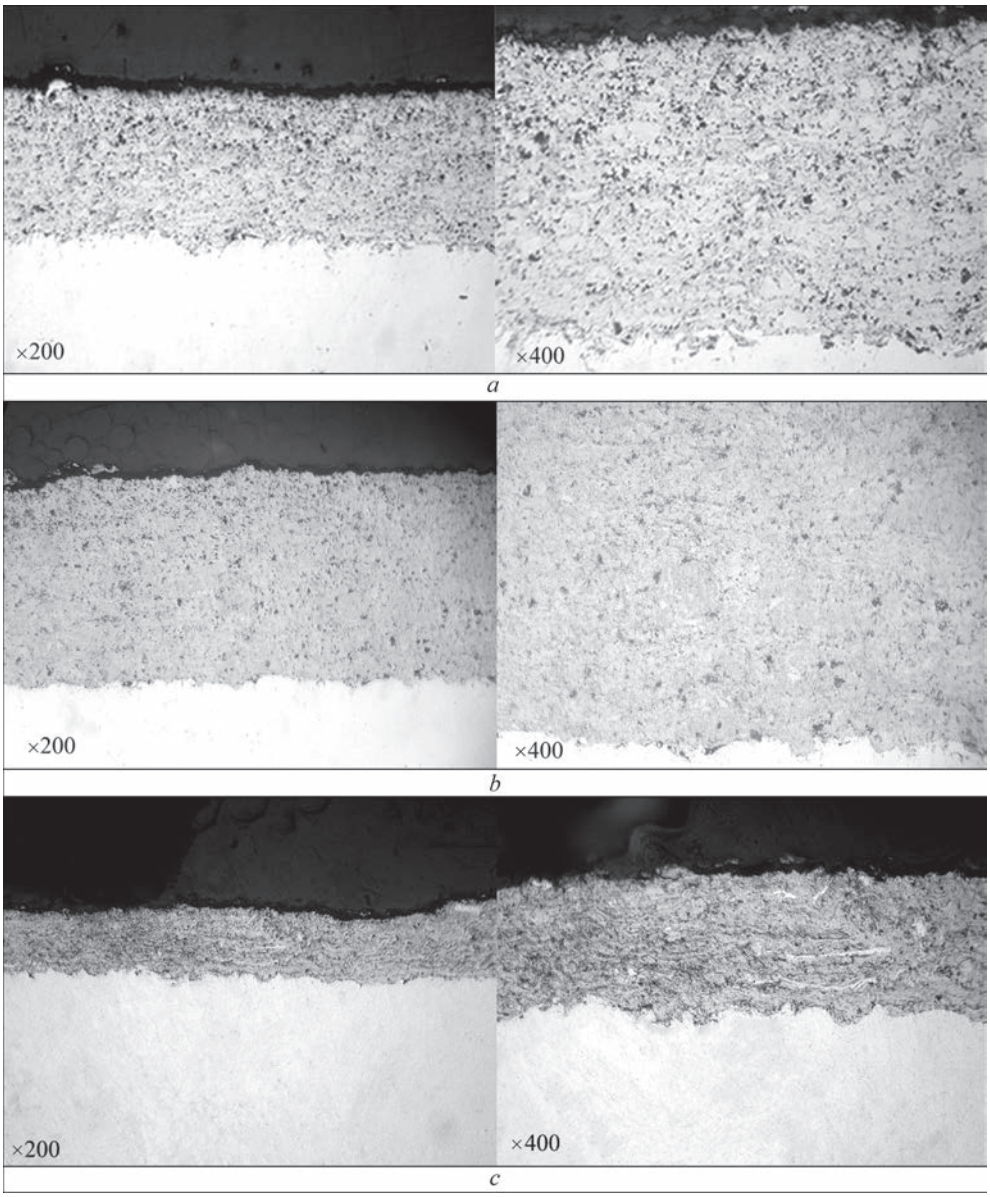

Figure 1. Microstructure of SAGPS-coatings: *a* — TiAl; *b* — TiAl–SiC; *c* — TiAl–Si_3N_4

spraying of initial TiAl powder, the coatings with a homogeneous dense structure are formed, consisting of lamellas, formed from particles completely molten and deformed during particle layer formation. The structural elements in the coatings are indistinguishable. The porosity of TiAl–SiC and TiAl–Si_3N_4 coatings amounts to 3–4 %, and in TiAl coating it is 8 %.

The data obtained from XRD (Figure 2) show, that as a result of physicochemical processes during spraying of coatings from composite powders, some changes in the phase composition are observed. In the process of spraying coatings of TiAl–SiC and TiAl–Si_3N_4 systems, the interaction of the components of TiAl composite powders with non-metallic refractory compounds and, unlike the powders after MChS, in the coatings there are no initial phases of SiC and Si_3N_4. This indicates the proceeding of exothermal reaction (according to thermodynamic calculations) in the spraying process that makes an additional heat input to the heating of powder particles. As a result of that, the end of the process of interaction of TiAl with the components of SiC and Si_3N_4 in spraying occurs, which did not proceed to the end in the process of MChS of powders. Due to proceeding of exothermic reaction and an increase in thermal energy of TiAl–SiC and TiAl–Si_3N_4 particles, in spraying the fraction of particles being in a completely molten state increases, and thus, a dense structure of coatings with lower porosity is formed than in spraying of the initial TiAl powder.

In the coatings of both systems, an amorphous phase disappeared as a result of passing the composite particles in the plasma jet of the heating zone to the transition into the melting stage with a subsequent cooling of the melt with the formation of crystalline phases. In the coatings during spraying, the oxides of

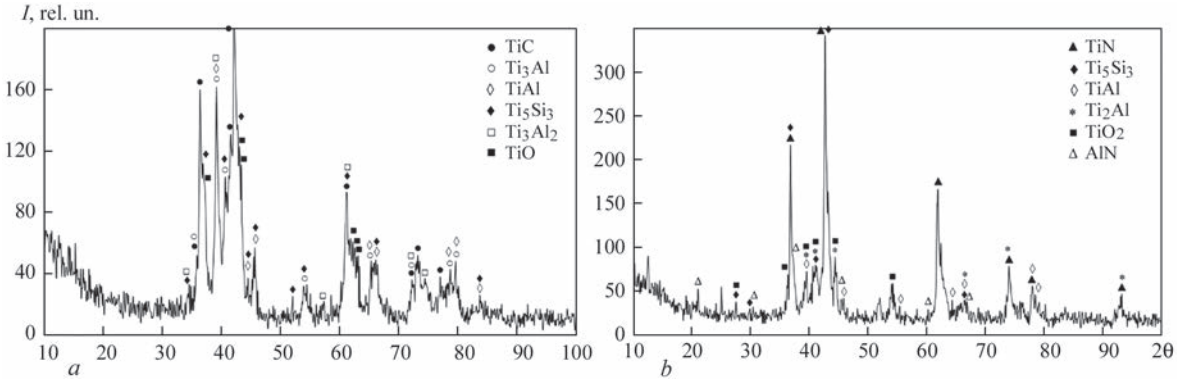

Figure 2. X-ray patterns of SAGPS-coatings: *a* — TiAl–SiC; *b* — TiAl–Si_3N_4

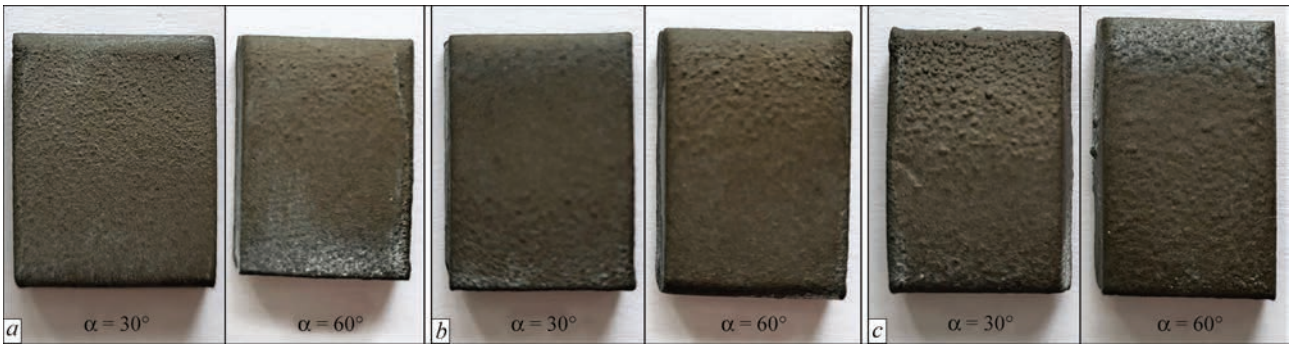

Figure 3. Appearance of the surface of specimens with SAGPS-coatings after tests for erosion resistance: *a* — TiAl–SiC; *b* — TiAl–Si_3N_4; *c* — TiAl

TiO and TiO_2 are formed, which is predetermined by interaction of the material that is sprayed with oxygen of the environment. In spraying TiAl–SiC coating as a result of phase transformations, instead of the triple phase of Ti_3AlC carbide, which was present in the powder, MACh-phase of Ti_3AlC_2 is formed.

Other changes in the phase composition of the coatings as compared to the composition of the initial composite TiAl-NRC powders, produced by MChS (Table 1) were not detected. In the coatings, the phase of initial TiAl powder maintains, as well as the phases foreseen by thermodynamic calculations (Ti_5Si_3, TiC, AlN, TiN).

The microhardness of TiAl—SiC and TiAl—Si_3N_4 coatings, which is 6610 ± 1070 and 6280 ± 950 MPa, respectively, due to the presence of solid phases of carbides, silicides, and nitrides in them, exceeds the microhardness of the TiAl coating by an average of 1300 MPa, the hardness of which is 5150 ± 670 MPa.

Table 2. Summarized results of tests on erosion resistance of SAGPS-coatings TiAl–SiC, TiAl–Si_3N_4, TiAl and VT6 and AMg3 alloys

Coating/alloy material	Average coating wear (mg/kg) at different angles of abrasive attack	
	30°	60°
TiAl–SiC	7.1 ± 1.1	10.8 ± 0.9
TiAl–Si_3N_4	8.0 ± 0.8	12.2 ± 1.2
TiAl	10.3 ± 1.2	15.3 ± 0.9
VT6 alloy	6.2 ± 0.6	5.2 ± 0.7
AMg3 alloy	7.7 ± 1.1	5.4 ± 0.4

EROSION RESISTANCE

As a result of studies of the resistance of the coatings under the conditions of erosive wear, it was found that the wear resistance of the developed TiAl–SiC and TiAl–Si_3N_4 coatings exceeds the wear resistance of the TiAl intermetallic powder coating by 1.3–1.5 times (Table 2), which is explained by the presence of strengthening phases in these coatings, that increase their strength and hardness.

The appearance of the specimens with the coatings after the tests (Figure 3) shows that the mechanisms of fracture of coatings of TiAl–NRC systems and TiAl coatings under the same influence of gas abrasive flow are slightly different. This is explained by the inner structure of the deposited coatings, in particular, by the presence of pores in the coatings. The effect of porosity on the nature of material wear can be considered from two positions. Firstly, pores and discontinuities, reducing the live cross-section of the deposited layer and being concentrators of local stresses, can significantly reduce strength properties of the coatings. Secondly, due to the peculiarities of the microrelief, which are associated with the presence of surface defects, the wear conditions of the specimens vary.

Table 3. Results of electrochemical studies of SAGPS-coatings in a 3 % NaCl solution

Coatings	Electrochemical characteristics			
	E_{st}, V	E_c, V	i_c, A/cm^2	K_c, mm/year
TiAl–SiC	–0.44	–0.40	$4.2\cdot10^{-7}$	0.019
TiAl–Si_3N_4	–0.42	–0.38	$4.8\cdot10^{-7}$	0.023
TiAl	–0.48	–0.42	$6.4\cdot10^{-6}$	0.045

Note. i_c (A/cm^2) for St3 steel — $6.5\cdot10^{-5}$; AMg3 alloy — $2.6\cdot10^{-5}$; VT6 alloy — $2.4\cdot10^{-6}$.

At each point, the angle of attack of the abrasive is determined by the size and shape of pores and cavities. As a rule, the conditions of wear of the specimens in the area of surface defects are more tough than in defect-free plane areas. As a result of the effect of the mentioned factors, a more intense chipping of larger TiAl coating blocks is possible under the action of the gas abrasive flow, which are observed on the surface of the specimens after the tests.

The intensity of wear of the investigated coatings is 1.5 times higher when examining the specimens at an angle of attack of the abrasive of 60°. It is known that according to the degree of resistance to gas-abrasive effect (depending on the angle of attack of abrasive particles), the powder materials and coatings are conditionally divided into two groups [14]: $\alpha < 35°$ — maximum wear for plastic and $\alpha > 45°$ — for brittle materials. Thus, TiAl–SiC and TiAl–Si_3N_4 coatings wear as brittle materials. Therefore, it will be rational to use the developed coatings at angles of attack of the abrasive that do not exceed 30°, which corresponds to the actual attack angles of the particles on the blades surface of centrifugal wheels in the compressors of oil and gas equipment [11].

It was also found that at an angle of abrasive attack of 60°, the wear resistance of TiAl–SiC and TiAl–Si_3N_4 SAGPS-coatings is 2.0–2.4 times lower than the wear resistance of the specimens made of VT6 and AMg3 alloys. In turn, at an angle of abrasive attack of 30°, the wear resistance of composite coatings is lower than the wear resistance of VT6 and AMg3 alloys by only 1.1–1.3 times, and in TiAl–SiC coating it slightly exceeds the wear resistance of AMg3 alloy (by 1.1 times).

CORROSION RESISTANCE

Electrochemical studies showed that the corrosion of SAGPS-coatings occurs with hydrogen depolarization with inhibition of anodic dissolution. The absence of passivation of the coatings is predetermined by the fact that a 3 % NaCl solution refers to an aggressive environment with a high content of Cl-, in the presence of which oxygen is removed from the surface of the electrode and the formation of a passive film on the surface of the coatings is prevented.

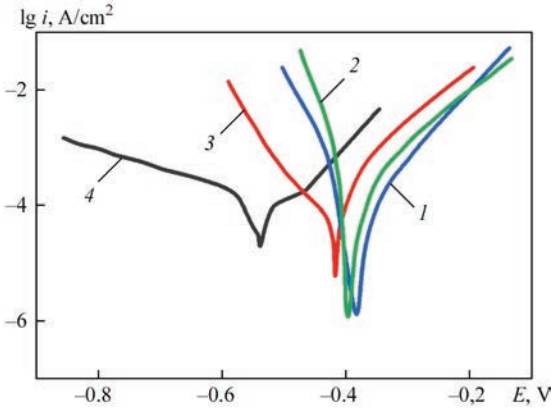

Figure 4. Polarization curves of SAGPS-coatings TiAl–SiC (curve *1*), TiAl–Si_3N_4 (curve *2*), TiAl (curve *3*) and St3 steel (curve *4*) in a 3 % NaCl solution

The kinetics of the corrosion process of the coatings of TiAl–NRC systems, unlike the coating of TiAl intermetallic, takes place with a shift of corrosion potentials in the positive direction and a decrease in corrosion currents (Figure 4).

The analysis of the results of corrosion studies showed that the corrosion resistance of TiAl–SiC and TiAl–Si_3N_4 SAGPS-coatings is superior to TiAl intermetallic coating by approximately one order of magnitude with the indices of corrosion current of $4.2\cdot10^{-7}$ A/cm^2, $4.8\cdot10^{-7}$ and $6.4\cdot10^{-6}$, respectively (Table 3).

An increase in corrosion resistance can be explained by the presence of titanium silicide Ti_5Si_3 in the coatings of TiAl–NRC systems, which, as is known [15], significantly increases the corrosion resistance of coatings and alloys in different aggressive environments, which is predetermined by the presence of strong covalent bonds metal–non-metal, as well as Si-Si bonds.

In addition, the corrosion resistance of the produced TiAl–SiC and TiAl–Si_3N_4 coatings exceeds the corrosion resistance of St3 by 135–155 times, AMg3 alloy by 24–62 times, and VT6 alloy by 5–6 times.

CONCLUSIONS

1. Applying the method of supersonic air-gas plasma spraying using composite powders produced by the method of mechanochemical synthesis, the coatings based on TiAl intermetallic with the additives of non-metallic refractory compounds SiC and Si_3N_4 were formed. As a result of spraying, heterophase coatings with a dense structure with a hardness of 6.3–6.6 GPa and a porosity of 3–4 % are formed.

2. It was found that in the process of spraying coatings of TiAl–SiC and TiAl–Si_3N_4 systems, the

components of TiAl composite powders interact with non-metallic refractory compounds and, unlike powders after mechanochemical synthesis, initial phases SiC and Si_3N_4 are absent in the coatings.

3. Conducted studies of erosion resistance of the coatings showed that due to the presence of solid phases in the developed coatings, the resistance under the conditions of erosive wear is 1.3–1.5 times higher than the resistance of the coatings made of TiAl intermetallic powder. According to the wear nature, the coatings TiAl–SiC and TiAl–Si_3N_4 belong to the brittle class and are recommended for using in the conditions of abrasive wear at angles of abrasive attack that do not exceed 30°.

4. Electrochemical studies showed that TiAl–SiC and TiAl–Si_3N_4 coatings, due to the presence of the titanium silicide phase in them, are superior in corrosion resistance to TiAl intermetallic coatings by approximately one order of magnitude in terms of corrosion resistance in a 3 % NaCl solution, and also exceed the corrosion resistance of St3 by 135–155 times, AMg3 alloy by 24–62 times and VT6 alloy by 5–6 times.

References

1. Noda, T. (1998) Application of cast gamma TiAl for automobiles. *Intermetallics,* **6**(7–8), 709–713. DOI: https://doi:10.1016/s0966-9795(98)00060-0
2. Lobanov, L.M., Asnis, Yu.A., Piskun, N.V., Statkevych, I.I. (2020) Improvement of mechanical properties of β-stable intermetallics of TiAl system by floating-zone refining. *Dopov. NANU,* **8**, 51–56. DOI: https://doi.org/10.15407/dopovidi2020.08.051
3. Zhang, W., Yang, Y.Q., Zhao, G.M. et al. (2014) Interfacial reaction studies of B_4C-coated and C-coated SiC fiber reinforced Ti–43Al–9V composites. *Intermetallics,* **50**, 14–19. DOI: https://doi:10.1016/j.intermet.2014.02.003
4. Liu, C., Huang, L.J., Geng, L. et al. (2015) In situ synthesis of (TiC + Ti_3SiC_2 + Ti_5Si_3)/Ti6Al4V composites with tailored two-scale architecture. *Advanced Engineering Materials,* 17(**7**), 933–941. DOI: https://doi:10.1002/adem.201400585
5. Jong-Keuk, P., Jong-Young, C., Hyeong-Tag, J., Young-Joon, B. (2009) Structure, hardness and thermal stability of TiAlBN coatings grown by alternating deposition of TiAlN and BN. *Vacuum,* 84(**4**), 483–487. DOI: https://doi:10.1016/j.vacuum.2009.10.013
6. (2003) *Study of cyclic oxidation behavior of anti-oxidation coatings on a super alloy.* Eds by Shahid M.R., Subhani T., Shengkai G., Mirza J.A. Dr AQ Khan Research Labs, Islamabad, Pakistan.
7. Li, G., Li, L., Han, M. et al. (2019) The performance of TiAlSiN coated cemented carbide tools enhanced by inserting Ti interlayers. *Metals*, 9(**9**), 918. DOI: https://doi:10.3390/met9090918
8. Fager, H., Andersson, J.M., Lu, J. et al. (2013) Growth of hard amorphous TiAlSiN thin films by cathodic arc evaporation. *Surface and Coatings Technology*, **235**, 376–382. DOI: https://doi:10.1016/j.surfcoat.2013.07.014
9. Gizynski, M., Miyazaki, S., Sienkiewicz, J. et al. (2017) Formation and subsequent phase evolution of metastable Ti–Al alloy coatings by kinetic spraying of gas atomized powders. *Surface and Coatings Technology*, **315**, 240–249. DOI: https://doi:10.1016/j.surfcoat.2017.02.053
10. Machethe, K.E., Popoola, A.P.I., Adebiyi, D.I., Fayomi, O.S.I. (2017) Influence of SiC–Ti/Al on the microstructural and mechanical properties of deposited Ti–6V–4Al alloy with cold spray technique. *Procedia Manufacturing,* **7**, 549–555. DOI: https://doi:10.1016/j.promfg.2016.12.069
11. Parajko, Yu.I. (2011) Regulations of wear of operating surfaces of gas-compressor unit and development of technologies of their service life increase. *Problemy Tertya ta Znoshuvannya*, **56**, 71–83 [in Ukrainian].
12. Mikhailov, D.A. (2014) Main features of operation of GTE compressor blades and classification of their service functions. *Progresyvni Tekhnologii i Systemy Mashynobuduvannya,* 50(**4**), 126–131 [in Russian].
13. Zhuk, N.P. (2006) *Course of theory of corrosion and protection of metals*. Moscow, LLC TID Alliance [in Russian].
14. Kulu, P. (1988) *Wear resistance of powder materials and coatings.* Tallin, Valgus [in Ukrainian].
15. Liu, L. Xu, J., Li, Zh. (2013) Electrochemical characterization of Ti_5Si_3/TiC nanocomposite coating in HCl solution. *Inter. J. Electrochem. Sci.*, **8**, 5086–5101.

ORCID

Yu.S. Borysov: 0000-0002-6019-8464,
N.V. Vihilianska: 0000-0001-8576-2095,
M.V. Kolomytsev: 0000-0003-0602-5615,
K.V. Iantsevych: 0000-0002-3975-7727,
O.M. Burlachenko: 0000-0003-2277-4202,
T.V. Tsymbalista: 0000-0001-9569-7776

CONFLICT OF INTEREST

The Authors declare no conflict of interest

CORRESPONDING AUTHOR

N.V. Vihilianska
E.O. Paton Electric Welding Institute of the NASU
11 Kazymyr Malevych Str., 03150, Kyiv, Ukraine.
E-mail: pewinatalsa@gmail.com

SUGGESTED CITATION

Yu.S. Borysov, N.V. Vihilianska, M.V. Kolomytsev, K.V. Iantsevych, O.M. Burlachenko, T.V. Tsymbalista (2022) Formation of composite coatings by the method of supersonic plasma spraying of powders based on TiAl intermetallic with non-metallic refractory compounds SiC and Si_3N_4. *The Paton Welding J.*, **6**, 11–16.

JOURNAL HOME PAGE

https://pwj.com.ua/en

Received: 30.05.2022
Accepted: 15.08.2022

https://doi.org/10.37434/tpwj2022.06.03

REPAIR OF THE BODY OF CONNECTING ROD OF MOBILE JAW CRUSHER METSO LOKOTRACK LT 120

V.D. Poznyakov, O.A. Gaivoronskyi, Yu.V. Demchenko, A.M. Denysenko, G.V. Zhuk

E.O. Paton Electric Welding Institute of the NASU
11 Kazymyr Malevych Str., 03150, Kyiv, Ukraine

ABSTRACT

The paper describes the experience of repair welding of service defects in the body of the connecting rod of mobile jaw crusher Metso lokotrack LT 120, which is a rather rigid honeycomb structure from cast low-alloyed steel of 20GL type with thickness of external walls of 60 mm and of partitions of not less than 45 mm and more than 5 t weight. It was found that the most significant defects — fatigue cracks and cleavage which are incompatible with performance, naturally formed near the structural stress raisers, service damage, caused by contact impact of armour protection, casting defects, as well as in the sites of unsmooth connection of elements, etc. Crack opening displacement is equal to 2–3 mm that is indicative of the start of shape change of the body and need for prevention of further operation in such a state. Rigid structure of the connecting rod body and general state of destruction required special technology of repair welding, which was created and realized by the authors. It included new welding consumables, technological measures and engineering solutions and those verified by our own practical experience of repair of cast structures, as well as high skill and competence of the welders. Practical importance and effectiveness of the performed work on connecting rod repair was confirmed by safe operation of the crusher in the design mode for two years.

KEYWORDS: connecting rod, service defects, design stress raisers, through-thickness cracks, repair-welding technology, rigid framework, weldability, mechanical peening of welds

INTRODUCTION

A large number of foreign highly productive technological equipment, in particular jaw crushers, has been imported into mining, cement and construction industry of Ukraine over the recent decade. The most widely spread are mobile jaw crushers, namely Metso lokotrack LT 120 (Finland). It is designed for primary rock crushing by their compression between flat surfaces called jaws, which are located at a small angle to each other. The operating principle consists in that one of the crushing surfaces is stationary, while crushing is performed due to the mobile jaw moving closer to the stationary one. The mobile surface, which is called the connecting rod, performs reciprocal movements, thus alternatively reducing or increasing the gap between the jaws that leads to high compressive and shear stresses, and, as a result, to the rock breaking up [1]. As the connecting rod operates under variable static loading, its body is made from cast low-alloyed steel with a rather rigid honeycomb structure with 60 mm thickness of the outer walls, not less than 45 mm thickness of the partitions, and more than 5 t weight (Figure 1).

Intensive operation of Metso lokotrack LT 20 jaw crusher at PJSC “Kryvyi Rih Cement” Company for five years resulted in formation of a number of defects on the connecting rod body. Location of the most significant of them, detected by the methods of visual-optical control, is given in Figure 2 and Table 1. Photofixation of cracks Nos 1–4, incompatible with further performance of the rod, is given in Table 2.

As one can see from Figure 2, through-thickness fatigue cracks Nos 1–4 naturally developed from structural stress raisers, service damage, contact impact of armour protection, casting defects, as well as in areas of unsmooth connection of elements, etc. Crack opening is equal to 2–3 mm that is indicative of the start of distortion of the body shape and inadmissibility of its further operation in such a state. Therefore, at the peak of 2002 season crusher operation was interrupted, as there was no spare connecting rod on stock. At mining enterprises repair of such parts by welding is considered to be the main measure for restoring their integrity, and extension of their operation term [2]. The complex nature of destruction and absence of qualified specialists, needed to restore parts by welding, initiated the appropriate plant

Figure 1. Design features of the connecting rod body

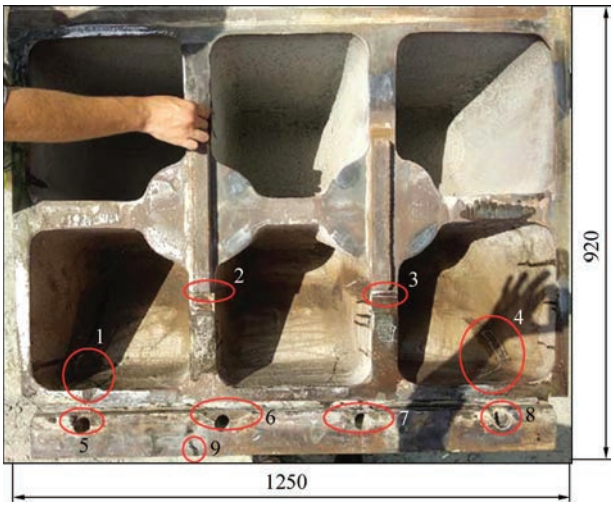

Figure 2. Location of defects Nos 1–9 on the walls and partitions of the rod body

services turning to PWI for technical assistance. In view of the design features, general state, destruction parameters, and operating conditions, PWI specialists came to the conclusion that the connecting rod is repairable in case of application of special repair-welding technology.

The objective of this work consists in development of a repair technology that allows reducing the level of residual stresses in joints, where welding is performed under the conditions of limited deformation, and ensuring their high technological strength and operability under variable static loading.

MATERIALS AND PROCEDURES

In order to develop the respective repair-welding technology, it is necessary to study the chemical composition of foreign cast steel, assess its weldability and technological strength, select a welding process and welding consumables, and to develop new engineering solutions for restoration of the integrity and load-carrying capacity of the body, as well as technological methods to adjust the welding stresses.

For performance of welding operations, it was considered rational to apply coated-electrode manual arc welding (111) and gas-shielded mechanized welding (135), as well as their combination. Taking into account the chemical composition and potential mechanical properties of the cast steel, and requirements of ensuring high technological strength, low-hydrogen welding electrodes of BOHLER FOX EV 50 grade of 3.2 and 4.0 mm diameter (AWS A5.1 E7018) and welding wire of Bohler DMO-IG grade of 1.2 mm diameter (AWS A5.28M-05) were selected. Proceeding from our own experience at performance of such repairs, it was decided to conduct welding in the modes with lower heat input [3, 4], given in Table 3, which were corrected during work performance, in order to improve the stress-strain state of repair joints of the connecting rod under the conditions of their rigid fastening. Positive results, obtained earlier at combined application of both the methods were also taken into account, for instance, when manual welding was used for facing of the groove, and mechanized process — for performance of the filling layers. Previous practice has shown that welding with facing of the edges of not less than 3 mm thickness promotes formation of a more favourable structure in the metal of welded joint HAZ and prevents appearance of cold

Table 1. Characteristic inadmissible service defects on the rod body surface

Defect number	Defect type	Length, mm
1	Through-thickness crack	370
2		320
3		330
4		270
5	Spallation	50
6		100
7		70
8		75
9	Blowhole	30
10	Surface wear	100 %, depth > 4 mm

Table 2. Location and parameters of defects (through-thickness cracks) Nos 1–4

Table 3. Technological characteristics of welding modes

Welding process	Electrode diameter. mm	Kind of current, polarity	Welding current, A	Arc voltage V
111	3.2 4.0	Direct, reverse	120–140 140–160	24–26
135	1.2		160–200	26–28

cracks and spallation in it, even in welding alloyed steels [5, 6]. Considering the great thickness of the rod body walls and in order to increase the cold cracking resistance, it was also believed rational to apply preheating up to 80–100 °C in welding [6, 7]. In welding under the rigid restraint conditions, for this repair case it was recommended to apply mechanical peening of weld metal layers, using a special impact tool [8]. Before the start of welding operations, baking of electrodes in electric furnaces at the temperature of 300–350 °C for 1.5 h should be usually performed. To eliminate their moistening, during operation they must be kept in thermal cases at the temperature of 70–80 °C. For manual welding it is necessary to use, for instance, field-proven DC current source VD-306, and for mechanized gas-shielded welding (80 % Ar + 20 % CO_2) — the apparatus of ewm Phoenix Pulse 501 model with built-in semi-automatic machine. The methods of cutting out the damaged metal cracks and edge preparation for welding, used in the work, are well-established and have been applied in our practice for a long time [9]:

- mechanical cutting, plasma and electric-arc gauging by special electrodes of ANR-2 type;
- surface cleaning by an abrasive tool.

Connecting rod preparation for repair consisted in removal of contamination and lubricants from the surface in the welding zone, as well as mechanical cleaning of the surfaces from scale and thorough check for defects using penetrants.

The described experience and recommendations were included into the repair technology of restoration of the connecting rod integrity.

INVESTIGATION RESULTS

As a result of studying the chemical composition, it was found that the content of elements in the metal sample taken from the rod body, is as follows, wt.%:

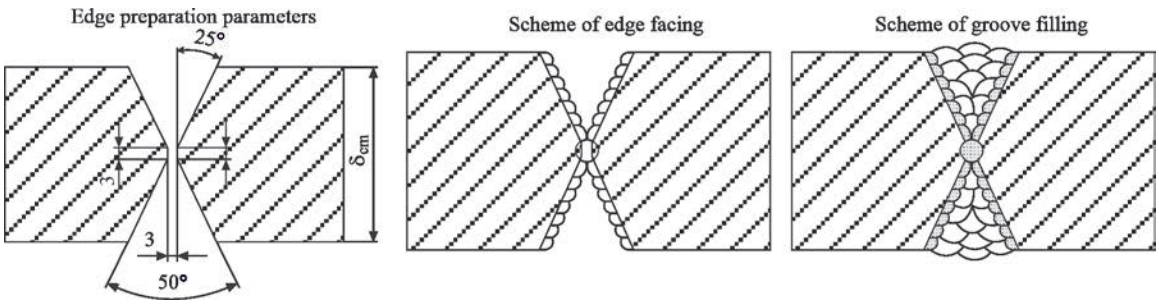

Figure 3. Scheme of repair of defects Nos 1–4

Figure 4. General view of the region of repair of crack No. 1 on the front wall (*a*), after thermal removal of a wall fragment (*b*), after welding (*c*) from the inside and outside, respectively

Figure 5. General view of repair of crack No. 2 on the front wall after mechanical edge preparation (*a*) and after welding (*b*)

C — 0.20, Si — 0.43, Mn — 1.52, S — 0.007, P — 0.023. Such metal is identified as low-alloyed steel, analog of local steel of 20GL grade to GOST 977–88. Its weldability at carbon equivalent C_{eq} = 0.45 is assessed as satisfactory.

Welding technique was as follows: block method, up to 100 mm block size, not more than 10 mm width of individual weld beads.

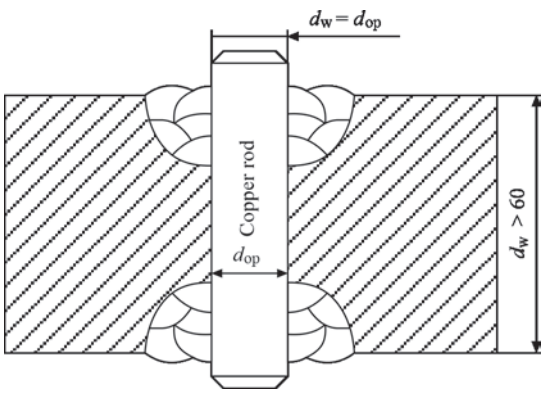

Figure 6. Scheme of repair of defects Nos 5–8

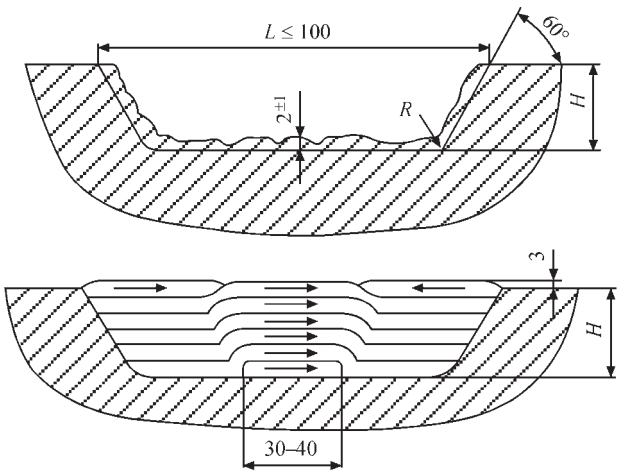

Figure 7. Scheme of repair of defect No. 9

Taking into account the size and diversity of the defects, their repair sequence was as follows: regions with cracks in the walls were cut out and welded first (defects Nos 1–4), openings were repaired in the second turn (defects Nos 5–8), and blowholes were the third to be repaired (defect No. 9). Repair was completed by restoration of the worn surfaces.

Repair of defects Nos 1–4 was performed after crack cutting out, edge facing with electrodes of Bohler FOX EV 50 grade with subsequent mechanized welding up of the groove, using Bohler DMO-IG wire according to the scheme, given in Figure 3. An example of the general view of the region of repair of crack No. 1 on the front wall is given in Figure 4, and that of the crack No. 2 — in Figure 5. When going over to welding of the weld outer side, the weld root cleaning must be performed. During welding mechanical peening of deposited metal layers by an impact tool was performed up to a change of the weld pattern, except for the first layer in the weld root and the facing layer. Weld interpass temperature was maintained in the range of 130–150 °C.

Repair of defects Nos 5–8 was performed after treatment of the inlet channel and installation of the copper rod into the opening. Welding was conduct-

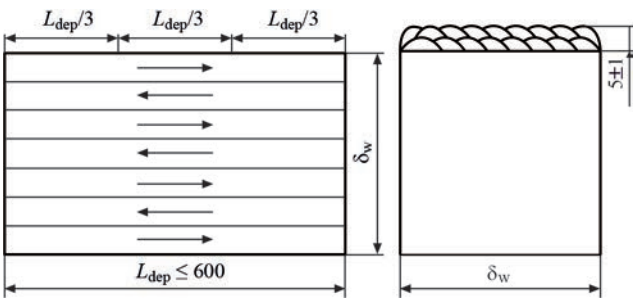

Figure 8. Scheme of restoration of worn surfaces

ed by FOX EV 50 electrodes, in keeping with the scheme, given in Figure 6.

Blowhole repair (defect No. 9) was carried out according to the scheme (Figure 7) with prior grinding to clean metal, using mechanized welding by Bohler DMO-IG wire.

Restoration of worn surfaces was performed with prior removal of the work-hardened layer to the depth of 0.8–1.0 mm and further deposition of longitudinal beads by Bohler DMO-IG wire with 1/3 overlapping in two layers, according to the scheme in Figure 8. Finish grinding was performed to metal level, no blackness was allowed.

At planned breaks or long-term interruptions of the work, as well as after completion of welding, repair joints must be subjected to slow cooling with periodical heating by gas-oxygen flame up to the temperature of 120–150 °C with covering by thermal insulation materials.

Welding operations support provided by our specialists during the entire period of their performance showed that the proposed technology ensures the high technological strength of the repair joints and is professionally realized by qualified welders without any problems. After performance of visual-optic control the restored connecting rod was transferred to the enterprise with guarantee period of 12 months. Two years have passed since putting it into operation up to now. During this time, the enterprise did not make any claims as to the quality of the provided service.

CONCLUSIONS

It was clarified that inadmissible service defects on the connecting rod body made its further operation impossible, and required repair by a special technology, which would take into account the design features of the repaired object, the state of its damage and need for welding under the conditions of limited deformation. Custom-designed technology includes new welding consumables, technological measures and engineering solutions and those tried out by our practical experience of repair of similar cast structures, as well as high skill and competence of welders. Practical importance and effectiveness of its application has been confirmed by the rod operation in the design working mode of the mobile jaw crusher Metso lokotrack LT 120 for two years.

REFERENCES

1. Kravets, V.G., Terentiev, O.M., Chala, O.M. (2019) *Technique and technology of rock processing:* Manual. Kyiv, NTUU KPI [in Ukrainian] Electron data.
2. Lashchenko, G.I. (2019) Welding production in the economy of Ukraine. *The Paton Welding J.*, **11**, 2–7. DOI: https://doi.org/10.15407/tpwj2019.11.01
3. Poznyakov, V.D. (2017) Technologies of welding for production and repair of metal structures from high-strength steels. *Visnyk NANU*, **1**, 64–72 [in Ukrainian].
4. Poznyakov, V.D., Gajvoronsky, A.A., Zhdanov, S.L., Demchenko, Yu.V. et al. (2004) Restoration of one-piece-cast bases of cone crushers by welding. *Svarshchik*, **5**, 6–9 [in Russian].
5. Volchenok, V.N., Makarov, E.L. (1991) *Welding and welded materials:* Handbook in 3 Vol. Moscow, Metallurgiya [in Russian].
6. Gajvoronsky, A.A. (2014) Resistance to cold crack formation of HAZ metal of welded joint on high-strength carbon steels. *The Paton Welding J.*, **2**, 2–11.
7. Poznyakov, V.D., Gajvoronsky, A.A. (2006) Resistance to delayed fracture of welded joints in repair welding of cast structures from high-strength carbon steels. In: *Problems of life and service safety of structures, constructions and machines.* Kyiv, PWI, 411–414 [in Ukrainian].
8. Lashchenko, G.I., Demchenko, Yu.V. (2008) *Energy saving technologies of postweld treatment of metal structures*. Kyiv, Ekotekhnologiya [in Russian].
9. (2013) *Renovation technologies of welding and related processes:* Lecture notes for students. Comp. by S.M. Getmanets, D.V. Stepanov. Kyiv, NTUU KPI [in Ukrainian].

ORCID

V.D. Poznyakov: 0000-0001-8581-3526
O.A. Gaivoronskyi: 0000-0002-8146-7790,
Yu.V. Demchenko: 0000-0002-7899-6608

CONFLICT OF INTEREST

The Authors declare no conflict of interest

CORRESPONDING AUTHOR

V.D. Poznyakov
E.O. Paton Electric Welding Institute of the NASU
11 Kazymyr Malevych Str., 03150, Kyiv, Ukraine.
E-mail: paton39@ukr.net

SUGGESTED CITATION

V.D. Poznyakov, O.A. Gaivoronskyi, Yu.V. Demchenko, A.M. Denysenko, G.V. Zhuk (2022) Repair of the body of connecting rod of mobile jaw crusher METSO LOKOTRACK LT 120. *The Paton Welding J.*, **6**, 17–21.

JOURNAL HOME PAGE

https://pwj.com.ua/en

Received: 18.05.2022
Accepted: 15.08.2022

https://doi.org/10.37434/tpwj2022.06.04

EVALUATION OF LOAD BEARING CAPACITY OF CYLINDRICAL SHELL OF ABOVE-GROUND VERTICAL STEEL WELDED TANK FOR OIL STORAGE AFTER REPAIR

A. Barvinko, Y. Barvinko, A. Yashnik, O. Kostenevich

E.O. Paton Electric Welding Institute of the NASU
11 Kazymyr Malevych Str., 03150, Kyiv, Ukraine

ABSTRACT

When above-ground steel tanks are repaired, certain improper techniques used during welding of individual sheets into the tank shell may cause depressions to form in the shell surface. Such deviations in the shell shape from the design geometry create additional stresses. In this study basing on result of computer calculation of tank with D = 22.8 m and H = 12.0 m it is proposed that if the shell imperfection is a rectangular depression of a near-cylindrical design geometry, it is possible to increase the allowable stresses by 10 % by introducing a specific coefficient taking into consideration the effect of additional stresses.

KEYWORDS: vertical cylindrical above-ground tank, stressed state, rectangular depression, local shell deformation, welding, repair

INTRODUCTION

When repairing cylindrical steel oil storage tanks by closed-contour welding of individual sheets into the tank shell, buckling or deformation under extended residual weld stresses may be observed [1]. Depressions may form in the thin-walled cylindrical shell creating under the hydrostatic pressure load additional bending stresses exceeding the yield strength of the material [2, 3] in the areas deviating from the design geometry. This requires reducing the filling height of the tank, which may create technological restrictions at storage plants in situations when the volume needs to be clearly defined, e.g., when the reservoirs used are measuring tanks.

Oil storage tanks are high hazard objects classified as Consequences Class 3 (CC3) [4]. Thus, the problem of assessing strength and stiffness of such tanks is especially important. Particular attention should be paid to the development of a separate approach to assessing the impact of initial imperfections, such as depressions, on the bearing capacity of the cylindrical shell [5–7]. Most research on the bearing capacity of cylindrical steel tank shells that takes into consideration the initial geometric imperfections [8–10] is aimed at improving the calculation algorithms and assessing the conditions leading to the loss of overall stability. Some studies [11–13] used stress concentration factor to analyze the issue of local strength of a thin-walled cylindrical shell. This approach, however, does not allow estimating the total strength and residual life of the tank shell fully. Another study considered the possibility to reduce bending stress for an isolated depression by reinforcing the structure with vertical ribs and a horizontal stiffening ring [2].

Thus, estimating the load-bearing capacity of a deformed shell is an urgent problem requiring further research. In this study, we propose a refined strength criterion for estimating the influence of shape imperfections, i.e. rectangular depressions, on the general shell strength. The chosen object of study was an above-ground steel tank (diameter D = 22.79 m, H = 11.845 m) with a single rectangular depression formed in its shell during welding of repair sheets without changing the curvature sign of the shell. The depression was caused by insufficient transverse shrinkage compensation in vertical welded joints [14]. This required revising the oil filling height during further operation of the tank.

DESIGN SOLUTIONS FOR REPAIRING AND DEFECT TOLERANCE ASSESSMENT

The vertical steel tank (Figure 1) consisted of a cylindrical shell, a bottom, and a conical panel-frame roof with a central support column. By the time of the repair, the tank had been in operation for 58 years. According to the repair project, it was planned to replace the entire 1st course and the defective section from the 2nd course and to the full height of the shell (Figure 1). The lower part of the insert from the 2nd to the 5th course was ~ 4.5 m high and was welded to the shell with a vertical flat butt weld, while for the upper part, which was ~ 5.1 m wide and ~ 5.5 m high, the overlap weld was used.

The tank shell had 8th courses: the height of the first new course was 1.79 m, the height of the other courses was approximately 1.49 m. The total height of the shell was H = 11.759 m. The design thickness of the courses from bottom up was 9.2–7.3–7.5–5.7–4.8–4.8–4.9–4.8 mm. The first new course and repair insert were made of non-alloy structural steel St3sp5-

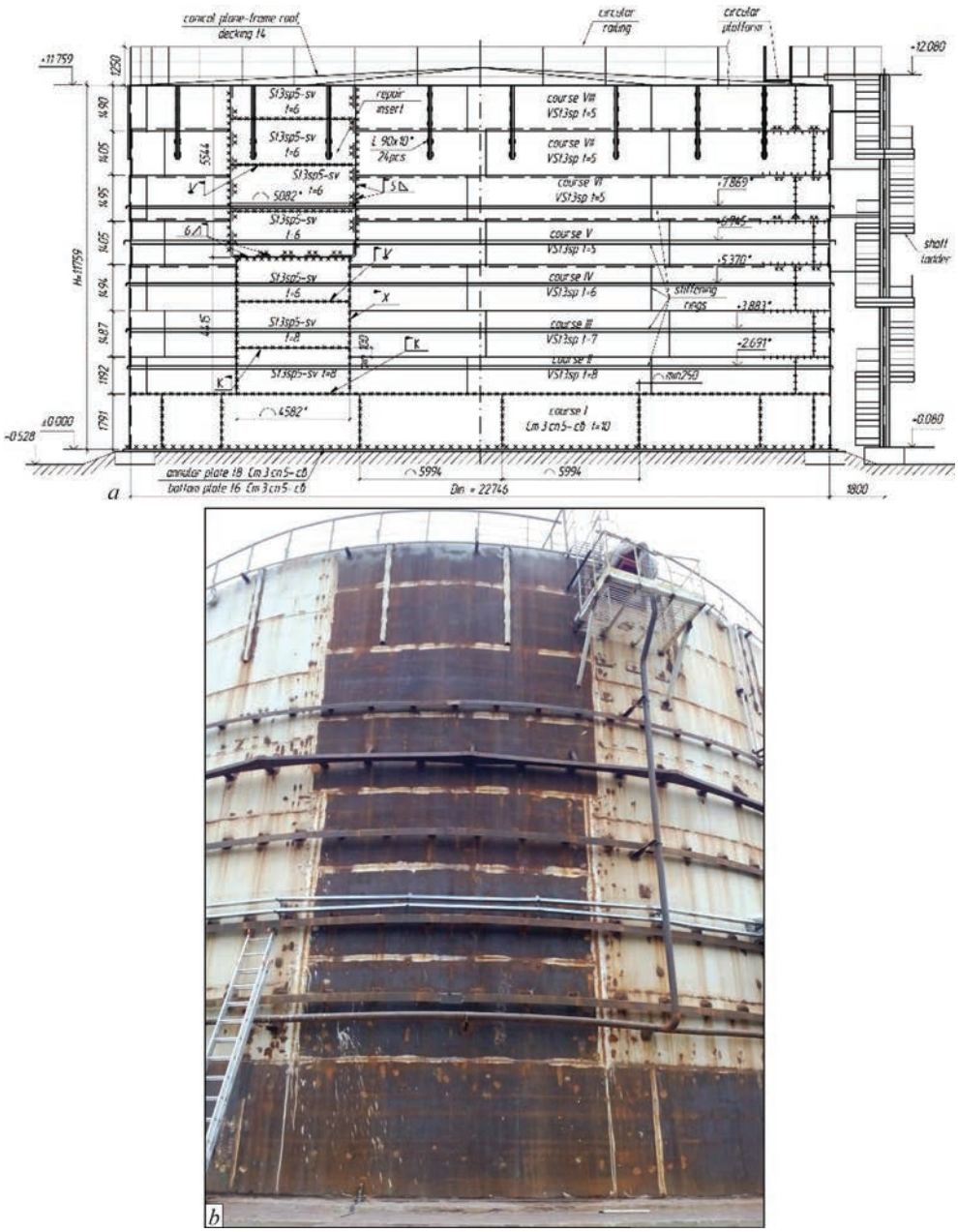

Figure 1. Process of tank repair: *a* — design schema; *b* — shell after installation stiffening rings, tank is empty

sv with min yield strength $R_{ey} \geq 255$ MPa (analog of S235 steel) steel, while the rest of the courses were made of non-alloy structural steel VSt3sp, with min yield strength $R_{ey} \geq 210$ MPa (analog of S235 steel). To ensure that the shell was generally stable, 24 L-shaped stringers (L90×10) were installed on its upper courses (VII-VIII), and a stiffening ring made of bent profile L6×90×200 was mounted at the mark +6.745 m.

For welding repair insert it was used the process 135 in the mix M21 with the solid electrode wire G3Si1. Vertical butt welds in insert had X-joint preparation, horizontal welds had X-joint preparation (see Figure 1). Existing shell welds were welded with using process 121.

A deviation from the vertical weld technology caused the repair insert to deform, which created a depression taking up the full height of the shell characterized by unacceptable [6] vertical deviations (Figure 2). Estimation of the geometric shape of the deformed shell (local deviations) using a template (straightedge) showed that it met the standard requirements [5, 6].

Eurocode 3 stipulates [15] that in the plastic limit state LS1 (yield strength), the strength analysis for tanks is performed using the circumferential stress:

$$\left[\gamma_F \rho g H_{\text{red}} + p_{\text{Ed}}\right]\left(\frac{r}{t}\right) \leq f_{yd}, \qquad (1)$$

where r is the radius of the tank ρ is the density of the stored liquid; g is the free fall acceleration; $H_{\text{red, j}} = H_j - 0.3$ m (H_j is the vertical distance from the bottom of the j^{th} course to the filling height level); p_{Ed} is the calculated value of internal pressure; γ_{M0} is the

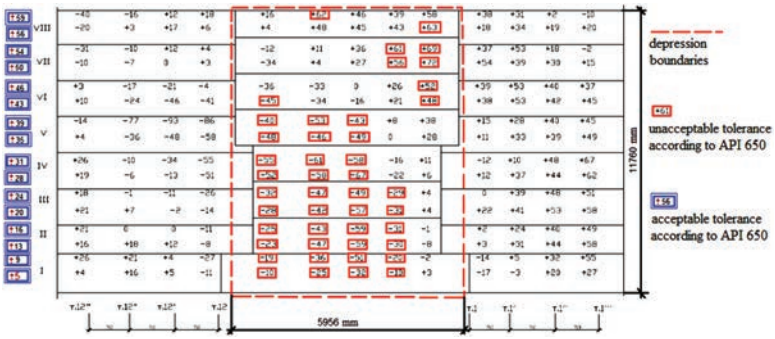

Figure 2. Size of depression and out-of-plumbness values for tank with installed stiffening rings, "+" outside of tank, "–" inside of tank

partial resistance factor; $f_{yd} = f_{yk}/\gamma_{M0}$; f_{yk} is the characteristic value of the yield strength.

According to EN14015 [5], when operating a tank, the maximum allowable design stress S of the tank's shell must be 2/3 of the yield strength, but must not exceed 260 MPa. The minimum required shell thickness e_c is determined based on the circumferential stress by the formula:

$$e_c = \frac{D}{20S}\left\{98W\left(H_c - 0.3\right) + p\right\} + c, \qquad (2)$$

where D is the tank diameter; W is the maximum design density of the product; p is the design internal pressure; c is the corrosion allowance; H_c is the distance from the bottom edge of the course to the filling height.

The API-650 standard describes a similar approach [6].

Thus, when performing strength analysis of the tank shell with imperfections, one needs to consider the action of circumferential and additional stresses.

Let us consider how the depressions formed in the tank shell during its repair affect its stress state. The analysis of these deformations shows that the actual geometric shape of the deformed area of the shell can be viewed as a smooth unfractured rectangular depression 5956 mm wide and 11760 mm high (Figure 2) with a smooth transition to the cylindrical shell. Since the depression is formed due to insufficient transverse shrinkage compensation in the repair vertical welds [14], it happens largely through the reduction of the insert arc length. This means that the shell in the depression area deforms in such a way that its radius increases. Thus, the change in the stress state of the cylindrical shell must be mainly contributed by additional bending stresses [16].

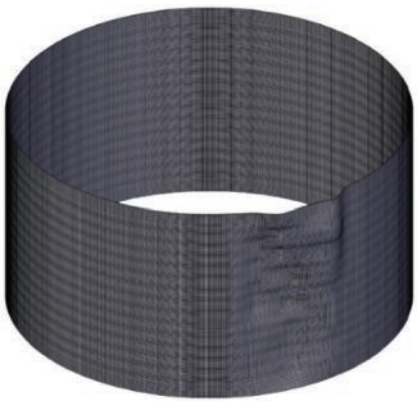

Figure 3. Tank shell geometry obtained using third order approximation curves [18]. Magnification ×10

In order to reduce the initial deviations from the design geometry, the tank shell was reinforced with four L-shaped stiffening rings (L100×8 mm, L125×8 mm) installed at the marks +2.691 m, +3.883 m, +5.370 m, and +7.869 mm during the filling of the tank. The stiffening rings strengthened the structure, allowing for the general stability of the tank shell. Figure 2 presents the out-of-plumbness values for the empty tank after the hydrostatic test has been completed and the stiffening rings fixed to the shell.

Computer simulation of the stress-strain state of the tank shell deviating from the design geometry (Figure 2) was performed by the finite element method (FEM) using the SCAD Office 21.1.9.9 software system. The finite element model of the tank shell consisted of rectangular shell elements taking into consideration geometric nonlinearity. The minimum size of the rectangular finite element was 114.5×122.5 mm. For the lower edge of the shell the fixed-end boundary condition was set, while the boundary condition of horizontal translational motion was set for the top edge of the shell. The fixed roof of the tank was represented by a load evenly distributed along the upper edge of the shell. Stiffening rings and stringers were modeled using end rod elements. The design specific weight of oil was taken as 0.87 t/m^3.

To analyze the flat stress state in the tank shell with initial deviations under hydrostatic pressure, we used the von Mises theory [17].

Analytical description of the imperfections in the shell geometry was performed using third order approximation curves according to the study by A.A. Krysko [18]. Figure 3 shows the results of computer simulation of the tank shell with the depression (the surface imperfections are 10 times magnified for illustrative purposes). The junction between the depression and the cylindrical shell was described by a sinusoidal curve.

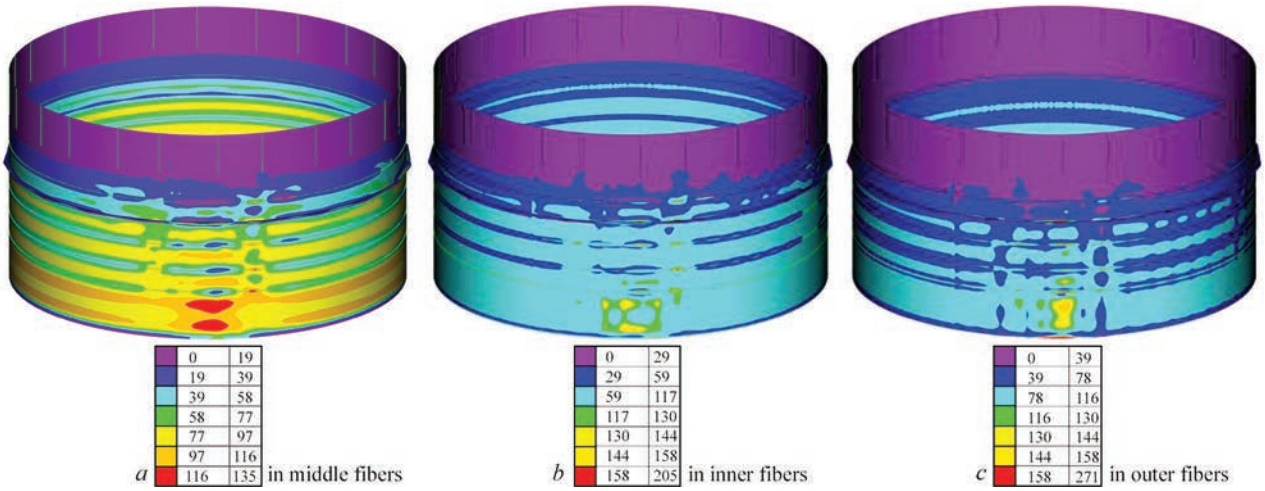

Figure 4. Equivalent (von Mises) stress σ_{eq}, MPa in shell with rectangular depression formed after repair welding

RESULT OF NUMERICAL RESEARCH & DISCUSSION

The results on FEM calculations of equivalent (von-Mises) stresses obtained in the middle, inner, and outer shell fibers under hydrostatic pressure load (product density 0.87 t/m^3) are presented in Table 1 for two filling heights, H_f = 9 m and H_f = 10 m, and in Figure 4, *a–c* for H_f = 10 m. The maximum local equivalent stresses acted at the junctions between the shell and the stiffening rings. To avoid the edge effect in the ring-to-shell junction areas, the stresses in the shell were determined at a distance greater than $0.6(rt)^{1/2}$ from those areas.

The maximum fraction of bending stresses was defined as the ratio of the equivalent stress in the outer ($\sigma_{eq\ out}$) or inner ($\sigma_{eq\ in}$) shell fibers (whichever the largest) to the equivalent membrane stress in the middle fibers ($\sigma_{eq\ m}$), Δ_{eq}, or to the allowable stress (σ_{all}), Δ_{all}. The latter was taken as per API 650 [6]:

$$\sigma_{all} = \min\begin{Bmatrix} 0.4\,f_u \\ 0.67\,f_y \end{Bmatrix} = 144 \text{ MPa}. \qquad (3)$$

The analysis of the nonlinear calculation results (Figure 4, *a–c*, Table 1) shows that deviations from the design geometry cause additional stresses in the outer/inner fibers of the deformed area of the shell.

The highest equivalent stresses in the middle fibers of the shell (equivalent membrane stresses) were observed for the 1st and 2nd courses: $\sigma_{eq,\ m}$ = 120 MPa (H_f = 9 m) and $\sigma_{eq,\ m}$ = 135 MPa (H_f = 10 m), the equivalent stresses in the outer fibers were σ_{eq} = 143 MPa (H_f = 9 m) and σ_{eq} = 158 MPa (H_f = 10 m).

The analysis of the data from Table 1 shows that when the filling height is increased to the design value H_f = 10 m, the strength condition [6] in the first and second courses is not met (Table 1). Additional bending stresses in the shell cause the design equivalent stresses σ_{eq} to increase by 10 % relative to the allowable values σ_{all}.

In order to substantiate the value of additional bending stresses, let us analyze the stress state of an isolated rectangular depression in the cylindrical tank shell considered allowable by the standards [5–7]. The API 650 [6] and EN14015 [5] standards require assessing the geometry tolerance in a deformed shell using a template or a vertical straightedge with a length of 0.9 and 1.0 m.

Table 1. Calculation results on stresses in repair insert courses of steel shell (St3sp-5, S255) of various thickness ***t*** for two filling heights H_f

No. course	*t*, mm	H_f = 9 m		H_f = 10 m	
		$\sigma_{eq\ mid}/\sigma_{eq\ in}/\sigma_{eq\ out}$, MPa	Δ_{eq}/Δ_{all}, %	$\sigma_{eq\ in}/\sigma_{eq\ out}$, MPa	Δ_{eq}/Δ_{all}, %
1	9.2	120/132/143	16/–	134/149/158	15/10
2	7.2	120/136/143	16/–	135/149/158	15/10
3	7.2	100/106/120	17/–	115/122/136	15/–
4	5.4	86/100/102	16/–	104/122/122	15/–
5	5.4	72/80/90	20/–	90/101/100	11/–
6	5.4	44/54/55	20/–	63/76/62	17/–
7	5.4	14/33/40	65/–	32/47/40	32/–
8	5.4	13/20/25	48/–	9/13/12	31/–

Note. The edge effect zone at a distance of $0.6(rt)^{1/2}$ (where r is the shell radius) from the bottom edge of the first shell course within the junctions between the shell and the stiffening rings was not considered.

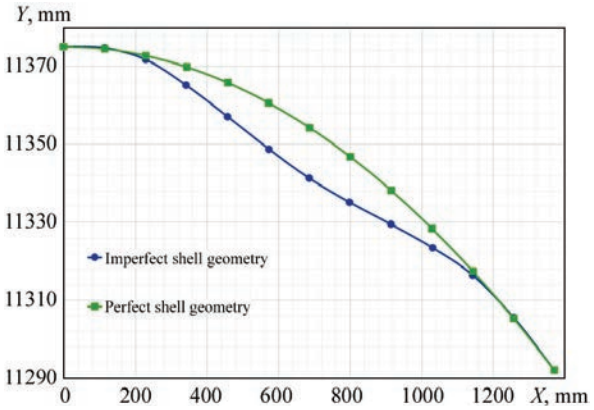

Figure 5. Approximation of geometric shape rectangular depression with 914 mm wide in tank shell

According to EN14015 [5], the maximum local deformation in the vertical and horizontal directions is checked by a 1.0 m long straightedge (template) and should not exceed 16 mm (for a sheet thinner than 12.5 mm). A similar approach is taken in API 650 [6]. Here, local deviations from the design geometry for vertical and horizontal welded joints should not exceed 13 mm (1/2 inch). Deviations should be determined using a 900 mm (36 inch) template.

Let us consider the stress state of the local deviation from the ideal cylindrical shape on the example of an isolated rectangular depression with a length of 914 mm in the circumferential direction and a maximum depth of 13 mm (Figure 5, 6), which spreads along the entire tank shell height and is considered allowable as per API 650 [6]. The results of nonlinear calculation of equivalent stress fields according to the von Mises theory in the middle, inner and outer fibers of the tank shell with an isolated 13 mm deep depression are shown in Figure 6 and Table 2. The strength condition assessment was performed according to API 650 [6] (3) and EN14015 [5] (4):

$$\sigma_{all} = \min\begin{Bmatrix} 0.67 f_y \\ 260 \text{ MPa} \end{Bmatrix} = 160 \text{ MPa}. \qquad (4)$$

Table 2. Calculation results on stresses in tank shell area with 914 mm long and 13 mm deep depression for filling height $H_f = 10$ m

No. course	t, mm	$\sigma_{eq\ mid}/\sigma_{eq\ in}/\sigma_{eq\ out}$, MPa	Δ_{eq}, %	Strength condition assessment according to	
				API 650	EN14015
1	9.2	106/185/210	43–49	–	–
2	7.2	112/188/204	40–45	–	–
3	7.2	101/173/192	42–47	–	–
4	5.4	96/160/174	40–45	–	–
5	5.4	80/140/149	43–46	+	–
6	5.4	54/102/116	47–53	+	+
7	5.4	25/57/75	56–67	+	+
8	5.4	3/10/7	70–57	+	+

Note. The edge effect zone at a distance of $0.6(rt)^{1/2}$ (where r is the shell radius) from the bottom edge of the first shell course was not considered.

The analysis of the obtained data (Figure 6, Table 2) shows that, although the 914 mm wide and 13 mm deep depression is deemed acceptable according to the API 650 [6] standard, the cylindrical tank shell with such a deformation, besides the circumferential membrane stresses, also develops sufficiently large additional bending stresses (40–50 % of σ_{eq}) in the inner and outer fibers. This means that the presence of such depression does not allow meeting the strength condition for the shell as per the standards [5, 6] (Table 2).

The influence of the length of the 13 mm deep depression in the circumferential direction was also assessed for the depression lengths of 914, 1200 and 1500 mm (Table 3) at a filling height of 10 m.

The analysis of the calculation results (Table 3) shows that even when the width (length) of the depression is increased 1.5 times (to 1500 mm), the stresses in the 1st and 2nd courses of the shell exceed the allowable values by 12 %.

This means that it is not always possible to correctly assess geometry tolerance in a deformed shell using a 0.9–1.0 m long template (straightedge), as described

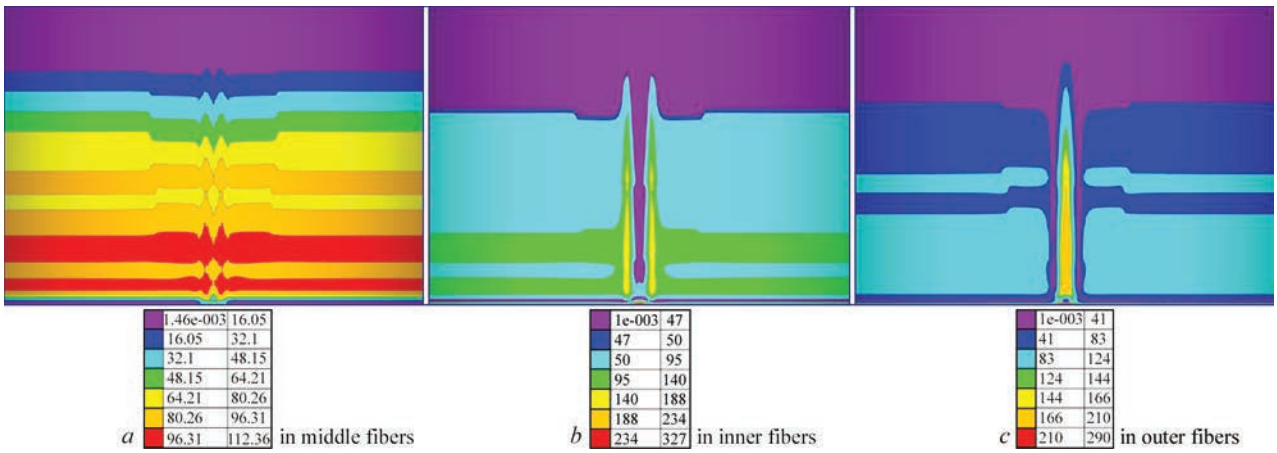

Figure 6. Equivalent (von Mises) stress σ_{eq}, MPa, in shell with rectangular depression with 914 mm wide

Table 3. Calculation results on stresses in repair insert courses of tank shell at filling height H_f = 10 m for 13 mm deep depressions of different lengths: 914, 1200 and 1500 mm

No. course	Stresses for following depression sizes:					
	914×13 mm		1200×13 mm		1500×13 mm	
	$\sigma_{eq\ mid}/\sigma_{eq\ in}/\sigma_{eq\ out}$, MPa	Δ_{eq}/Δ_{all}, %	$\sigma_{eq\ mid}/\sigma_{eq\ in}/\sigma_{eq\ out}$, MPa	Δ_{eq}/Δ_{all}, %	$\sigma_{eq\ mid}/\sigma_{eq\ in}/\sigma_{eq\ out}$, MPa	Δ_{eq}/Δ_{all}, %
1	106/185/210	49/46	109/180/162	39/25	109/161/135	32/12
2	112/188/204	45/42	111/180/158	38/25	109/161/134	32/12
3	101/173/192	47/33	96/160/144	40/11	94/142/120	34/–
4	96/160/174	45/21	94/152/130	38/6	92/132/110	30/–
5	80/140/149	46/4	78/126/109	38/–	75/110/90	32/–
6	54/102/116	53/–	49/90/81	46/–	47/78/63	40/–
7	25/57/75	67/–	19/46/47	60/–	18/40/34	55/–
8	3/10/7	70/–	2/6/5	67/–	2/6/5	67/–

in [5, 6], since it may not ensure compliance with the static strength condition in terms of allowable stresses, which should not exceed 2/3 of the yield strength. If the depression in the circumferential direction is shorter than the length of the template, the actual working stresses in the shell can reach the yield strength.

Thus, the analysis of the actual allowable stress state of the tank shell shows that the standards [5, 6] permit the equivalent stresses exceeding the allowable values in a local area with deviations from the design geometry. The stress exceedance in this case is not standardized and thus the local plastic deformation of metal in the outer and inner fibers of these areas is effectively allowed when the tank is filled.

REFINED STRENGTH CRITERION FOR THE SHELL AREA WITH A DEPRESSION

In view of the above, for the rectangular depression in the tank shell close to the design cylindrical shape, certain additional stresses are allowed, provided that the metal of the insert exhibits elastic behavior. It is important to note that under the action of hydrostatic circumferential and additional stresses, the deformation of the shell is final and does not lead to the destruction of the tank. A similar situation occurs with tanks constructed from coiled sheets. Here, along with the circumferential stresses, the shell also exhibits residual bending stresses from folding and unfolding of the roll [19] (Figure 7). In such a case, the residual bending stress can reach the yield strength of steel.

Thus, considering the above calculation results and the study [16] we propose to formulate the strength condition for the deformed area of the shell as follows:

$$\sigma_{eq} \le \gamma_{dep} S, \quad (5)$$

where σ_{eq} is the equivalent design stresses in the shell; S is the allowable design stress; γ_{dep} is the coefficient determining the value of additional stresses in the depression (insert) relative to the circumferential stresses ($\gamma_{dep} \le 1.10$).

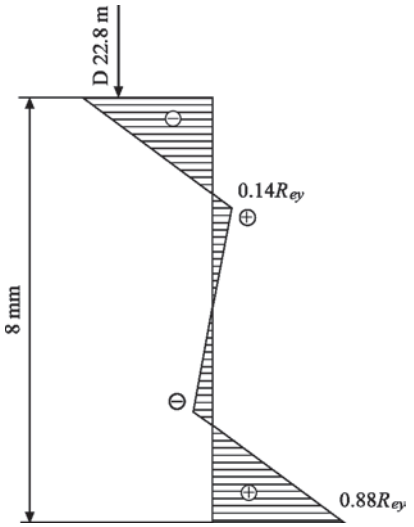

Figure 7. Residual stresses in the lower course of the tank with a volume of 5000 m^3 (D = 22.8 m, H = 12.0 m) when constructed by rolling method [19]. Material of shell is non-alloy structural steel VSt3sp, with yield strength R_{ey} min ≥ 210 MPa (analog of S235 steel). "+" stretched fiber, "–" compressed fiber

The final decision on the possibility of using the tank with initial geometric imperfections should be made and the coefficient γ_{dep} should be determined based on a detailed instrumental inspection of the shell for sharp bends (fractures), corrugations, and areas of plastic deformation, as well as a check of the state of repair welds (angle deformation, results of X-ray inspection or ultrasonic testing, etc.) and their operating conditions (repeated stress mode: quasi-static, low-cycle).

CONCLUSIONS

1. When performing the strength assessment of a cylindrical vertical tank shell with a rectangular depression close to the design cylindrical shape, it is proposed to take into consideration the additional stresses caused by this imperfection by introducing an additional coefficient determining the amount of additional stresses in the depression (insert) relative to the circumferential stress.

The value of the additional coefficient should not exceed 10 % of the allowable circumferential stress and is determined depending on the actual technical condition of the deformed shell section with repair welds.

2. When developing design solutions for repairing the tank shell, one should use such a repair insert design and such welds design that, in the case of welding technology violation (e.g., insufficient transverse shrinkage compensation in vertical welds), would provide a rectangular depression in the tank shell as close to the design cylindrical shape as possible. In this case, the stress state change will be mainly contributed by additional bending stresses, which can make it possible to increase the allowable stresses and, thus, provide the design filling height of oil (oil product) in the tank.

3. Assessing geometry tolerance in a deformed cylindrical shell using a template (straightedge), as per the standards [5, 6] may be insufficient for ensuring the operability of the tank. In the area with allowable local deviations from the design geometry, significant additional stresses may manifest, thus leading to a violation of the strength condition for the tank shell. This may call for an additional calculation analysis of the actual stress state of the cylindrical tank shell for the given imperfection.

REFERENCES

1. Makhnenko, V.I., Barvinko, A.Yu., Barvinko, Yu.P., Tsiarkovsky, P. (2002) Estimation of stressed state of the wall of coiled vertical cylindrical tanks in weldin-in of insert plates. *The Paton Welding J.*, **5**, 2–6.
2. Šapalas, A., Šaučiuvėnas, G., Rasiulis, K. et al. (2019) Behaviour of vertical cylindrical tank with local wall imperfections. *J. of Civil Engineering and Management*, 25(**3**), 287–296. DOI: https://doi.org/10.3846/jcem.2019.9629
3. Liagova, A.A, Samigullin, G.H. (2017) Evaluation of stress-strain state of steel cylindrical tank with dent defect. *Inter. J. of Applied Engineering Research*, **5**, 761–764.
4. EN 1990: *Eurocode — Basis of structural design*.
5. EN 14015: *Specification for the design and manufacture of site built, vertical, cylindrical, flat-bottomed, above ground, welded, steel tanks for the storage of liquids at ambient temperature and above. CEN/TC 265*. Secretariat, BSI, (2017-01), 343.
6. API 650: *Welded tanks for oil storage 13th edition*. API, March 2020.
7. API 653: *Tank inspection, repair, alteration, and reconstruction*. Fifth Edition. API, (November 2014).
8. Maraveas, C., Georgios A. Balokas, K. Tsavdaridis (2015) Numerical evaluation on shell buckling of empty thin-walled steel tanks under wind load according to current American and European design codes. *Thin-Walled Struct.,* **95**, 152–160. DOI: https://doi.org/10.1016/j.tws.2015.07.007.
9. Mahshid Rastgar, Hossein Showkati (2017) Field study and evaluation of buckling behaviour of steel tanks under geometric imperfections. *J. of Applied Mechanical Engineering,* 6(**3**) (January 2017). DOI: https://10.4172/2168-9873.1000268
10. Mahyar Maali, Abdulkadir Cuneyt Aydınl, Hossein Showkati et al. (2018) Longitudinal imperfections on thin walled cylindrical shells. *J. Civil Environ Eng.*, 8:2. DOI: https://10.4172/2165-784X.1000309
11. Rasiulis, K., Gurkšnys, K. (2010) Analyses of the stress intensity of the cylindrical tank wall at the place of the geometrical defect. *J. of Civil Engineering and Management*, 16(**2**), 209–215. DOI: https://doi.org/10.3846/jcem.2010.23
12. Rasiulis K., Samofalov, M., *Šapalas*, A. (2006) Application of the non-linear Fe models to estimate effect of soft defects on thin walls of steel cylindrical tanks. *J. of Civil Engineering and Management*, 12(**2**), 169–179. DOI: https://doi.org/10.3846/13923730.2006.9636389
13. Romanenko K., Samofalov M., *Šapalas* A., Aliphanov L.A. (2004) Linear and physically non-linear stress state analysis of local shape defects on steel cylindrical tank walls by finite element method. Lithuania. *Mechanika*, (**2**) 5–13.
14. EEMUA 159: *Above ground flat bottomed storage tanks: A guide to inspection maintenance and repair.* Publ. 159, Ed. 5, (2017).
15. EN 1993-4-2: *Eurocode 3: Design of steel structures.* Pt 4–2: Tanks.
16. Barvinko, A.Yu., Gotsulyak, E.A. (2003) Determination of admissible deviation of inserts in replacement of an assembly joint in the wall of coiled tanks. *The Paton Welding J.*, **3**, 27–31.
17. EN 1993-1-6: *Eurocode 3. Design of steel structures.* Pt 1–6: Strength and Stability of Shell Structures.
18. Krysko, A.A. (2016) *Geometric and computer modeling of the exploited structures of thin-walled shells of engineering structures, taking into account the imperfections of the geometric shape*. Donbass National Academy of Civil Engineering and Architecture, PhD thesis (2016) 191.
19. Biletsksy, S.M., Golynko, V.M. (1983) *Industrial production of outsized welded sheet structures*. Kyiv, Naukova Dumka.

ORCID

A. Barvinko: 0000-0002-5719-0576
O. Kostenevich: 0000-0002-7427-2805

CONFLICT OF INTEREST

The Authors declare no conflict of interest

CORRESPONDING AUTHOR

A. Barvinko
E.O. Paton Electric Welding Institute of the NASU
11 Kazymyr Malevych Str., 03150, Kyiv, Ukraine.
E-mail: tanksweld@gmail.com

SUGGESTED CITATION

A. Barvinko, Y. Barvinko, A. Yashnik, O. Kostenevich (2022) Evaluation of load bearing capacity of cylindrical shell of above-ground vertical steel welded tank for oil storage after repair. *The Paton Welding J.*, **6**, 22–28.

JOURNAL HOME PAGE

https://pwj.com.ua/en

Received: 25.05.2022
Accepted: 15.08.2022

https://doi.org/10.37434/tpwj2022.06.05

MODERN TECHNOLOGICAL METHODS OF PRESSURE WELDING OF MAGNESIUM ALLOYS (REVIEW)

Yu.V. Falchenko, L.V. Petrushynets

E.O. Paton Electric Welding Institute of the NASU
11 Kazymyr Malevych Str., 03150, Kyiv, Ukraine

ABSTRACT

Proceeding from the results of literature analysis, the good prospects for application of pressure welding methods, namely diffusion, ultrasonic, and roll bonding, when joining elements from magnesium alloys, are shown. Comparative evaluation of bonding modes was performed. The main directions for producing sound joints were determined. It is shown that the main ways to improve the bonding processes are application of the following approaches: monitoring the temperature-time parameters of bonding, application of interlayers in the form of separate layers from similar materials, based on copper, nickel, zinc or silver, or of eutectic mixtures, butt joint strengthening through application of nano- or finely-dispersed particles, intensification of plastic deformation through superposition of ultrasonic oscillations, increase of plastic deformation intensity, as well as application of heat treatment before and after bonding.

KEYWORDS: magnesium alloys, welded joints, microstructure, strength, diffusion bonding, ultrasonic bonding, roll bonding

INTRODUCTION

Magnesium is one of the most widely spread elements on Earth. By estimates of total quantity, it is in the fourth place after iron, oxygen and silicon and in the eighth place in terms of its content in the earth's crust. The main advantage of application of magnesium alloys is their low weight: magnesium has one of the lowest densities among the structural materials [1]. Its active application is slowed down because of low ductility and formability at room temperature, presence of basic texture, edge cracking at rolling and high electrochemical activity [2].

Development of new alloys and introduction of modern processing methods promotes wider acceptance of magnesium in automotive and aviation industry. Over the recent years, magnesium alloys became wider applied in manufacture by large car companies, including General Motors, Ford, Volkswagen and Toyota. Dashboard elements, gearboxes, steering components and radiator supports are made from this group of materials. Such aircraft elements as brackets, compressor upper case for air conditioning mounting, door fasteners, twisted-blade impeller, antenna supports, window frame, parts of turbofan engine gearbox, etc. are already made from magnesium alloys [1, 2].

As magnesium becomes ever wider applied in manufacture of diverse components, there is the need to develop joining methods, which would provide the appropriate properties of the produced structural elements.

It is known, however, that the traditional technologies of fusion welding of magnesium alloys cause considerable softening of the material in the joint zone, formation of cast coarse-crystalline weld structure and of characteristic defects, such as pores, microinclusions of oxide films and cracks, which are due to metal melting and crystallization in the zone of permanent joint formation [3, 4].

Solid-phase welding processes can be effective methods of improvement of weld reliability, making impossible the formation of defects characteristic for fusion welding.

Considering the above-said, the objective of this work was to perform analysis of the techniques applied in pressure welding of magnesium alloys. These include rolling, diffusion and ultrasonic bonding and their combinations.

Figure 1 gives the main technological measures, which are used in roll, ultrasonic and diffusion bonding. Friction stir welding is not considered in this paper in view of the specific features of its impact on the joint zone, which make it essentially different from the above processes.

We will consider the publications of recent years devoted to this issue [5–31].

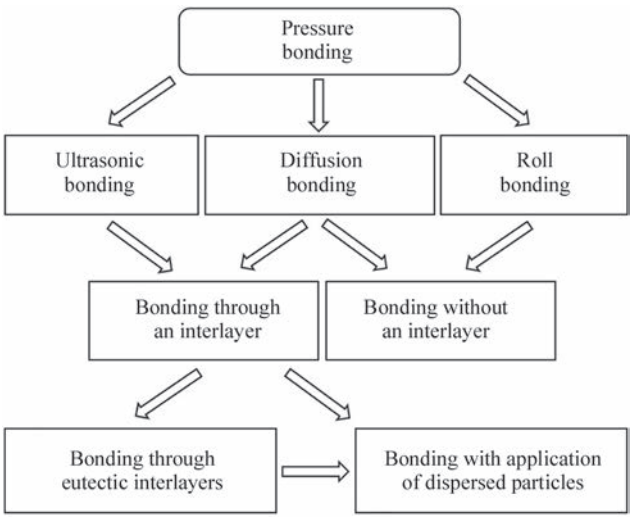

Figure 1. Main methods of pressure bonding of magnesium alloys

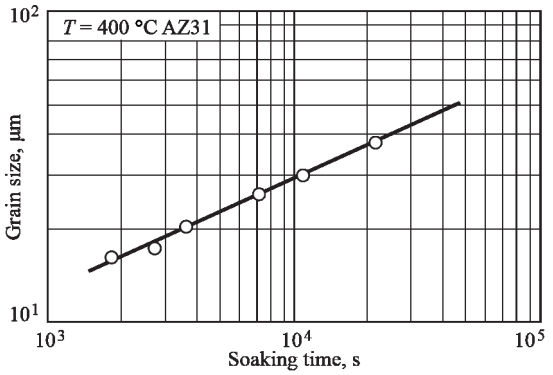

Figure 2. Interrelation between grain size and sample heating time at the temperature of 400 °C [6]

DIFFUSION BONDING

The main parameters in diffusion bonding (DB) are temperature, pressure and soaking time. In works [5–8] the influence of grain size and bonding parameters at sample heating in air on formation of the structure and mechanical properties of the joints were considered.

In work [5] when studying pure magnesium joints the following parameters were varied: temperature from 300 to 400 °C, pressure from 2 to 20 MPa, soaking time from 15 to 4320 min. Maximum values of shear strength of 95.7–109.4 MPa (88.8 % of base material strength) were achieved in the following mode: T = 400 °C, P = 20 MPa, t = 60 min. The joint line in such samples is not identified by optical microscopy. It is noted that the average grain size in the magnesium alloy was close to 85 μm in the initial condition.

When joining AZ31 alloy (Mg–3Al–1Zn, wt.%) [6], its preliminary annealing at 400 °C was performed for 30 min. Average grain size after this operation was 16.8 μm. Diffusion bonding was conducted in air at the temperature of 400 °C, pressure of 2–10 MPa, and soaking for 30–400 min. Here, superplasticity is observed in the alloy.

As shown by studies, conducted by the authors, increase of bonding time for samples from AZ31 magnesium alloy leads to increase of grain size (Figure 2).

During bonding, pores form between the contacting surfaces, the heating of which requires application of higher pressure or longer bonding time. Maximum values of shear strength of 74.2–80.5 MPa (85 % of that of the initial metal) were obtained in the following mode: T = 400 °C, P = 3 MPa, t = 180 min. The joint line in such samples is not revealed by optical microscopy.

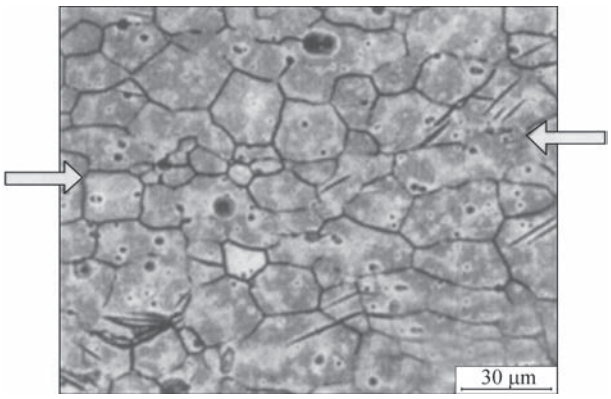

Figure 3. Optical microstructure of the joint zone of samples produced under pressure of 3 MPa for 180 min [6]

In work [7] studies of AZ31 alloy (Mg–3Al–1Zn, wt.%) were carried ont, when it demonstrated superplastic behaviour and at lowering of bonding temperature to 200–300 °C. Material was used after hot pressing and rolling. Average grain size was 8.5 μm. The authors note that the initial alloy grain size has an essential influence on the temperature, at which the superplastic properties are manifested, for instance for 16 μm grain size it is 300 °C, while for 8.5 μm it is 200 °C. Thus, such bonding temperature and pressure were selected, at which the alloy superplastic properties were manifested: 250–300 °C and 15–30 MPa, respectively. The process was conducted in air, and its duration was 60–120 min.

At bonding temperature of 250 °C, a clear contact line and pores are observed in the butt joint. Temperature rise allows lowering the defect rate in the joint zone. However, increase of soaking time up to 120 min leads to excess grain growth, and, consequently, to lowering of the produced joint strength. Maximum shear strength τ = 68.5 MPa (80.3 % of initial material strength) was achieved in the following mode: T = 300 °C, P = 20 MPa, t = 60 min.

The influence of grain size on formation of joints of AZ31 magnesium alloy at diffusion bonding was considered in [8]. Samples after annealing at 400 °C for 30 min with average grain size of 28 and 11 mm were used. Diffusion bonding was conducted in air at the temperature of 400 °C, pressure of 2–10 MPa, and soaking for 30–600 min.

It was shown that the grain size of the initial metal has an essential influence on the process of joint formation, and its coarsening requires application of a more stringent control of the bonding modes to produce strong joints. This is attributable to the dependence of metal superplastic behaviour on grain size. So, in the case of samples with grain size of 28 μm, the optimal mode is as follows: T = 400 °C, P = 5 MPa, t = 180 min, and for grain size of 11 μm it is: T = = 400 °C, P = 3 MPa, t = 120 min. Shear strength here is 74.5–81.1 MPa (90 % of that of the initial metal) and 81.4–85.1 MPa (92 %), respectively. The authors proposed a model of joint formation, which includes both the diffusion processes and plastic deformation of the subsurface layers. Recommendations are given for selection of bonding time at different pressure values, depending on base metal grain size.

In works [9–11] diffusion bonding of magnesium alloys was studied under the vacuum conditions.

In work [9] vacuum diffusion bonding (VDB) of extruded AZ31 magnesium alloy (Mg–2.5–3.5Al–0.5

–1.5Zn–0.2–0.5Mn — up to 0.1Si — up to 0.05Cu — up to 0.005Fe – up to 0.005Ni, wt.%) was performed. In order to obtain initial material with specified average grain size of 14.1 μm, preliminary isothermal annealing was conducted at 300 °C for 30 min. Bonding process parameters were assigned in the following ranges: temperature of 390–480 °C, pressure of 8 MPa, soaking time of 60–120 min, and degree of rarefaction in the chamber of 14 Pa.

Investigation results showed that bonding temperature and soaking time had a key influence on joint quality. At temperature below 420 °C, the diffusion processes in the butt joint are running slow, the contact line is clearly visible and the shear strength of such samples is low. At T = 450–480 °C partial disappearance of the contact line, essential grain growth and strength decrease take place. During soaking for 90 min, the diffusion processes are the most complete, sample strength grows, and further increase of bonding time leads to a slight decrease in strength, because of grain coarsening. The following mode was determined to be the optimal one: temperature of 420 °C, pressure of 8 MPa, and soaking for 90 min. Under these conditions, samples with maximum value of shear strength τ = 76.2 MPa were produced.

The authors of work [10] studied the features of joint formation at VDB of ZK60 magnesium alloy (Mg–6Zn–0.35Zr, wt.%). Average grain size was 11.9 μm. Bonding was conducted at the temperature of 300–400 °C, pressure of 1–20 MPa, soaking for 30–90 min, and vacuum of 0.27 Pa. Proceeding from the conducted mechanical investigations of the samples, the following mode was determined as the optimum one: temperature of 380 °C, pressure of 20 MPa, and soaking for 90 min. Shear strength of such joints is equal to 65.8 MPa (82 % of base metal strength). At lower values of mode parameters, the contact line and individual pores are visible in the butt joint. Exceeding the recommended values leads to excess growth of the grain, and, consequently, to a certain loss of strength. During bonding in the optimal mode, the average grain size increases from 11.9 to 21.2 μm. Up to certain limits, this process has a positive effect on sample quality, as the main mechanism of joint formation is atom diffusion and slipping of the initial grain boundaries, caused by grain growth.

In work [11] vacuum diffusion bonding of AZ61 magnesium alloy (Mg–5.8–7.2Al–0.4–1.5Zn–0.1–0.4 Mn — up to 0.3Si — up to 0.05Cu — up to 0.05Fe — up to 0.05Ni, wt.%) was performed. Preliminary recrystallization annealing at 300 °C for 30 min allowed reducing the average grain size from 20.48 to 14.29 μm. VDB was conducted at the temperature of 430–490 °C, pressure of 10 MPa, soaking time of 60–120 min. Degree of rarefaction is not given.

Metallographic investigations of samples, produced in the proposed modes, showed that a clear contact line remains in all the cases. However, its thickness decreases with increase of bonding temperature and pressure. At the same time, application of higher bonding temperature leads to excessive grain growth, and, consequently, to deterioration of the mechanical properties of the joints. Proceeding from experimental results, it was found that the maximum shear strength of 51.95 MPa (46.78 % of base metal strength) can be obtained in the following mode: T = 470 °C, P = 10 MPa, t = 90 min. Microhardness values of such samples are higher in the joint zone, than in the base metal (*HV* 82.48 against ~ *HV* 65) that is attributable to plastic deformation of the subsurface layers during bonding.

In work [12] it is proposed to perform heat treatment of the produced joints in order to improve their strength. The authors studied vacuum diffusion bonding of AZ91 alloy (Mg–9Al–1Zn, wt.). Recrystallization annealing was performed at 300 °C for 30 min with the purpose of grain refinement. Average grain size was 12.31 μm. Samples were bonded in vacuum of 18 Pa in the following mode: temperature of 430–490 °C, pressure of 10 MPa, and soaking time of 60–120 min. After bonding in the proposed modes, the contact line is clearly visible in all the samples, and considerable grain grown is found at a combination of high temperature with long-term soaking. Maximum shear strength of as-welded joints was equal to 64.7 MPa, respectively, and the following mode was determined to be the optimal one, respectively: T = 470 °C, P = 10 MPa, t = 90 min. Annealing of the joints was performed to improve their mechanical properties. Heat treatment was conducted at 320–380 °C for 60 to 300 min. An increase of their shear strength was achieved in all the modes, maximum values τ = 76.93 MPa were obtained at the temperature of 350 °C and soaking for 240 min. The joint line practically disappears here, the grains in the butt joint are fine, their size, however, gradually increasing with greater distance from the weld.

From the above works [5–12] on bonding magnesium alloys without using interlayers we can come to the conclusion that it is desirable to apply the bonding modes, not leading to considerable grain growth. Additional heat treatment allows somewhat increasing the joint strength, due to running of the recrystallization processes.

The possibility of application of interlayers of different chemical composition at diffusion bonding was studied in works [13–24].

In work [13] 50 μm thick copper foil was proposed as interlayer for VDB of AZ31B magnesium alloy (Mg–2.5–3.5Al–0.5–1.5Zn–0.2–0.5Mn–0.1Si–0.05 Cu–0.005Fe, wt.%). Bonding was performed at the temperature of 480 °C, pressure of 10 MPa, soaking for 30 min, and vacuum of 10^{-2} Pa.

Sound joints were produced, in the microstructure of which formation of three layers is observed (Figure 4).

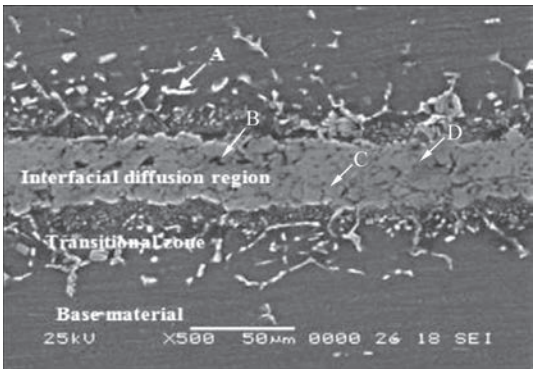

Figure 4. Microstructure of the joint zone of AZ31B alloy using a Cu interlayer, where A, B, C, and D are different areas of the diffusion zone [13]

The total thickness of the diffusion zone is 115 μm. The central layer of light-grey colour with black inclusions 35 μm thick is a mixture of Mg_2Cu (region D), $MgCu_2$ phases (region C) and Mg(Cu) solid solution (region B). The layers adjacent to the magnesium alloy (each 40 μm thick) are a dark-grey base with white, predominantly elongated inclusions (region A) and consist of Mg(Al,-Cu) solid solution and $Mg_{17}(Cu,Al)_{12}$ phase, distributed in it. Copper atoms demonstrate rather high activity in AZ31B alloy. On Mg/Cu interface copper diffuses along the grain boundaries into the base metal, forming a white compound. Joint formation is considered as a result of diffusion along the grain boundaries and dislocations, as well as solid-phase transformations. Microhardness distribution in the joint zone is of a steplike nature and gradually increases from the magnesium alloy to the central layer of the butt joint, where it is close to *HV* 100 that is by *HV* 50–60 higher than that in the base material.

The authors of work [14] applied a thinner layer of copper of thickness δ = 20 μm for bonding Mg–3Al–1Zn, wt.% alloy. Bonding was performed in argon atmosphere at the temperature of 530 °C, pressure of 0.7 MPa, and soaking for 5–120 min.

The authors divide the joint formation process into four stages: plastic deformation and diffusion in the solid state; dissolution of the interlayer and the base metal; isothermal crystallization and homogenizing (Figure 5, *a–c*). At the first stage (t = 5 min) drawing together of the contacting surfaces and their microplastic deformation take place. The second stage (t = 5–15 min) includes formation of the liquid phase as a result of a eutectic reaction that is accompanied by dissolution of the interlayer and part of the base metal. The joint zone here consists of solid solution of magnesium and $CuMg_2$ eutectic. At the stage of isothermal crystallization (t = 15–60 min), a gradual increase of the content of $CuMg_2$ phase occurs, as a result of intensive diffusion of copper into the base metal, that is accompanied by grain growth and appearance of a clear joint line in the center of the butt joint. The fourth stage is completion of the process of homogenizing of the joint zone, which is a solid solution of magnesium with $CuMg_2$ phase, distributed along the grain boundaries. The joint line losses its clear contours. Experimental results showed that the shear strength of the joints directly depends on bonding duration (Figure 5, *e*). With short bonding time (5–30 min) the mechanical properties of the joints are at a low level, because a too large quantity of brittle $CuMg_2$ phase remains in the butt joint, and at a too long bonding time (30–120 min) — because of intensive grain growth, combined with accumulation of $CuMg_2$ phase on grain boundaries. The following mode was determined to be the optimum one: T = 530 °C, P = 0.7 MPa, t = 30 min (Figure 5). Shear strength of the joints in this case is 70.2 MPa (85.2 % of base metal strength).

In work [15] bonding of AZ31 magnesium alloy was performed through an interlayer of copper and copper with tin. Copper 5 μm thick was applied on the sample surface by vacuum evaporation method. In part of the experiments tin foil 50 μm thick was additionally used. Bonding was conducted in argon at the temperature of 520 °C and pressure of 0.5 MPa, varying the soaking in the range of 10 50 min. Heating up to bonding temperature was conducted for approximately 2 min, and cooling to room temperature was performed together with the chamber.

It is shown that at application of the copper coating a diffusion zone 50–70 μm thick forms in the butt joint, its size decreasing with longer soaking time. It consists of solid solution of Mg and Cu_2Mg phase, and defects in the form of pores are present. Application of a combined interlayer of Cu coating and Sn foil allows producing a sound joint with a more uniform nature of element distribution in the butt joint and higher values of shear strength. The joint area consists of solid solution, enriched in Mg, and individual inclusions of Cu_2Mg phase. Sn layer does not take part in formation of intermetallic phases and freely diffuses in-depth of the magnesium alloy. Microhardness values in the butt joint are close to those of the base metal (68–70 VHN against ~ 58 VHN). Shear strength of the joints increases with longer soaking duration. However, after soaking for 30 min it almost does not change (τ = 64 MPa at t = 30 min and τ = = 67 MPa at t = 50 min).

Authors of work [16] used pure copper, as well as a combination of copper with nanoparticles of TiO_2, Al_2O_3 or SiC, as an interlayer in bonding AZ31 magnesium alloy (Mg–2.5–3.5Al–0.7–1.3Zn–0.3Si–0.2Mn –0.05Cu–0.005Fe–0.005Ni, wt.%). A galvanic coating from pure copper 20 μm thick was applied on the sample surface after cleaning. For additional deposition of the nanoparticles they were added to the electrolyte solution in the quantity of 10 g/l. TiO_2 and SiC nanoparticles of 20 nm size, and Al_2O_3 nanoparticles of 20 and 50 nm size were used. Bonding was conducted in the atmosphere of argon at the temperature of 525 °C, pressure of 1 MPa, and soaking for 60–120 min.

It is shown that increase of bonding time in all the cases promotes a more complete running of isother-

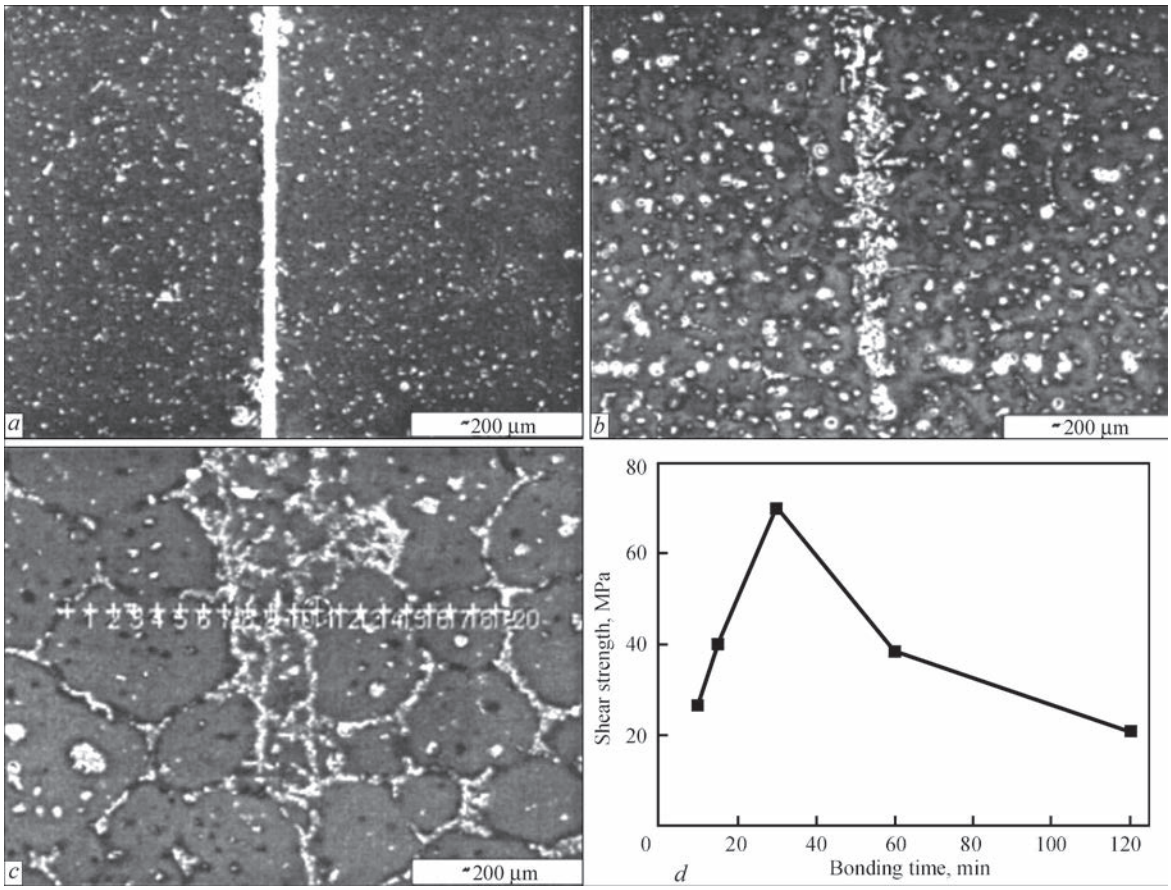

Figure 5. Microstructure of joints produced at 530 °C at bonding time of 5 min (*a*), 30 (*b*), 120 (*c*) and graph of dependence of shear strength on bonding time (*d*) [14]

mal crystallization process and allows producing a more homogeneous joint. When pure copper coating is used, a continuous interlayer of AlCuMg phase remains in the joint zone, along which microcracks are observed. At application of a copper interlayer with SiC particles a considerable quantity of Mg_2Cu phase forms in the central part of the butt joint, the presence of which is the cause for brittle fracture of such samples. In the case of an interlayer of copper with Al_2O_3 it was shown that increase of nanoparticle size from 20 to 50 nm leads to decrease of strength values. Here, a mixture of Mg_2Cu, AlCuMg phases and intermetallic phases of Al–Cu–Mg system, enriched in magnesium forms in the joint zone, and individual microcracks are observed. The highest shear strength of 31.66 MPa (98 % of that of the base metal) was found in samples bonded through an interlayer of copper with TiO_2 in the following mode: T = 525 °C, P = 1 MPa, t = 120 min. An accumulation of AlCuMg phase particles is observed in the joint zone (Figure 6). Uniform distribution of nanoparticles in the interlayer in this case inhibits crack initiation and propagation.

The authors of work [17] used aluminium foil 9 and 14 μm thick as an interlayer for bonding AZ31magnesium alloy (Mg–2.54Al–0.71Zn–0.09Si–0.03Mn–0.03Cr –0.03V–0.01Ti, wt.%). Bonding was performed at the temperature of 440–450 °C, pressure of 2 MPa, soaking for 45–120 min, and vacuum of 2.7 Pa.

The joint zone consists of three layers, and the aluminium content gradually decreases from the butt joint center to the base metal. At other conditions being equal, the joints, obtained through 9 μm foil have higher strength, that is attributable to a more complete running of the process of isothermal crystallization and formation of a smaller volume of $Al_{12}Mg_{17}$. At more than 75 min bonding duration, intensive grain growth occurs, leading to strength drop. The joint zone microhardness is up to three times higher than that in the base metal, while greater foil thickness leads to a certain increase of butt joint hardness. The following conditions were determined to be the optimal ones for joint formation: T = 440 °C, P = 2 MPa, t = 75 min and intermediate layer thickness of 9 μm. The shear strength was ~ 35 MPa.

The authors of work [18] considered the possibility of using silver foil 100 μm thick as an interlayer at vacuum diffusion bonding of AZ91 magnesium alloy (Mg–9Al–1Zn, wt.%). Bonding was conducted at the temperature of 480 °C, pressure of 1 MPa, and soaking for 30–120 min in the vacuum of $2 \cdot 10^{-3}$ Pa.

Sound joints were produced. During the bonding process, melting of the material on the boundary of AZ91 alloy/Ag foil and active diffusion of atoms between base material and the interlayer take place with silver gradually dissolving in the magnesium alloy matrix. The shear

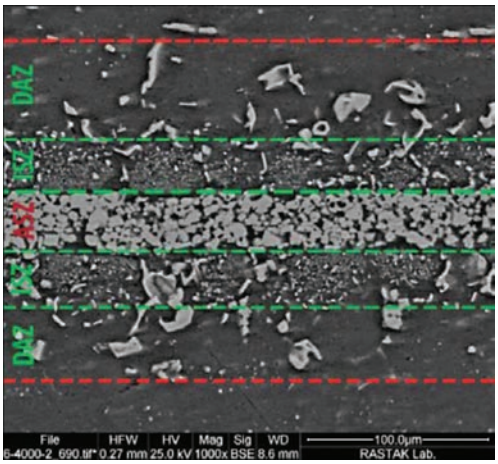

Figure 6. Microstructure of AZ31 alloy joint produced with application of a copper interlayer with TiO_2 nanoparticles [16]

strength of the joints is almost independent on bonding duration and it is in the range of 65–70 MPa (against ~120 MPa for base metal after annealing). The microstructure and chemical composition of the joint zone of samples produced at different soaking are similar.

In work [19] bonding of AZ31 magnesium alloy (Mg–2.99Al–0.96Zn, wt.%) was conducted through an interlayer of silver 50 μm thick. Bonding was performed at the temperature of 480–500 °C and soaking for 60 min.

In samples produced at T = 480–490 °C a eutectic layer is observed in the central part of the weld and diffusion layers are found at the boundary with base metal. In bonding at 500 °C just a thin eutectic layer forms in the joint zone. The composition of the found phases also changes with temperature rise. At 480 °C, a mixture of $AgMg_4$ intermetallic and $AgMg_3$ eutectic of the total width of 40 μm is formed in the butt joint. At 490° C a joint zone of approximately 100 μm width is formed, where the diffusion layers consist predominantly from a solid solution, enriched in Mg, and the central region consists of $AgMg_3$ eutectic. At 500 °C the interlayer with Ag almost disappears as a result of diffusion into the base metal, leaving a thin eutectic layer (~ 6 μm). It is noted that increase of bonding temperature also has a positive influence on microhardness of the joint zone, its value dropping from *HV*0.05–170 (*T* 480 °C) to *HV*0.05–80 (*T* = 500 °C). Shear strength is just 39 MPa at optimum bonding temperature that is two times lower than in the base metal.

The authors of [20] used a nickel interlayer at VDB of AZ31 magnesium alloy (Mg–3Al–1Zn, wt.%). The bonding process was conducted in the following mode: temperature of 515 °C, pressure of 0.16 MPa, soaking for 5–120 min, and vacuum of 0.053 Pa.

After bonding three diffusion layers, located symmetrically relative to the butt joint center, can be singled out in the joint zone. The central layer, which consists of a eutectic, gradually decreases and disappears with increase of soaking time to 60 min that is indicative of a complete isothermal crystallization of the weld. Directly adjacent to it are intermetallic layers, the thickness of which is increased with longer bonding time. At soaking in the range of 20–30 min the layers adjacent to the base metal, first become wider, and then decrease in size. It is attributable to gradual homogenizing of the joint zone, as interdiffusion of the interlayer and base metal elements takes place. Increase of bonding time to 120 min leads to strength drop that was related to formation and segregation of brittle intermetallics of Mg–Ni system. The following mode was determined as the optimum one: T = 515 °C, P = 0.16 MPa, t = 60 min. Under these conditions a joints with maximum shear strength of 36 MPa were produced, the microhardness being 179 VHN that is three times higher than in the magnesium alloy (55 VHN).

In work [21] AZ31 magnesium alloy (Mg–3Al–1Zn, wt.%) was bonded through a nickel coating. Nickel of 5 μm thickness was deposited by vacuum evaporation. Bonding was performed in the following mode: temperature of 520 °C, pressure of 8 MPa, soaking for 5–60 min, and vacuum of $1.33 \cdot 10^{-3}$ Pa.

In the first minutes of joint formation regions enriched in nickel are still observed in the butt joint. Increase of bonding duration up to 30 min promotes Ni diffusion and more complete passage of isothermal crystallization process. Maximum values of shear strength τ = 46.2 MPa were obtained at 20 min soaking. At greater duration of the process, intensive grain growth is observed in the butt joint alongside formation of Mg_2Ni brittle phase, leading to strength drop in such joints.

The authors of [22] considered the possibility of applying SiC particles as a reinforcing element of the butt joint in vacuum diffusion bonding of AZ91 magnesium alloy (Mg–8.25Al–0.63Zn–0.22Mn–0.035 Si–0.014Fe–0.03Cu–0.002Be, wt.%). Bonding was conducted at the temperature of 420 °C, pressure of 10 MPa, with 60 min soaking. SiC particles of 10–45 μm size in the ratio of 2–6 % were placed between the magnesium alloy surfaces.

It is shown that application of reinforcing particles allows increasing the shear strength almost two times, compared to bonding without interlayers (109 MPa against 63 MPa). The optimum size and concentration were determined to be 10–25 μm and 4 %, respectively. A too large volume of the particles leads to slowing down of the diffusion processes and SiC accumulation in certain regions of the butt joint that leads to lowering of ductility of such joints and their fracture at lower strength values.

It follows from the above that in bonding through eutectic interlayers it is necessary to control the process of brittle phase formation through reduction of bonding time, as well as limited formation of the liquid phase that is achieved by using thinner foils/coat-

ings. Application of reinforcing particles of an optimum size and concentration can significantly increase the strength of the produced joints.

In works [23, 24] the influence of plastic deformation on welded joint formation was studied.

In work [23] bonding of AZ31 magnesium alloy ((Mg–3.04Al–0.99Zn–0.29Mn–0.02Si–0.01Fe–0.0Cu, wt.%)) was performed in two stages: hot deformation and annealing. Compression was performed at the temperature of 350 °C, strain rate of 0.1 s^{-1}, and degree of deformation of 10–60 %. The samples were heated to the specified temperature and compressed up to specified upsetting, leaving them under pressure for 3 min more. Then they were welded into vacuum tubes, and soaked for 400 °C at 60–720 min.

Increase of the degree of deformation to 40–60 % promotes passage of dynamic recrystallization of grains in the butt joint, and initial line of adhesion takes a wavelike shape. Growth of new grains at the interface and their gradual growth into adjacent deformation regions lead to migration between the grains and partial disappearance of the interface (Figure 7).

Annealing for 60 min leads to a certain growth of the recrystallized grains. Increase of soaking time to 120–240 min promotes formation of a more ramified contour of the grain boundaries, their size increasing only slightly. The interface disappeared completely after soaking for 480 min. Further increase of annealing duration leads to undesirable coarsening of the grain that has a negative influence on the mechanical properties of such joints. Maximum tensile strength of 164.7 MPa was found in samples, which were joined with 60 % degree of upsetting and annealed for 480 min that is by 9% higher than in samples soaked for 60 min.

The authors of work [24] studied the features of formation of joints of WE43 magnesium alloy (Mg–4Y–3Nd–0.5Zr, wt.%). Samples were heated up to 450–525 °C and compressed, setting the strain rate of 0.001 — 1 s^{-1} and degree of strain of 5–50 %. After heating to the specified temperature, they were compressed and quenched in water.

In the joint zone a rapid dynamic grain growth takes place under the conditions of low strain rate of 0.001 s^{-1} and high bonding temperature of 525 °C, leading to strength lowering (σ_t = 114.43 MPa). In case of conducting the process at the temperature of 450 °C or high strain rate, grain refinement in the joint zone is controlled by dynamic recrystallization.

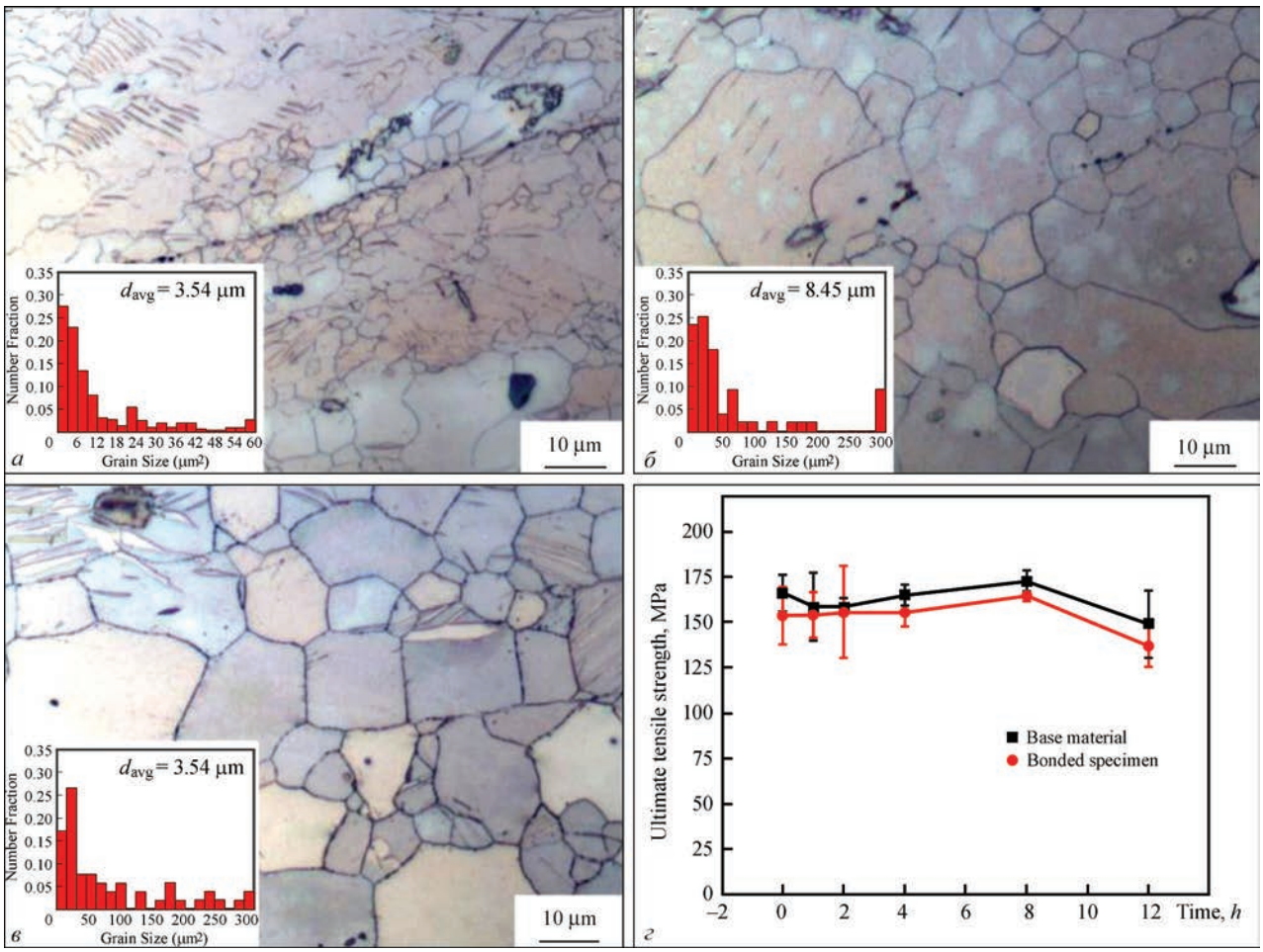

Figure 7. Microstructure of the joint zone and distribution of grain size in samples produced at the temperature of 350 °C, at the degree of deformation of 0.6 with subsequent heat treatment at 400 °C for: *a* — 60; *b* — 240; *c* — 480 min. Graph of the influence of heat treatment time on shear strength of the joints (*d*) [23]

It is shown that bonding performance at a high strain rate of 1 s^{-1} leads to a considerable drop of ductility, compared to the initial alloy (3.56–5.51 % against 12.17 %). The highest values of rupture strength of 158.60 MPa were obtained for samples joined at the temperature of 450 °C and strain rate of 0.001 s^{-1}, with ductility being 6.99 %.

ULTRASONIC BONDING

In the works on ultrasonic bonding of magnesium alloys [25–28] oscillations are additionally used, alongside parameters characteristic for diffusion bonding (heating temperature, pressure) that allows essentially shortening the bonding time.

In work [25] bonding of ME20M magnesium alloy (Mg–1.3–2.2Mn–0.15–0.35Ce–0.3Zn, wt.%) was conducted through an interlayer of pure Zn 50 μm thick. Samples from ME20M alloy were welded in the inductor in air at the temperature of 370 °C, pressure of 0.15 MPa, and soaking up to 2 min. Ultrasound of 200 W power at the frequency of 20 kHz was used as an additional source of intensification of joint formation.

It was not possible to produce joints in the proposed mode without ultrasonic oscillations. Application of ultrasound promotes breaking up of the oxide film at contact surfaces, accelerates the eutectic reaction, intensifies Mg and Zn diffusion in the eutectic liquid and accelerates the process of isothermal crystallization. Already after one second of ultrasound action, the zinc interlayer transforms into a two-phase gray layer, the main part of which consists of $Mg_{51}Zn_{20}$ with acicular MgZn inclusions. Increase of bonding time (Figure 8) causes a gradual decrease of the thickness of the central eutectic layer and its disappearance as a result of completion of the process of isothermal crystallization with formation of Mg(Zn) solid solution with individual inclusions of MgZn phase. The highest average shear strength of the joints of 106.4 MPa was obtained for samples, where bonding time was 2 min.

In publication [26] foil of N_{26} alloy (Cu–38Zn) 20 μm thick was used as an interlayer. Bonding was conducted at the temperature of 460 °C, pressure of 0.15 MPa, process duration of 0.05–1.5 min, ultrasound frequency of 20 kHz and power of 500 W.

It is shown that increase of bonding time promotes a gradual dissolution of the interlayer with formation of $CuMg_2$ and CuMgZn phases, which, in their turn, disappear as a result of formation of a solid solution in the butt joint. The process of isothermal crystallization is fully completed after 1.5 min. The oxide films are fragmented, partially pressed out of the butt joint with the liquid phase, and their remains are arranged in two strings along the base metal. Samples, produced at bonding time of 1.5 min, had shear strength at the level of base metal (105 MPa).

The authors of [27] studied the possibility of ultrasound application in bonding AZ31B magnesium alloy. Zn foil 0.5 mm thick was used as an interlayer. Oscillation frequency was 20 kHz. Bonding was conducted in air at the temperature of 360–380 °C, pressure of 0.36 MPa, and soaking of 0.02 min.

It was shown that at bonding temperature of 360–380 °C a layer of $MgZn_2$ intermetallic with a string of pores in the middle, eutectic layers on the boundary of contact with the base metal and thin MgZn inclusions on the interface between $MgZn_2$ and eutectic form in the center of the butt joint. Here, temperature rise promotes thinning of the central layer. At 380 °C the zinc foil reacts completely with magnesium, forming a eutectic structure with inclusions of magnesium-based solid solution. Maximum shear strength of 42 MPa was demonstrated by samples produced at the temperature of 380 °C.

The work shows a diagram of joint formation through a liquid interlayer (Figure 9). Dense oxide layers were present on the surfaces of magnesium alloy and Zn before bonding. After heating up to bonding temperature and switching on the ultrasonic oscillations, the oxides start breaking up, and a liquid phase forms in their place. Active diffusion of Mg and Zn promotes a fast formation of a large quantity of liquid, breaking up of oxide remains and their pressing out into flash. Mg atoms diffuse into Zn interlayer, forming $MgZn_2$ and MgZn in the solid state. The liquid phase forms a eutectic structure, at the boundary with the base metal.

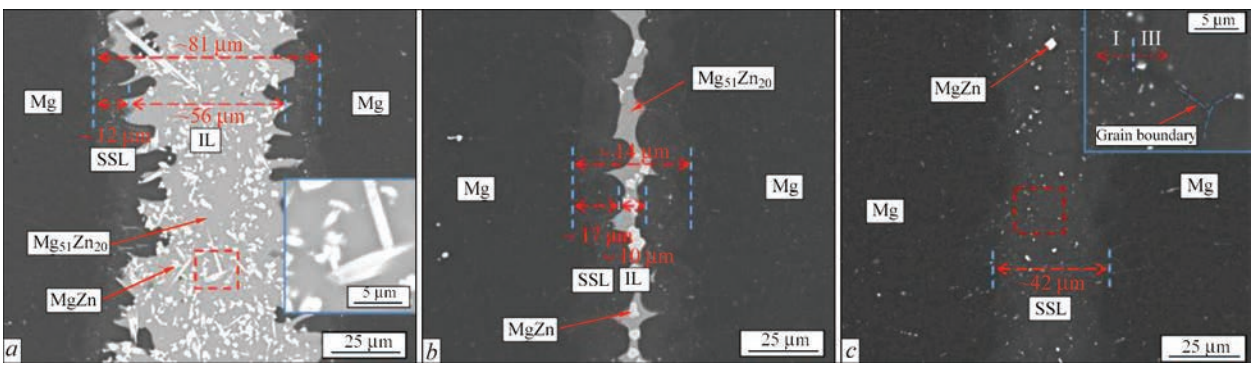

Figure 8. Microstructure of the joint of ME20M alloy, using Zn interlayer and ultrasonic oscillations at process time of: *a* — 0.02; *b* — 0.5; *c* — 2 min [25]

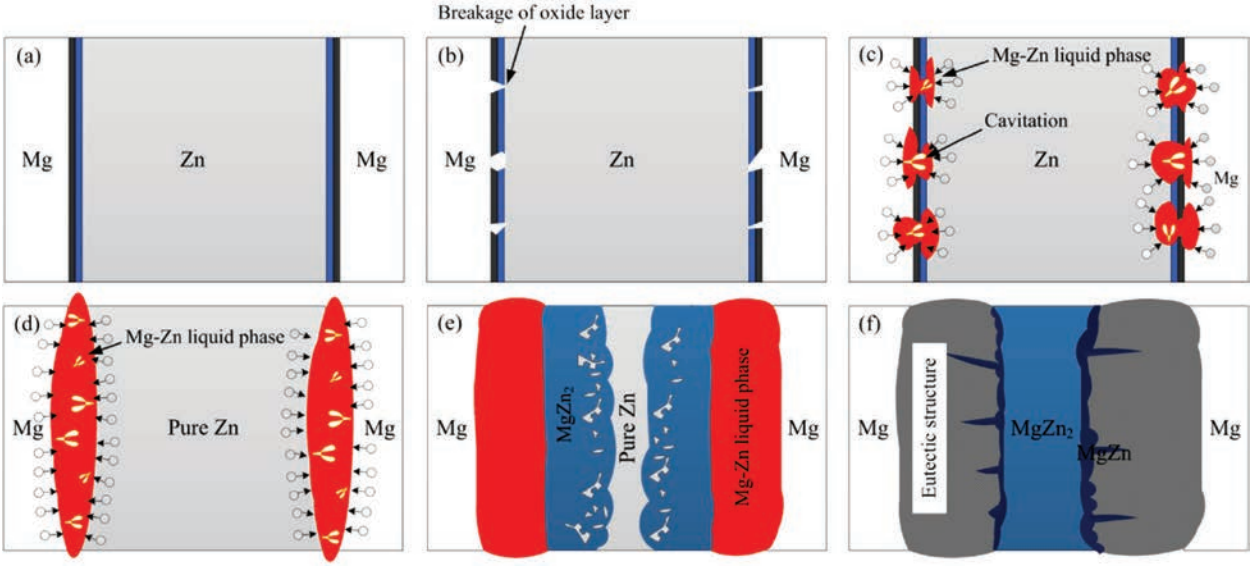

Figure 9. Scheme of the mechanism of joint formation through a liquid interlayer [27]

In work [28] the influence of pulse power on the quality of joints of AZ31B magnesium alloy was studied. Zinc foil 0.5 mm thick was used as an interlayer. Bonding was conducted in air at the temperature of 360 °C and pressure of up to 0.4 MPa. Working frequency was 20 KHz with the power of 333–1000 W.

Investigations showed that the oxide is completely removed from the magnesium alloy surface already after one second of ultrasound action. A wide joint zone (~1.2 mm) forms in the butt, which consists of a layer of $MgZn_2$ with inclusions of Zn in the central part and of Mg/Zn eutectoid structures on the boundary with the base metal, and MgZn inclusions are observed between both the layers. Increase of bonding time promotes a reduction of the size of the central zone, from which individual longitudinal inclusions remains already after 3 s. In the joints produced at higher power of ultrasound, smaller residual porosity and greater width of the butt joint with thicker eutectoid layers are observed. At sonotrode pressure of 0.4 MPa a joint zone 120 μm wide, completely consisting of the eutectoid phase, forms in the butt joint. Investigations of mechanical properties showed that joints, which completely consisted of the eutectoid structure, had the highest shear strength of 40 MPa.

Application of ultrasound at magnesium alloy bonding allows reducing the duration of the process of joint formation several times, compared to diffusion bonding, due to intensification of the diffusion processes and rapid destruction of oxide film on contact surfaces. However, application of this method is limited by the ability to weld small-sized samples.

ROLL BONDING

In works [29–31] on roll bonding the degree of sample strain was considerably increased from 32 % [29] to 50 % [30, 31], unlike diffusion bonding, where the degree of strain is equal to 2–5 %.

The authors of work [29] studied the influence of process temperature at accumulative rolling of AZ31 alloy. Sheets of 1 mm thickness were used as initial metal, which were stacked into packs of three and heated in the furnace up to 350–450 °C for 10 min. Rolling was performed with 32 % strain and 14 m/min rate.

It was shown that at preheating of sample assembly up to 350 °C, dynamic recrystallization starts taking place at the grain boundary. At 400 °C shear bands start forming, which consisted of dynamically recrystallized grains. At 450 °C a shear band of irreg-

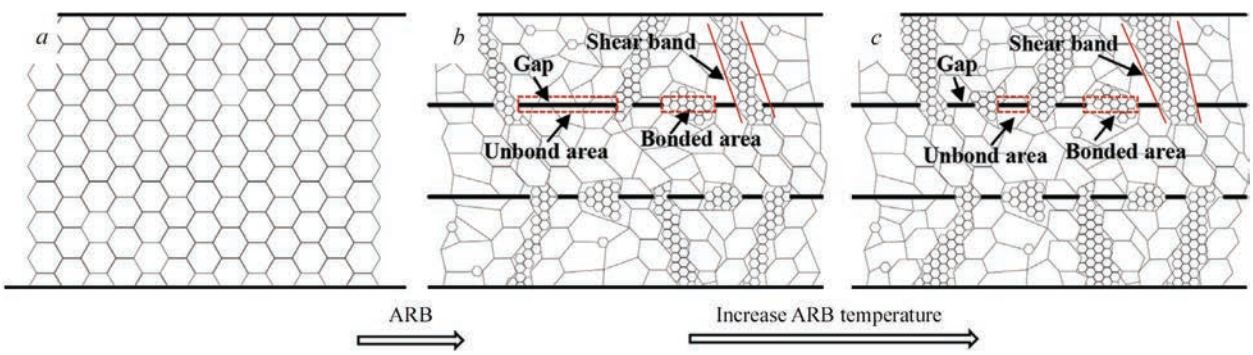

Figure 10. Schematic illustration of evolution of the microstructure and mechanism of formation of AZ31 alloy joint at different process temperature

Parameters of pressure bonding of magnesium alloys

Material	Bonding process	Interlayer	Bonding parameters			Joint strength, MPa	Source
			T, °C	*P*, MPa	*t*, min		
Pure Mg	DW	–	400	20	60	τ = 95.7–109.4	[5]
AZ31	DW	–	400	3	180	τ = 74.2–80.5	[6]
AZ31	DW	–	300	20	60	τ = 68.5	[7]
AZ31	DW	–	400	5	180	τ = 74.5–81.1	[8]
			400	3	120	τ = 81.4–85.1	
AZ31	DW	–	420	8	90	τ = 76.2	[9]
ZK60	DW	–	380	20	90	τ = 65.8	[10]
AZ61	DW	–	470	10	90	τ = 51.95	[11]
AZ91	DW	–	470	10	90	τ = 76.93[1]	[12]
AZ31B	DW	Copper foil	480	10	30	–	[13]
Mg–3Al– 1Zn	DW	Cu foil	370	0.7	30	τ = 70.2	[14]
AZ31	DW	Cu coating + Sn foil	520	0.5	50	τ = 67	[15]
AZ31	DW	Cu coating + TiO_2 nanoparticles	525	1	120	τ = 31.66	[16]
AZ31	DW	Al foil	440	2	75	τ = 35	[17]
AZ91	DW	Ag foil	480	1	30–120	τ = 65–70	[18]
AZ31	DW	Ag foil	500	–	60	τ = 39	[19]
AZ31	DW	Ni	515	0.16	60	τ = 36	[20]
AZ31	DW	Ni coating	520	8	20	τ = 46.2	[21]
AZ-91	DW	SiC particles	420	10	60	τ = 109	[22]
AZ31	DW	–	350	–[3]	3	σ_t = 164.7[1]	[23]
WE43	DW	–	450	–[3]	–	σ_t = 158.60	[24]
ME20M	USW	Zn foil	370	0.15	2	τ = 106.4[2]	[25]
ME20M	USW	Cu–38Zn foil	460	0.15	1.5	τ = 105[2]	[26]
AZ31B	USW	Zn foil	380	0.36	0.02	τ = 42[2]	[27]
AZ31B	USW	Zn foil	360	0.4	–	τ = 40[2]	[28]
AZ31	RB	–	450	–	–	σ_t = 295.4	[29]
LZ91	RB	–	150	–	–	σ_t = 290.2	[30]
AZ31	RB	–	400	–	–	–	[31]

Notes. [1]Strength values after joint heat treatment. [2]Application of ultrasound as an additional source of intensification of joint formation process. [3]Compression in bonding with the specified level of upsetting.

ular shape forms, the width of which decreases from the surface inwards. Increase of sample temperature before rolling intensifies the dynamic recrystallization in the butt joint and improves the joint quality. At a high temperature, grain boundaries shift easily, and the recrystallized grains come into contact and coalesce. The features of joint formation are shown schematically in Figure 10, depending on the preheating temperature. On the whole, the rolling process significantly lowers the material elongation value and almost does not change the yield limit and rupture strength. An essential lowering of ductility is attributable to cracking during rolling. The optimal preheating temperature was 450 °C. At this temperature the yield limit was 222.8 MPa, ultimate strength was 295.4 MPa and elongation was 6.0 %.

In work [30] LZ91 magnesium alloy (Mg–6Li–1Zn) was subjected to accumulative rolling. Plates 100 mm long and 0.65 mm thick were cleaned from one side, stacked into packs of two, heated up to 150 or 400 °C in air and rolled with the degree of strain of 50 % at roll temperature of 135 °C. Then, the thus obtained two-layer sheets were again stacked into a pack of two and the process was repeated up to 5 times.

In the initial state an elongated fibrous structure is found in LZ91 alloy, which consists of two main α and β phases. Pack rolling promotes grain refinement and formation of a more homogeneous structure. At preheating temperature of 400 °C and five rolling cycles the fibrous structure of Mg-rich α-phase becomes thinner and discontinuous. Samples preheated up to 150 °C and rolled five times had the maximum value of ultimate strength of 290.2 MPa. Application of a

higher preheating temperature leads to a certain drop of hardness and strength values, as a result of passage of the process of recovery and recrystallization.

The authors of [31] studied the deformational behaviour at accumulative rolling of AZ31 magnesium alloy (Mg–3.2Al–1.3Zn–0.4Mn–0.06Ce–0.03Fe–0.01 Si, wt.%). Sheets of 2 mm thickness were stacked into packs of two and rolled with the degree of strain of 50 % and rate of 24 mm/min. Preheating temperature was 350–400 °C.

Joints could only be produced at preheating up to 400 °C. After the first pass a line of contact with dispersed particles of the oxide is clearly visible in the butt joint. Al_8Mn_5 phase is rather uniformly distributed in the base metal and joint zone. Cracks form at the edges. After the second pass, the adhesion strength was improved, and no delaminations were observed on the interface. Rolling essentially influences the grain size: already after the first pass, their average size drops by an order of magnitude from 100 to 10 μm, and after the second one — to 7.6 μm, here coarse grains practically disappear. Grain refinement occurs due to rotational dynamic recrystallization. It is emphasized that increase of yield limit and ultimate strength values occurs even after one rolling pass. Certain heterogeneity of the mechanical properties is noted that is related to the texture formed during rolling: they are somewhat higher in the rolling direction, than across it. This anisotropy decreases with increase of the number of passes. While deformation of samples cut out in the rolling direction is mainly performed by dislocation slipping, mechanical twinning has an important role during deformation of samples cut out across the rolling direction.

Results of investigations presented in works [29–31] for roll bonding, lead to the conclusion that increase of plastic deformation rate leads to an essential grain refinement and improvement of joint strength due to running of dynamic recrystallization processes.

Proceeding from the currently available technologies of joining magnesium alloys (Table), we can conclude that there are no well-established technologies at their bonding to produce sound joints. Modes which differ essentially from each other are proposed even for bonding similar alloys. On the whole, it can be summed up that it is desirable to conduct the process as lower bonding temperatures and/or bonding duration, and to allow for the initial metal grain size. Application of eutectic interlayers allows significantly shortening the time of joint formation.

CONCLUSIONS

Pressure bonding processes are extensively applied to produce magnesium alloy welded joints. The main ways to improve the bonding processes are application of the following approaches:

- control of temperature-time parameters of bonding to make grain growth impossible;
- application of interlayers in the form of individual layers of similar materials based on copper, nickel, zinc, aluminium or silver, or eutectic mixtures that allows, due to component interaction, accelerating destruction of the oxide film on the surface of samples being welded;
- butt joint strengthening due to application of nano- or fine particles;
- intensification of plastic deformation due to superposition of ultrasonic oscillations;
- increase of plastic deformation intensity;
- application of heat treatment before and after bonding.

Thus, in diffusion bonding of magnesium alloys the following can be considered promising: application of thin interlayers or coatings that should reduce the chemical heterogeneity in the butt joint and promote activation of the contact surfaces, strengthening of the joint zone due to addition of fine particles to the butt, or their formation during an increase of the rate and degree of plastic strain.

REFERENCES

1. Gialanella, S., Malandruccolo, A. (2020) *Aerospace alloys*. Springer, Cham.
2. Colleen Bettles, Matthew Barnett. (2012) *Advances in wrought magnesium alloys. Fundamentals of processing, properties and applications*. Woodhead Publishing Limited.
3. Min, D., Shen, J., Lai, S., Chen, J. (2009). Effect of heat input on the microstructure and mechanical properties of tungsten inert gas arc butt-welded AZ61 magnesium alloy plates. *Materials Characterization,* 60(**12**), 1583–1590. DOI:10.1016/j.matchar.2009.09.010
4. Abbas, M., Khan, A., Ali, M. et al. (2014) Effect of weld current and weld speed on the microstructure and tensile properties of magnesium alloy specimens during tungsten inert gas. *Technical Journal, University of Engineering and Technology Taxila*, 19(**II**), 35–39.
5. Hidetoshi Somekawa, Hiroyuki Hosokawa, Hiroyuki Watanabe, Kenji Higashi (2001) Experimental Study on Diffusion Bonding in Pure Magnesium. *Materials Transact.*, 42(**10**), 2075–2079. DOI: https://doi.org/10.2320/matertrans.42.2075
6. Hidetoshi Somekawa, Hiroyuki Hosokawa, Hiroyuki Watanabe, Kenji Higashi (2003) Diffusion bonding in superplastic magnesium alloys. *Materi. Sci. and Eng. A,* **339**, 328–333. DOI: https://doi.org/10.1016/S0921-5093(02)00127-2
7. Hidetoshi Somekawa, Hiroyuki Watanabe, Toshiji Mukai, Kenji Higashi (2003) Low temperature diffusion bonding in a superplastic AZ31 magnesium alloy. *Scripta Materialia*, **48**, 1249–1254. DOI: https://doi.org/10.1016/S1359-6462(03)00054-X
8. Hidetoshi Somekawa, Hiroyuki Watanabe, Kenji Higashi (2003) The Grain Size Dependence on Diffusion Bonding Behavior in Superplastic Mg Alloys. *Materials Transact.*, 44(**4**), 496–503. DOI: https://doi.org/10.2320/matertrans.44.496
9. Fei, Lin, Tiepeng, Li, Lulu, Sun, Qingsen, Meng. (2012) A study on vacuum diffusion bonding of as-extruded AZ31 magnesium alloy. *Applied Mechanics and Materials,* **121–126**, 10–14. DOI: https://doi.org/10.4028/www.scientific.net/AMM.121-126.10

10. Yu Yandong, Li Qiang (2005) Diffusion Bonding in Superplastic ZK60 Magnesium Alloy. *Materials Science Forum*, **488–489**, 227–230. DOI: https://doi.org/10.4028/www.scientific.net/MSF.488-489.227
11. Fei, Lin, Jie, Li, Hongwei, Zhao et al. (2013) Experimental research on vacuum diffusion bonding of as-extruded AZ61 magnesium alloy. *Advanced Materials Research*, **788**, 34–37. DOI: https://doi.org/10.4028/www.scientific.net/AMR.788.34
12. Fei Lin, YaXin Tian, ZhiTong Chen et al. (2015) Diffusion bonding and post-weld heat treatment of extruded AZ91 Magnesium Alloys. *Materials Science (Medžiagotyra)*, 21(**4**), 532–535. DOI: https://doi.org/10.5755/j01.ms.21.4.9699
13. Zhang Weixiang, Du Shuangmin (2013) Investigation into Cu-interlayered Diffusion Bonding Trial of AZ31B Alloy. *Advanced Materials Research*, **631–632**, 167–171. DOI: https://doi.org/10.4028/www.scientific.net/AMR.631-632.167
14. Sun, D.Q., Liu, W.H., Gu, X.Y. (2004) Transient liquid phase bonding of magnesium alloy (Mg–3Al–1Zn) using copper interlayer. *Materials Science and Technology*, 20(**12**), 1595–1598. DOI: https://doi.org/10.1179/1743284103X13789824293506
15. Abdulaziz Nasser AlHazaa, Muhammad Ali Shar, Anas Mahmoud Atieh, Hiroshi Nishikawa (2018) Transient liquid phase bonding of magnesium alloy AZ31 using Cu coatings and Cu coatings with Sn interlayers. *Metals*, **8**, 60–69. DOI: https://doi.org/10.1016/j.jksus.2015.09.006
16. Dehnavi, F., Bakhtiari, R. (2021) Effect of microstructure aspects on mechanical properties of nanoparticle-assisted transient liquid phase (NP-TLP) joints for AZ31 alloy. *J. of Manufacturing Processes*, **68**, 42–55. DOI: https://doi.org/10.1016/j.jmapro.2021.05.032
17. Sohrab Ghahri Saremi, Seyyed Ehsan Mirsalehi, Ali Shamsipur (2018) Transient liquid phase bonding of AZ31 magnesium alloy: Metallurgical structure and mechanical properties. *J. of Manufacturing Processes*, **35**, 140–148. DOI: https://doi.org/10.1016/j.jmapro.2018.08.002
18. Torun, O., Karabulut, A., Baksan, B., Çelikyürek, I. (2008) Diffusion bonding of AZ91 using a silver interlayer. *Materials and Design*, **29**, 2043–2046. DOI: https://doi.org/10.1016/j.matdes.2008.04.003
19. Reza Ghavami, Ayoub Halvaee, Amir Hadian (2019) Effect of bonding temperature on interface properties of AZ31 magnesium alloys joined by transient liquid phase using silver interlayer. *Materials Research Express*, **6**, 116519, 1–9. DOI: https://doi.org/10.1088/2053-1591/ab44df
20. Jin, Y.J., Khan, T.I. (2012) Effect of bonding time on microstructure and mechanical properties of transient liquid phase bonded magnesium AZ31 alloy. *Materials and Design*, **38**, 32–37. DOI: https://doi.org/10.1016/j.matdes.2012.01.039
21. AlHazaa A.N., Khalil Abdelrazek Khalil, Muhammad A. Shar (2016) Transient liquid phase bonding of magnesium alloys AZ31 using nickel coatings and high frequency induction heat sintering. *J. of King Saud University — Science*, **28**, 152–159. DOI: https://doi.org/10.1016/j.jksus.2015.09.006
22. Ramanujam, N., Rajamuthamilselvan, M., Girish, G. (2016) Investigation on mechanical properties of diffusion bonded AZ-91 magnesium alloy reinforced with Sic particles. *Inter. J. of Engineering Research & Technology (IJERT)*, 12(**5**), 159–166.
23. Ren, L., Li, B., Chen, Z. et al. (2021) Interfacial microstructure analysis of AZ31 magnesium alloy during plastic deformation bonding. *Processes*, **9**, 1857–1867. DOI: https://doi.org/10.3390/pr9101857
24. Lingxiao Ouyang, Yunwei Gui, Quanan Li, Yunqiang Fan (2021) Isothermal compression bonding mechanism and mechanical properties of WE43 magnesium-rare earth alloy. *Materials Science & Engineering A*, **822**, 141664, 1–12. DOI: https://doi.org/10.1016/j.msea.2021.141664
25. Lai Zhiwei, Chen Xiaoguang, Pan Chuan et al. (2016) Joining Mg alloys with Zn interlayer by novel ultrasonic assisted transient liquid phase bonding method in air. *Materials Letters*, **166**, 219–222. DOI: https://doi.org/10.1016/j.matlet.2015.11.031
26. Zhiwei Lai, Ruishan Xie, Chuan Pan et al. (2017) Ultrasound-assisted transient liquid phase bonding of magnesium alloy using brass interlayer in air. *J. of Materials Science & Technology*, 33(**6**), 567–572. DOI: https://doi.org/10.1016/j.jmst.2016.11.002
27. Zhiwu, Xu, Zhengwei, Li, Liming, Peng, Jiuchun, Yan (2019) Ultra-rapid transient liquid phase bonding of Mg alloys within 1 s in air by ultrasonic assistance. *Materials and Design*, **161**, 72–79. DOI: https://doi.org/10.1016/j.matdes.2018.11.015
28. Zhiwu Xu, Shu Chen, Liming Peng et al. (2020) Microstructure evolution and mechanical properties of ultrasonically TLP bonded Mg joint. *J. of Manufacturing Processes*, **52**, 145–151. DOI: https://doi.org/10.1016/j.jmapro.2020.01.056
29. Xixin Rao, Yunpeng Wu, Xiaobing Pei et al. (2019) Influence of rolling temperature on microstructural evolution and mechanical behavior of AZ31 alloy with accumulative roll bonding. *Materials Science & Engineering A*, **754**, 112–120. DOI: https://doi.org/10.1016/j.msea.2019.03.047
30. Akhmad Saufan, Ing-Song Yu, Jian-Yih Wang (2020) Enhancement of mechanical properties for Mg–9Li–1Zn alloy by accumulative roll bonding. *Materials Research Express*, **7**, 046511, 1–8. DOI: https://doi.org/10.1088/2053-1591/ab86f8
31. Zuzanka Trojanová, Ján Džugan, Kristýna Halmešová et al. (2018) Influence of accumulative roll bonding on the texture and tensile properties of an AZ31 magnesium alloy sheets. *Materials*, 73(**11**), 1–14. DOI: https://doi.org/10.3390/ma11010073

ORCID
Yu.V. Falchenko: 0000-0002-3028-2964,
L.V. Petrushynets: 0000-0001-7946-3056

CONFLICT OF INTEREST
The Authors declare no conflict of interest

CORRESPONDING AUTHOR
Yu.V. Falchenko
E.O. Paton Electric Welding Institute of the NASU
11 Kazymyr Malevych Str., 03150, Kyiv, Ukraine.
E-mail: falchenko@paton.kiev.ua

SUGGESTED CITATION
Yu.V. Falchenko, L.V. Petrushynets (2022) Modern technological methods of pressure welding of magnesium alloys (Review). *The Paton Welding J.*, **6**, 29–40.

JOURNAL HOME PAGE
https://pwj.com.ua/en

Received: 18.04.2022
Accepted: 15.08.2022

https://doi.org/10.37434/tpwj2022.06.06

EFFECT OF DEFORMATION OF MOLTEN METAL DROPLETS ON THEIR MOTION AND HEATING IN LIQUID SLAG

I. Krivtsun[1], V. Sydorets[1], G. Stovpchenko[1], G. Polishko[1], A. Sybir[2], L. Medovar[1]

[1]E.O. Paton Electric Welding Institute of the NASU
11 Kazymyr Malevych Str., 03150, Kyiv, Ukraine
[2]National Metallurgical Academy of Ukraine
4 Gagarin Prosp., 49600, Dnipro, Ukraine

ABSTRACT

The mathematical models describing motion and heating of molten metal droplets in a liquid slag layer at the process of traditional electroslag remelting have been developed, assuming that the droplets have a spherical shape or deform to a spheroids flattened in their movement direction. The deformation of metal droplets impacts the velocity of their motion, making more efficient their heating while falling through the molten slag layer because of the bigger midsection and surfase areas of the deformed droplets at the same volume and mass. The differences between the predicted characteristics of motion and heat up of spherical and deforming droplets in the slag layer are more significant for the droplets of large size.

KEYWORDS: electroslag remelting; mathematical modeling; consumable electrode; droplets; motion; deformation; heating

INTRODUCTION

Both the metal and slag droplets usually arise at pyrometallurgical processes, including various refining and welding methods. Droplets quantity and their size define the intensity and completeness of heat and mass transfer in these processes. The knowledge on behaviour of droplets allows optimize the conditions of chemical interactions and heat exchange between phases involved (gas, metal and slag). The behaviour of molten metal droplets at their motion in a liquid slag and vice versa at metal refining is the most often subject of investigation [1–6].

The drag coefficient is the crucial parameter for analysis of the dynamics of liquid metal particles in motion through different media. This coefficient is determined by the Stokes formula (usually for the movement of spherical particles at small Reynolds numbers) or by more complex criterion dependences considering the change in flow nature at particle size and velocity growing [7–9]. In the most cases, a moving droplet is assumed as a solid-state sphere of perfect regular shape. However, the motion of a liquid particle (like a molten metal droplet falling in a slag layer at the electroslag remelting process) has distinctive differences, namely, the change of its shape at motion and, accordingly, the drag force acting on it. The movement of deformable droplets can be modeled using numerical methods [10] allowing to estimate the velocity fields both outside and inside a droplet. However, this approach is quite complicated.

Evaluation of the size of droplets formed in the conditions of the electroslag remelting (ESR) processes on a consumable electrode is considered in many works [11–15]. Usually, the characteristics of a droplet motion in the slag layer is made using the criterion dependences of the drag coefficient for the spherical shape droplet (with no deformation).

In this work the simplified mathematical models allowing numerical evaluation of motion and heating of the molten metal droplets detached from the end of a consumable electrode under the conditions of ESR processes have been developed, taking into account possible changes in the droplet shape while falling in

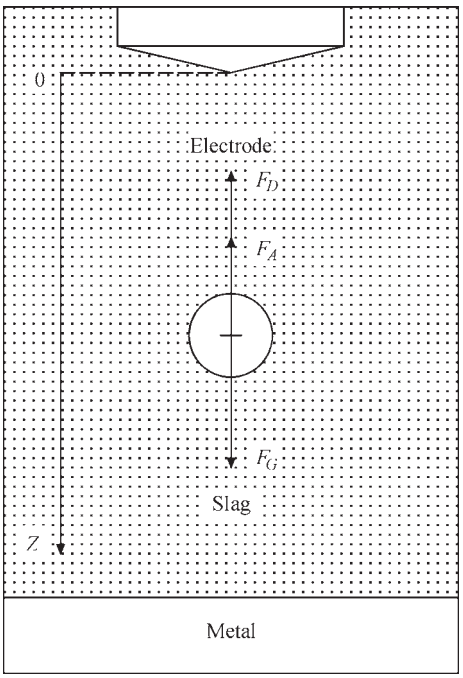

Figure 1. Scheme of forces acts on a molten metal droplet moving in a liquid slag layer at ESR: D_0 is the initial droplet diameter; F_G is the gravity force; F_A is the Archimedes force; F_D is the drag force

a liquid slag layer. Figure 1 shows the scheme of the above mentioned process.

The main parameters of liquid slag and metal droplets used in simulation the following:

- slag (ANF-29): density (ρ_s) — 2780 kg/m^3; specific heat capacity (C_s) — 1200 J/(kg·K); coefficient of dynamic viscosity (η_s) — 0.01965 Pa·s; coefficient of thermal conductivity (χ_s) — 6 W/(m·K); slag temperature (T_s) — 2073 K;
- metal (Steel 45): density (ρ_m) — 7000 kg/m^3; specific heat capacity (C_m) — 600 J/(kg·K); coefficient of dynamic viscosity (η_m) — 0.003 Pa·s; coefficient of thermal conductivity (χ_m) — 35 W/(m·K); coefficient of surface tension (σ_m) — 1.1 N/m; initial temperature of the droplet (T_m) — 1823 K.

MODELLING OF METAL DROPLETS MOTION IN LIQUID SLAG

The droplets detached from the consumable electrode surface move in a liquid slag layer under the gravity force and also are affected by Archimedes and hydrodynamic drag forces (Figure 1). The equation of the movement of a droplet can be written as:

$$\rho_m V \frac{du}{dt} = V(\rho_m - \rho_s)g - C_D S \frac{\rho_s u^2}{2};\ t \geq 0, \qquad (1)$$

where V is the droplet volume; $u=dz/dt$ is its velocity; t is the time counted from the moment of the droplet detachment; g is the acceleration of gravity; C_D is the drag coefficient, which depends on the Reynolds number; S is the midsection area of the droplet. At the initial moment ($t = 0$), we will assume that the droplet is spherical and has a diameter D_0 (radius r_0) and zero velocity ($u = 0$).

To estimate the effect of molten metal droplet deformation on its motion in a liquid slag, we consider two cases: the droplet remains spherical form in the process of its movement; the droplet changes its shape (deforms), preserving the same volume as the original spherical droplet.

In the first case, concerning that $V = \frac{4}{3}\pi r_0^3$; $S = \pi r_0^2$, the equation (1) can be rewritten as:

$$\frac{du}{dt} = \frac{\rho_m - \rho_s}{\rho_m} g - C_D \frac{\rho_s}{\rho_m} \frac{3u^2}{4D_0} \qquad (2)$$

with the initial condition

$$u|_{t=0} = 0. \qquad (3)$$

The drag coefficient of a spherical droplet can be expressed by the following criteria dependences [4]:

$$C_{D,\,sphere} = \begin{cases} \frac{24}{\mathrm{Re}}, & \mathrm{Re}<0{,}2; \\ \frac{24}{\mathrm{Re}} + 3.6\,\mathrm{Re}^{-0.317}, & 0.2<\mathrm{Re}<4; \\ \frac{24}{\mathrm{Re}} + 4\,\mathrm{Re}^{-0.333}, & 4<\mathrm{Re}<400; \\ \frac{24}{\mathrm{Re}} + 5.48\,\mathrm{Re}^{-0.573} + 0.36, & 400<\mathrm{Re}<10^4, \end{cases} \qquad (4)$$

Here $\mathrm{Re}\frac{\rho_s u D_0}{\eta_s}$ is the Reynolds number for a droplet moving in a liquid slag.

When performing the numerical calculation, the initial diameter of the droplet D_0 was varied in the range of 2–10 mm. The depth of the slag pool L (distance from the end of the electrode to the metal surface) was constant and equal to 200 mm. All calculations were performed in the following ranges of variables: $0 < t < 1.5$ s; $0 < z < 1000$ mm. The calculated velocity of spherical droplets of small ($D_0 = 2$ mm) and large ($D_0 = 10$ mm) diameter are shown in Figure 2.

These plots show that a spherical droplet of 2 mm reaches its constant (maximum) velocity 0.153 m/s in 0.1 s of its falling (Figure 2, *a*, curve *1*) at a distance from the electrode of about 12 mm (Figure 2, *b*, curve *1*), which is much less than the selected depth of the liquid slag layer. The droplet of 10 mm in diameter moves much faster than the previous one. It reaches its constant speed of 0.641 m/s after 0.3 s (Figure 2, *a*, curve *2*) at a distance from the electrode

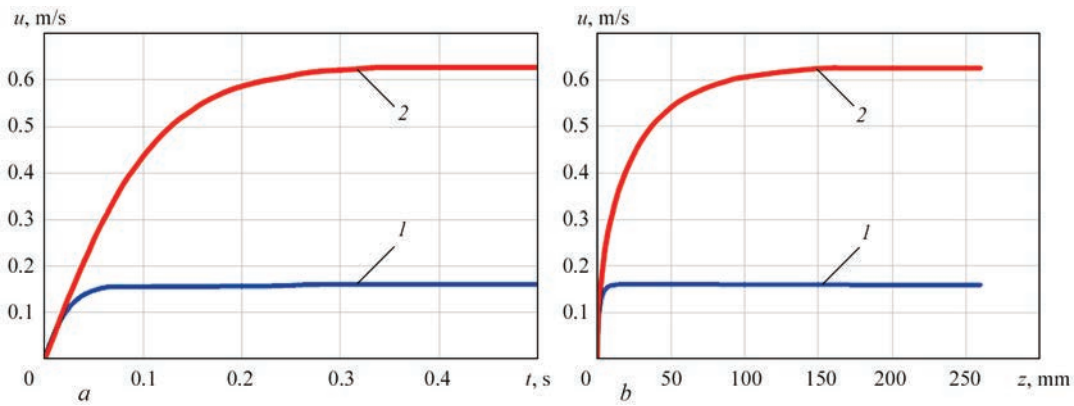

Figure 2. Dependence of velocity of spherical droplets with an initial diameter of 2 mm (*1*) and 10 mm (*2*), on time (*a*) and distance travelled (*b*)

of about 150 mm (Figure 2, *b*, curve *2*), commensurate with the usual depth of a slag pool in commercial ESR processes.

In the case, when a droplet of liquid metal deforms during motion in a slag layer, its shape can be represented as a linear superposition of eigenmodes of natural oscillations of its surface. Under the condition of axially symmetric deformation, it can be presented as:

$$\frac{r_s(\vartheta,t)}{R_0}=1+\sum_{n=2}^{\infty}a_n(t)P_n(\cos\vartheta), \qquad (5)$$

where $r = r_s(\vartheta, t)$ is the equation of a droplet surface in the polar coordinates r, φ, $\vartheta\}$; $P_n(\cos\vartheta)$ is the Legendre polynomials. The equations for determining the dependences of the coefficients of the decomposition (5) on time have the following form [16]:

$$\frac{d^2a_n}{d\bar{t}^2}+8(n-1)(2n+1)\frac{1}{\mathrm{Re}_{def}}\frac{da_n}{d\bar{t}}+ \\ +8n(n-1)(n+2)\frac{1}{We}a_n=-2nC_n;\ n\ge 2. \qquad (6)$$

Here $\bar{t}=\frac{t}{t^*}$ is the dimensionless time, where $t^*=\sqrt{\frac{\rho_m}{\rho_s}}\frac{D_0}{u}$; $\mathrm{Re}_{def}=\frac{uD_0}{\eta_m}\sqrt{\rho_m\rho_s}$ is the Reynolds number for metal flow inside the droplet; $\mathrm{We}=\frac{\rho_s u^2 D_0}{\sigma_m}$ is the Weber number; C_n are the coefficients of decomposition of the pressure distribution $p_s(\vartheta)$ over the droplet surface

$$\frac{p_s(\vartheta)-p_\infty}{(\rho_s/2)u^2}=\sum_{n=2}^{\infty}C_nP_n(\cos\vartheta). \qquad (7)$$

The experimental dependences of the coefficients C_n in the decomposition (7) on the Reynolds number for the most significant eigenmodes of droplet surface oscillations (n = 2–5) are shown by Schmehl in [16]. As the result the following dependencies for turbulent, non-stationary, asymmetric stationary and laminar flows were obtained: $C_2 = 0.45 + 0.55\exp(-0.15\,\mathrm{Re}^{0.36})$; $C_3 = 0.45 - 0.45\exp(-5.2\cdot10^{-2}\,\mathrm{Re}^{0.63})$; $C_4 = 0.17 - 0.17\exp(-3.9\cdot10^{-5}\,\mathrm{Re}^{1.45})$; $C_5 = -0.07 + 0.07\exp(-5.6\cdot10^{-5}\,\mathrm{Re}^{1.93})$.

The most significant mode (n = 2) of droplet surface oscillations gives enough accurate evaluation of the impact of their deformation on motion speed in liquid slag. So we can assume that the molten metal droplet, having initial spherical shape, deforms and acquires a form of a flattened (in motion direction) spheroid. The spheroid is a rotation body formed by the ellipse (with $a > c$ semi-axes) revolving around the minor axis as shown in Figure 3.

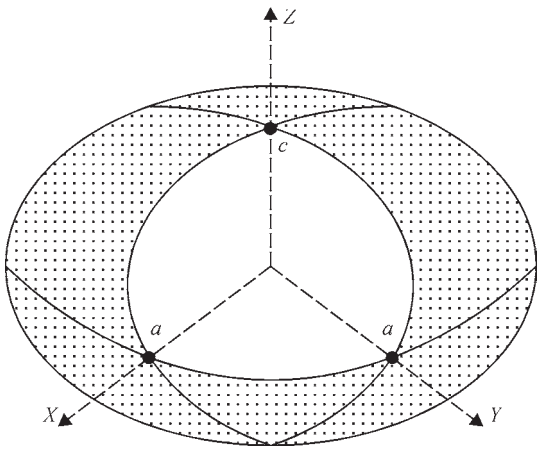

Figure 3. The appearance of a flattened spheroid

The equation of motion (1) sustains the same because the droplet's volume (mass) is constant. The area of the midsection and the drag coefficient of deformed droplets change.

The coefficient characterises a nonsphericality of the deformed droplet shape can be expressed as

$$y=\frac{D}{D_0}=\frac{a}{r_0}\ge 1, \qquad (8)$$

where D is the bigger diameter of the spheroid. Using this coefficient the equation (1) can be rewritten as

$$\frac{du}{dt}=\frac{\rho_m-\rho_s}{\rho_m}g-\bar{C}_D\frac{\rho_s}{\rho_m}\frac{3u^2y^2}{4D_0}, \qquad (9)$$

with the initial condition (3). From the condition of volume preserving for droplets at deformation from the initial spherical shape to a flattened spheroid, it follows that $a = r_0 y$, $c=\frac{r_0}{y^2}$ and the surface area of the deformed droplet is determined as follows:

$$S_s=2\pi a\left(a+\frac{c^2}{\sqrt{a^2-c^2}}\ln\frac{a+\sqrt{a^2-c^2}}{c}\right). \qquad (10)$$

This area will be further compared with the surface area of the original spherical droplet $S_{s_0}=4\pi r_0^2$ using the ratio $S=\frac{S_s}{S_{s_0}}$.

To calculate the drag coefficient of the deformed droplet included in equation (9), we will use the following dependence [16]:

$$\bar{C}_D=(1-f)C_{D,\,sphere}+fC_{D,\,disc}. \qquad (11)$$

Here $f = 1 - E^2$, where $E=\frac{c}{a}=\frac{1}{y^3}$ is the ratio of a small semi-axis of a flattened spheroid to the large one

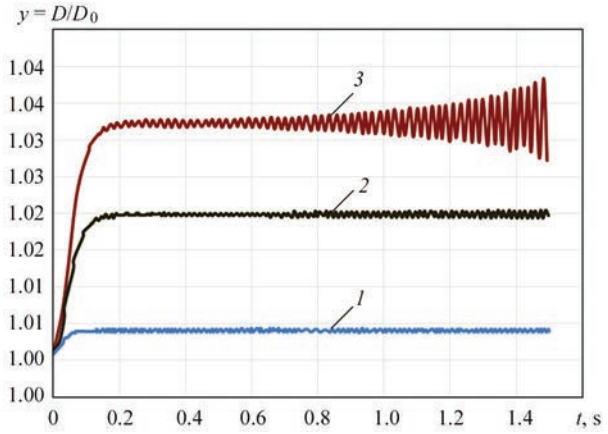

Figure 4. Dependences of the nonsphericality coefficient for the molten metal droplets on time at small values of their initial diameter: *1* — D_0 = 2; *2* — 4 (F = 62.5 Hz); *3* — 5 mm (F = 45.0 Hz)

(in the limiting cases we have: for the sphere E = 1, for an infinitely thin disk E = 0). The value $C_{D,\ sphere}$ is calculated by the formulas (4) at $\mathrm{Re}=\overline{\mathrm{Re}}$, where $\overline{\mathrm{Re}}=\dfrac{\rho_s u D_0 y}{\eta_s}$ is the Reynolds number that is calculated taking into account the change in a diameter of the midsection of a droplet, and the drag coefficient of the thin disk, which is calculated by the formula [16]:

$$C_{D,disc}=1.1+\frac{64}{\pi\overline{\mathrm{Re}}}. \qquad (12)$$

To determine the $y(t)$ value, the first equation (6) (at n = 2) can be written in the form [16]:

$$\frac{d^2y}{d\overline{t}^2}+\frac{40}{\mathrm{Re}_{def}}\frac{dy}{d\overline{t}}+\frac{64}{\mathrm{We}}(y-1)= \\ =0.9+1.1\exp\left[-0.15\overline{\mathrm{Re}}^{0.36}\right] \qquad (13)$$

with the initial conditions

$$y|_{\overline{t}=0}=1; \qquad \left.\frac{dy}{d\overline{t}}\right|_{\overline{t}=0}=0. \qquad (14)$$

The results of modelling behaviour of the molten metal droplets having different initial diameters with considering their deformation at movement in the slag layer are presented in Figures 4–7.

As follows from the calculated data shown in Figure 4, droplets of a size up to 4 mm almost preserves the initial spherical shape during their motion in the liquid slag layer. They experience weak oscillations of the shape with a frequency F that reduces with D_0 increase (4 mm F = 62.5 Hz; 5 mm F = 45 Hz). A droplet with an initial diameter of 5 mm undergoes deformation in the oscillating mode with a growing amplitude. The average value of the degree of deformation $\delta=\dfrac{D-D_0}{D_0}$ of such a droplet amounts about 3 % (Figure 4, curve *3*).

As shown in Figure 6, for larger droplets (D_0 = = 6–10 mm) the degree of deformation grows with an increase in D_0 at a corresponding rise in the amplitude of oscillations of the droplet surface, and these oscillations themselves become aperiodic starting from a certain moment of time (or after passing the appropriate distance in a liquid slag), what can lead to the disintegration of the droplet into smaller fragments. For example, the Weber number for the droplets with the initial diameter of 10 mm, reaches values close to critical (We > 5) already at t = 0.2 s. Dependences of the nonsphericality coefficient for the molten metal droplets on time at small values of their initial diameter are shown in Figure 5, *a*.

The calculation data shown in Figure *6*, a, illustrate the degree of maximum deformation of molten metal droplets of various initial diameters during their motion in a liquid slag for the time moment of 1.2 s.

The significant deformation of a large droplet (D_0 = = 8–10 mm) increases their surface area in compare of the initial spherical droplet, as shown in Figure 6, *b*. This can significantly intensify their heat exchange and chemical interaction with a liquid slag.

The effect of deformation of metal droplets of different initial diameters on the velocity of their motion in a liquid slag is illustrated in Figure 7.

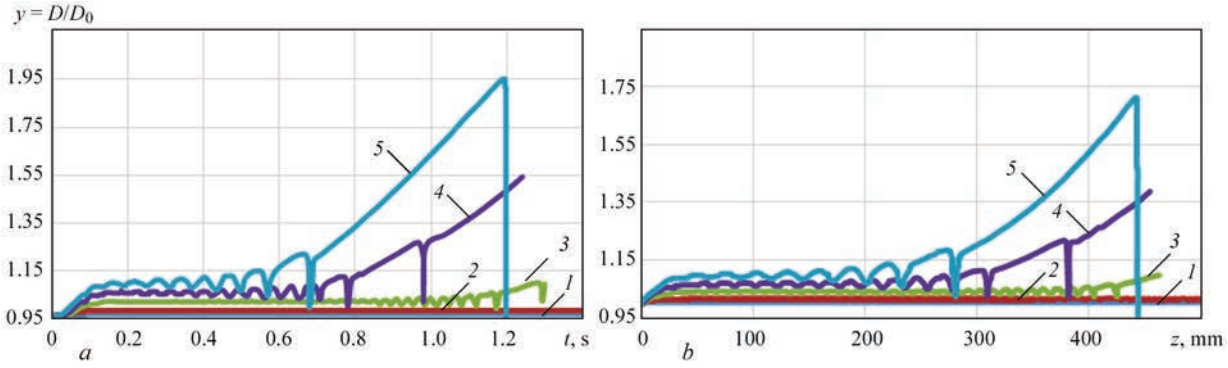

Figure 5. Dependences of the nonsphericality coefficient of molten metal droplets on time (*a*) and distance travelled (*b*) at different initial diameters: *1* — D_0 = 2; *2* — 4; *3* — 6; *4* — 8; *5* — 10 mm

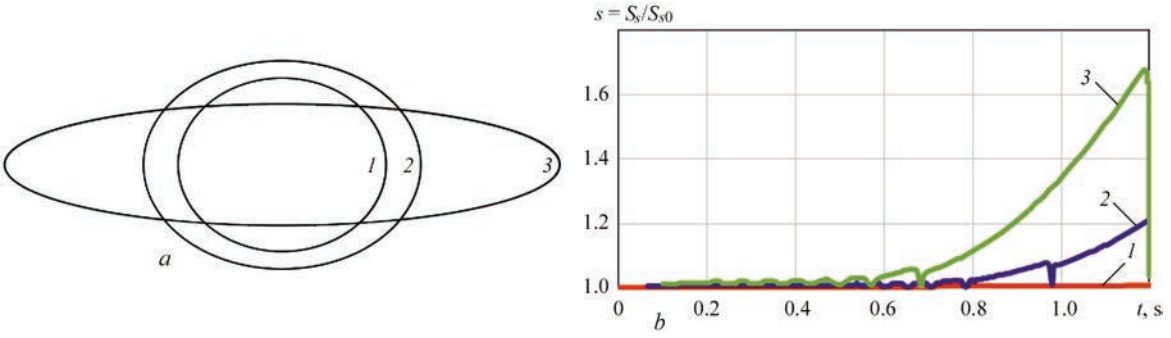

Figure 6. The shape of droplets at 1.2 s from the beginning of their motion and dependence of surface area of deformed metal droplets on time at various values of initial droplet diameter: *1* — D_0 = 6; *2* — 8; *3* — 10 mm

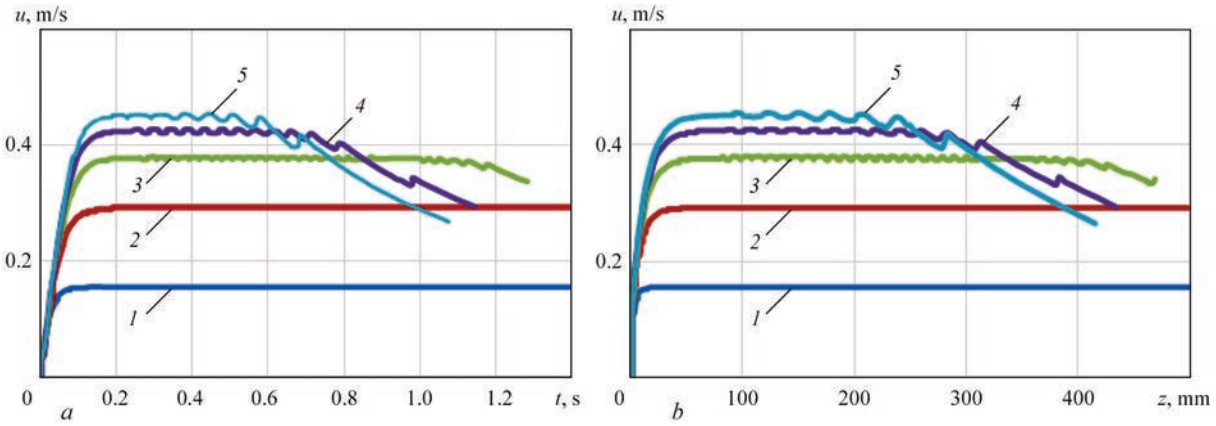

Figure 7. Dependences of velocity of deformed metal droplets on time (*a*) and passed distance (*b*) at various values of initial droplet diameter: *1* — D_0 = 2; *2* — 4; *3* — 6; *4* — 8; *5* — 10 mm

The calculated dependences prove that the small droplets (diameter of 2–4 mm) do not deform sufficiently while their motion (Figures 4, 5). For example, droplets with initial diameter 2 mm reach a constant speed of 0.153 m/s in 0.1 s (at a distance about 12 mm from the electrode), which is similar with the correspondent spherical shape droplets (Figure 2, *a*, *b*, curves *1*). As for the droplets of a larger initial diameter (D_0 = 6–10 mm), they move more slowly than the corresponding spherical droplets because they are subjected to significant deformation at their motion (Figures 5, 6). For example, deformed droplets of 10 mm in diameter reach a speed of 0.450 m/s at a distance of about 100 mm from the surface of the slag pool for 0.2 s, which is significantly lower than the corresponding values for the same size spherical droplets (Figure 2, *a*, *b*, curves *2*). Taking into account that the large droplets deformation occurs in an oscillating mode with an increasing amplitude (Figure 5), their speed decreases (Figure 7) due to changes in the drag force acting on them.

Analysing the results of simulation of molten metal droplets movement in the slag layer at ESR, it should be noted that at the selected depth of the slag pool (L = 200 mm), the noted features of the motion of droplets associated with their deformation became sufficient for large droplets with an initial diameter of more than 8 mm (Figures 5, *b*, 7, *b*).

MODELLING OF METAL DROPLETS HEATING

Assuming that the temperature of the metal in the volume of a droplet has an uniform distribution, the equation that describes heating of a metal droplet during its motion in a liquid slag can be written as:

$$\rho_m V C_m \frac{dT_m}{dt} = S_s \alpha (T_s - T_m);\ t \geq 0, \qquad (15)$$

where T_m is the metal temperature; α is the coefficient of convective-conductive heat exchange, and other designations correspond to those accepted earlier.

If a droplet in the process of its motion preserves a spherical shape, then the equation (15) can be written as:

$$\frac{dT_m}{dt} = \frac{6\alpha}{\rho_m C_m D_0}(T_s - T_m) \qquad (16)$$

with the initial condition

$$T_m\big|_{t=0} = T_0, \qquad (17)$$

To determine the heat exchanger coefficient α, the Nusselt criterion $\mathrm{Nu} = \frac{\alpha D_0}{\chi_s}$ was used. In the case of

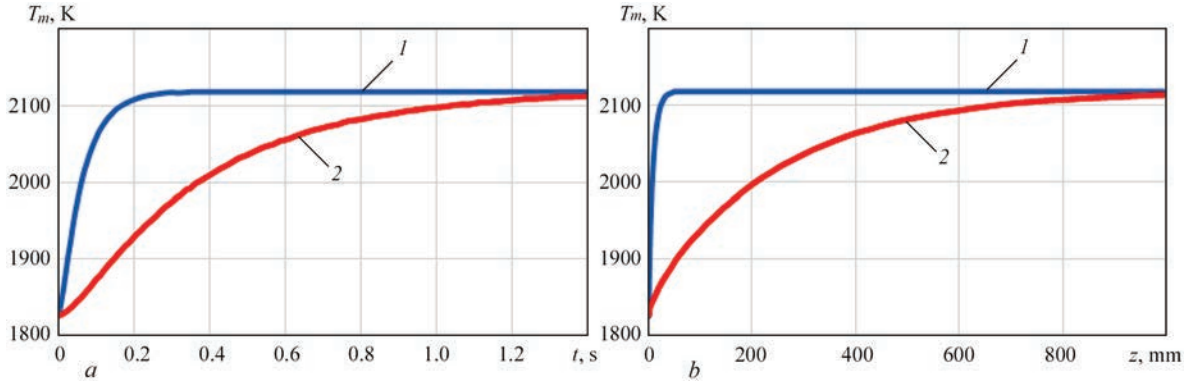

Figure 8. Dependence of temperature of spherical droplets with an initial diameter of 2 mm (*1*) and 10 mm (*2*), on time (*a*) and distance travelled (*b*)

a spherical shape of the droplet, the criterion dependence have the form [4]:

$$\mathrm{Nu} = 2.0 + 0.6\mathrm{Re}^{0.5}\mathrm{Pr}^{0.333}. \quad (18)$$

Here $\mathrm{Pr} = \frac{C_s \eta_s}{\chi_s}$ is the Prandtl number. The Reynolds number was determined considering the change in the droplet velocity depending on the time according to the accepted model of its motion.

The results of simulation of heating of undeformed (spherical) metal droplets of various initial diameters falling in a liquid slag, shown in Figure 8, demonstrate that small droplets are heating up from the initial temperature (1823 K) to the slag temperature (2073 K) much faster than large droplets. For example, a droplet with a diameter of 2 mm reaches the temperature of the slag after 0.25 s (Figure 8, *a*, curve *1*) at a distance of about 40 mm (Figure 8, *b*, curve *1*) from the electrode tip, which is significantly lower than the selected depth of the slag pool.

A droplet with a diameter of 10 mm is heating up much more slowly, and therefore, while passing the entire depth of the slag pool (L = 200 mm), its temperature does not exceed 1980 K (Figure 8, *a*, *b*, curves *2*).

Let us consider now the peculiarities of heating metal droplets during their motion in a liquid slag taking into account their deformation. As previously, we will approximately assume that a droplet in the movement process acquires the shape of a flattened spheroid. Homogeneous heating of a liquid metal droplet deformed in such a way is described by a differential equation

$$\frac{dT_m}{dt} = \frac{3\bar{\alpha} y^2}{\rho_m C_m D_0} \times \left[1 + \frac{1}{y^3\sqrt{y^6 - 1}} \ln\left(y^3 + \sqrt{y^6 - 1}\right)\right](T_s - T_m) \quad (19)$$

with the initial condition (17). Here $y = \frac{D}{D_0}$ is the coefficient of a nonsphericality of droplet; $\bar{\alpha}$ is the heat exchange coefficient for a spheroid, in the determination of which the criterion dependence (18) was used, taking into account that the Nusselt number $\overline{\mathrm{Nu}} = \frac{\bar{\alpha} D_0 y}{\chi_s}$ and the Reynolds number $\overline{\mathrm{Re}} = \frac{\rho_s u D_0 y}{\eta_s}$ were calculated for the midsection diameter of a deformed droplet.

The calculated temperatures for the deformed droplets having various initial diameters on the time and distance travelled in the slag are shown in Figure 11.

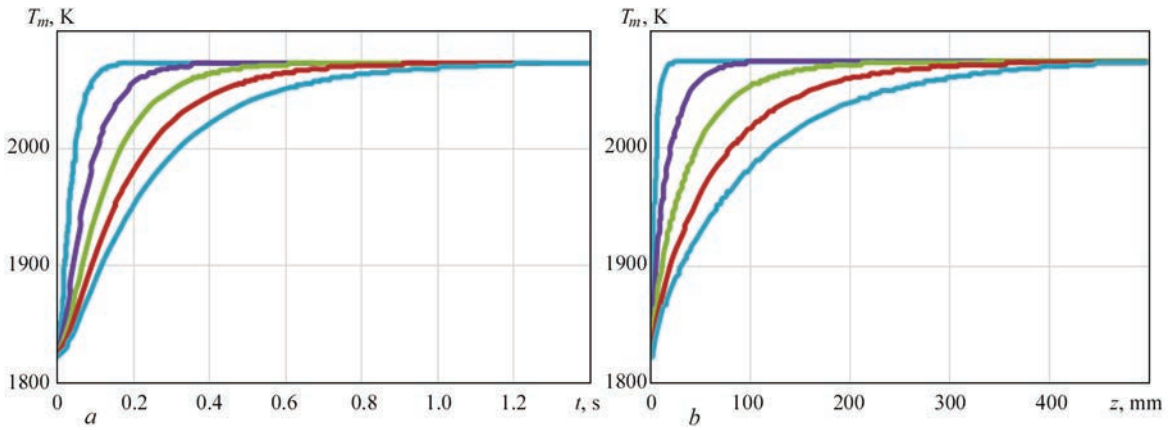

Figure 9. Dependences of temperature of deformed metal droplets on time (*a*) and distance traveled (*b*) at various values of initial droplet diameter: *1* — D_0 = 2; *2* — 4; *3* — 6; *4* — 8; *5* — 10 mm

Table 1. Results of numerical simulation of the processes of motion and heating of molten metal droplets in a liquid slag

D_0, mm	Motion								Heating					
	u_{max}, m/sec		z, mm at $u = u_{max}$		t, s at $u = u_{max}$		t, s at z = 200 mm		z, mm at $T_m = T_s$		t, s at $T_m = T_s$		T_m, K at z = 200 mm	
	SD*	DD**	SD	DD	SD	DD	SD	DD	SD	DD	SD	DD	SD	DD
2	0.153	0.153	12	12	0.10	0.10	1.33	1.33	40	40	0.30	0.20	2073	2073
4	–	0.289	–	30	–	0.15	–	0.74	–	90	–	0.38	–	2073
6	–	0.375	–	60	–	0.16	–	0.58	–	220	–	0.60	–	2070
8	–	0.420	–	80	–	0.18	–	0.53	–	370	–	0.93	–	2050
10	0.641	0.450	150	100	0.30	0.20	0.40	0.51	1000	450	1.60	1.20	1980	2010

*SD — spherical droplet. **DD — deformable droplet.

As follows from the data in Figures 8, *a*, *b*, and 9, an unsignificant deformation of small droplets at motion in the liquid slag (Figure 4) does not significantly change their heating compared to those for spherical droplets. For the convenience of readers, Table 1 shows generalised data on the obtained calculation results.

Deformation of large droplets makes an increasingly significant effect on their heating in liquid slag. For example, a deformed droplet of 10 mm in diameter heats to a slag temperature for a time of about 1.3 s (a distance about 500 mm from the electrode tip). Whereas for a spherical droplet (the deformation is not taken into account), the mentioned conditions ($T_m = T_s$) are met at $t \geq 1.6$ s, $z \geq 1000$ mm (Figure 8, a, b, curves 2). This allows concluding the intensification of heat exchange between liquid slag and metal droplets due to their shape changing.

The results of a numerical study of the moving and heating processes of metal droplets of various initial diameter in a liquid slag with and without taking into account their deformation is valuable for better understanding the heat and mass transfer pricesses in ESR.

CONCLUSIONS

1. Mathematical modeling and numerical simulation of the processes of moving and heating of molten metal droplets in a liquid slag at ESR were completed. Two cases of droplet's behaviour have been considered: when it preserves the initial spherical shape while falling in the slag; when it deforms taking the form of a flattened (in the direction of motion) spheroid. The deformation of droplets affects velocity (duration) of their motion in the slag layer because it increases the drag force acting on a droplet, as well as intensifies their heating and metallurgical interaction with a molten slag because it increases the surface area of a droplet (while maintaining its volume).

2. The deformation of droplets of small diameter (up to 5 mm) occurs by harmonic oscillations of their surface at the frequency range of 50–100 Hz. This frequency increases at a droplet diameter decreasing. The tiny droplets deformation is low (up to 3 %) and almost does not affect on their motion and heating in a liquid slag compared to the corresponding spherical shape droplets.

3. Droplets of large diameter (6–10 mm) undergo a significant deformation, which degree is the bigger, the greater a droplet diameter. The oscillations of its surface become aperiodic with growing amplitude (for a droplet with a diameter of 10 mm, the degree of deformation can reach 75%), which can eventually lead to decomposition of such droplets into smaller ones. Deformed droplets with an initial diameter of 10 mm reach a maximum velocity of 0.45 m/s (for 0.2 s at a distance of 100 mm from the electrode), much lower than the limiting speed of a corresponding spherical droplet (0.64 m/s), and then their velocity decreases.

4. Due to the surface area growing and velocity reduction for droplets of a larger diameter, their heating in the slag layer becames more efficient than for the corresponding spherical droplets. For example, the spherical droplet of 10 mm in diameter reaches the slag temperature of about 1.6 s at a distance of more than 1000 mm from the electrode. In contrast, for deformed droplets, this occurs in 1.2 s at the distance of 450 mm. At the given slag pool depth equals 200 mm, a deformable droplet of 10 mm in diameter is heated only to a temperature of 2010 K, which is more than 60 K lower than the slag temperature.

REFERENCES

1. Medovar, B.I., Tsykulenko, A.K., Shevtsov, V.L. (1986) *Metallurgy of electroslag process*. Kyiv, Naukova Dumka [in Russian].
2. Gulyaev, I.P., Dolmatov, A.V., Kharlamov, M.Yu. et al. (2015) Arc-plasma wire spraying: An optical study of process phenomenology. *J. of Thermal Spray Technology*, 24(**4**), 659–670.
3. Chaulet, J., Kharicha, A., Charmond, S. et al. (2020) A 2D multiphase model of drop behavior during electroslag remelting. *Metals*, **10**, 490. DOI: https://doi.org/10.3390/met10040490
4. Clift, R., Grace, J.R., Weber, M.E. (1978) *Bubbles, drops and particles*. New-York, London, Academic Press.
5. Michaelides, E.E. (2006) *Particles, bubbles & drops*: Their motion, heat and mass transfer. World Scientific Publ.

6. Medovar, L.B., Stovpchenko, G.P., Sybir, A.V. (2020) Comparison of conditions of mass exchange in electroslag processes with consumable electrode and liquid metal. *Uspekhi Fiziki Metallov*, **4**, 481–500 [in Russian]. DOI: https://doi.org/10.15407/ufm.21.01.001
7. Happel, J., Brenner G., (1976) *Hydrodynamics under small Reynolds numbers*. Moscow, Mir [in Russian].
8. Brooks, G., Subagyo, Y. Pan (2005) Modeling of trajectory and residence time of metal droplets in slag–metal–gas emulsions in oxygen steel making. *Metall. and Material Transact. B,* **36**, 525–535. DOI: https://doi.org/10.1007/s11663-005-0044-x
9. *Nanda* Kishore, Sai Gu (2011) Momentum and heat transfer phenomena of spheroid particles at moderate Reynolds and Prandtl numbers. *Heat Mass Transfer*, 54(**11–12**), 2595–2601. DOI: https://doi.org/10.1016/j.ijheatmasstransfer.2011.02.001
10. Yang, C., Mao, Z. (2014) *Numerical simulation of multiphase reactors with continuous liquid phase*. Academic Press.
11. Kharicha, A., Karimi-Sibaki, E., Wu, M. et al. (2018) Review on modeling and simulation of electroslag remelting. *Steel Research Int*., 89(**1**).
12. Dudko, D.A., Rublevsky, I.N. (1961) About drop transfer of electrode metal in electroslag welding. *Avtomatich. Svarka*, **4**, 24–31 [in Russian].
13. Polishko, G., Stovpchenko, G., Medovar, L., Kamkina, L. (2019) Physicochemical comparison of electroslag remelting with consumable electrode and electroslag refining with liquid metal. *Iron Making & Steel Making*, 46(**8**), 789–793. DOI: https://doi.org/10.1080/03019233.2018.1428419
14. Klyuev, M.M., Volkov, S.V. (1984) *Electroslag remelting*. Moscow, Metallurgiya [in Russian].
15. Klyuev, M.M., Nikulin, A.A. (1970) Speed of movement and degree of heating of the metal drop in slag during electroslag remelting. *Bulleten TsNIICherMet.*, **4**, 32–34 [in Russian].
16. Schmehl, R. (2002) Advanced modeling of droplet deformation and breakup for CFD analysis of mixture preparation. In: *Proc. of ILASS-Europe 2002 (Zaragoza, 9–11 September, 2002)*.

ORCID

I. Krivtsun: 0000-0001-9818-3383,
V. Sydorets: 0000-0002-8498-4726,
G. Stovpchenko: 0000-0002-6555-5715,
G. Polishko: 0000-0001-7543-280X,
A. Sybir: 0000-0002-9974-0636,
L. Medovar: 0000-0003-2077-5965

CONFLICT OF INTEREST

The Authors declare no conflict of interest

CORRESPONDING AUTHOR

I. Krivtsun
E.O. Paton Electric Welding Institute of the NASU
11 Kazymyr Malevych Str., 03150, Kyiv, Ukraine.
E-mail: krivtsun@paton.kiev.ua

SUGGESTED CITATION

I. Krivtsun, V. Sydorets, G. Stovpchenko, G. Polishko, A. Sybir, L. Medovar (2022) Effect of deformation of molten metal droplets on their motion and heating in liquid slag. *The Paton Welding J.*, **6**, 41–48.

JOURNAL HOME PAGE

https://pwj.com.ua/en

Received: 07.07.2022
Accepted: 15.08.2022

https://doi.org/10.37434/tpwj2022.06.07

FEATURES OF ANALYSIS OF THE TECHNICAL STATE AND SUPPORT OF RELIABILITY OF THE MAIN GAS PIPELINES AT TRANSPORTATION OF GAS-HYDROGEN MIXTURES (REVIEW)

O.S. Milenin, O.A. Velykoivanenko, G.P. Rozynka, N.I. Pivtorak

E.O. Paton Electric Welding Institute of the NASU
11 Kazymyr Malevych Str., 03150, Kyiv, Ukraine

ABSTRACT

Analytical review of the features of operation, expert analysis of the technical state, and support of the reliability of the main gas pipelines at transportation of natural gas and hydrogen mixtures through them was performed. Proceeding from modern concepts of hydrogen degradation of pipe steels, conditions are considered which are required for safe use of the currently available gas transportation system for this purpose, in particular, with different hydrogen concentration in the mixture. Additional requirements were formulated as to evaluation of the acceptability of typical defects, and procedure of their repair by pressure welding methods.

KEYWORDS: gas-hydrogen mixture, main gas pipeline, hydrogen degradation, technical state, reliability, repair

INTRODUCTION

Use of hydrogen and other renewable gases as a mean of energy transfer from remote sources (first of all, solar and wind electric stations, biomaterial processing stations etc.) becomes more and more widespread, in particular, in scope of EU Hydrogen Strategy to 2050 adopted by European Committee [1]. It is caused by a series of factors of economical, ecological and technological nature, including intensive development of "green" energy. Thus, usage of "green" technologies for energy production is related with certain localizing of the energy generating capacities depending on their type (places of installation of large area solar panels, wind generators etc.), that requires solution of a problem of generated energy transportation to general networks. Construction of the new power lines requires significant financial expenses that increases total cost of "green" energy. Therefore, one of the possible ways of its transportation to the end user is usage of a branched gas pipeline system for transportation, first of all, of "green" hydrogen, generated by electrolysis of water or its other types, shown in Figure 1 [2, 3]. Such an approach is reasonable from point of view of higher efficiency of energy transfer in pipeline hydrogen transportation, increase of part of renewable energy in a general scope of power generating capacities, decrease of industry dependence on fossil hydrocarbons, in particular natural gas [4].

However, direct use of a gas transportation system (GTS) for hydrogen transportation is related with

Green hydrogen
- Green hydrogen is produced by the electrolysis of water;
- The process is powered by zerocarbon electricity (e.g., wind and solar power);
- It is clean, but is too expensive for widespread use;
- The cost of electrolysers and renewable energy is expected to fall over the next decade, making green hydrogen more viable;
- Green hydrogen is the ideal long-term, zero-carbon way to produce hydrogen

Blue hydrogen
- Blue hydrogen is produced from fossil fuels (typically natural gas), but emissions are dealt with using carbon capture and storage (CCS) technology;
- With abundant natural gas and coal available, blue hydrogen could help to scale the hydrogen economy, however, this is dependent on wider adoption of CCS;
- Blue hydrogen could act as a stepping stone from grey/brown to green hydrogen

Grey/brown hydrogen
- Grey hydrogen is typically produced from natural gas in a process called steam methane reformation;
- Brown hydrogen is produced from the gasification of coal;
- These are the strongly dominant methods in use today;
- They are relatively cheap, but emit large amounts of CO_2

Figure 1. Example of hydrogen classifying by the methods of its industrial production [2]

increase of the risks of accidents since design conditions of the main and distribution pipelines do not consider high concentration of this element in gas being transported from point of view of material selection, operation conditions, maintenance order. Use of the mixtures of natural gas and hydrogen [5–7] is reasonable for the purpose of utilization of existing GTS for hydrogen transportation without significant changes in the pipeline design. Negative effect of hydrogen on strength and performance of the pipeline can be allowable under condition of selection of specific concentration of hydrogen in such a gas-hydrogen mixture (GHM). Nevertheless, in selection of the operation parameters as well as sequence of technical diagnostics performance, analysis of technical state, maintenance of working capacity and guarantee of GTS reliability it is necessary to consider not only materials science aspects of hydrogen effect on the main gas pipeline (MGP) material, but also apply corresponding approaches of mechanical engineering. The latter allows considering the peculiarities of state of the main pipeline structural elements in transportation of GHM in context of corresponding standards and norms.

The aim of present review is a generalization of the data on peculiarities of operation, analysis and maintenance of MGP state and performance during transportation of natural gas and hydrogen mixtures.

PECULIARITIES OF HYDROGEN EFFECT ON THE MAIN GAS PIPELINE MATERIAL

It is known that steel of a buried gas pipeline can be hydrogenated from a pipe outer surface in the area of protective insulation damage due to soil corrosive effect as well as inner one due to electrochemical interaction of condensed moisture that contains hydrogen or as a result of dissociation of hydrogen gas [8]. The applied aspects of a hydrogen negative effect on mechanical properties of metals and long-term operation structures are under constant attention of the operating organizations of different branches of industry as well as research groups all over the world. This allowed determining and generalizing the nature of hydrogen damage of typical pipe steels, however, understanding of its mechanisms [9] is insufficient. Thus, hydrogen degradation of the steel properties depends on their strength. High-strength steels are more susceptible to hydrogen influence than low-strength ones at that change of elastic properties is insufficient, however, ductility, parameters of resistance to different types of failure (ultimate strength, fracture toughness, threshold of strength intensity factor, fatigue crack growth rate) can deteriorate with increase of hydrogen concentration [10].

It is known that an integral concentration of diffusion hydrogen is to some extent a qualitative indicator of a condition of material hydrogenation, because the more important factor is a localized concentration on a tip of already existing material discontinuity defects, where atomic hydrogen can recombine to molecular state [11]. The recombination results in a formation of high local hydrostatic pressure inside the traps that leads to increase of internal microstresses. This promotes formation and development of distributed damage of the material as well as macrodefects on different mechanisms [12–14], namely hydrogen stress cracking (HSC); hydrogen-induced cracking (HIC/HAC); stress oriented hydrogen-induced cracking (SOHIC); soft zone cracking (SZC); stepwise cracking (SWC); sulphide stress cracking (SSC); blistering; stress corrosion cracking (SCC).

The nature and scale of the negative effect of hydrogen depend on various factors, including composition of pipe steel, distribution and morphology of phases, grain structure, segregation and distribution of alloying elements and impurities. Therefore, to evaluate the reliability of MGP elements under conditions of GHM transportation it is necessary to consider separately the effect of excessive hydrogen saturation of assembly welds metal (WM) and heat affected zone (HAZ) on a limiting state of the pipeline under design load conditions. The results of experimental investigations of the specimens from WM, HAZ and pipe steel base metal showed that at different level of hydrogenation the most sensitive to negative effect of hydrogen is HAZ metal in which coarse grain columnar structure is formed [15]. At that the highest degradation is observed in the fatigue characteristics of HAZ metal, which should be taken into account when determining the possibility and conditions of GHM transportation via specific sections of GTS.

A special phenomenon, typical for long-term operation structures at transportation of the hydrogen-containing substances, is accumulation of material scattered damage [16, 17]. The process of accumulation of such type of damage (metal ageing) is divided on several steps [18]. Ageing, strength and hardness of metal rise in stage I and characteristics of ductility and brittle fracture resistance reduce. In stage II for determination of material ductile characteristics it is necessary to consider its actual net section. In this case opening of the multiple microdefects under tensile stress has a significant effect on the obtained results of laboratory experiments that results in an error during determination of actual ductility. The latter could also be a reason for decrease of strength and hardness of the material.

TYPICAL PROBLEMS FOR RELIABILITY ENSURING IN THE MAIN PIPELINES AT TRANSPORTATION OF HYDROGEN AND NATURAL GAS MIXTURES

The requirements to conditions of operation of the existing GTS of Ukraine are based on a complex of standards and norms that regulate different aspects of design, analysis of technical state and order of pipeline maintenance. Reprofiling main pipeline systems for GHM transportation requires consideration of the peculiarities of effect of hydrogen increased concentration on operation characteristics of GTS elements. So, it is established, that high hydrogen flowability, on the one hand, increases energy efficiency of GHM pumping and, on the other hand, provokes rise of a risk of transported gas leakage [19]. From point of view of pipeline integrity management the following reasons of local leakage appearance [20] are usually considered, namely corrosion damage; material defects; defects of technological nature; operation or design errors; distributed load, other loads, equipment malfunction etc.

The results of calculation of a risk factor (for different pipeline materials) and total risk (taking into account probability of appearance of critical situation) of accident due to leakage of transported GHM with different volumes of hydrogen content (0–50 %) (Table 1) show that the highest risks take place in the area of corrosion damages and technological defects (dents, bends, corrugations etc.) [21]. Technological defects that appear, in particular, during construction or technical works on separate sections of the pipelines at open excavations, do not virtually change in the process of pipeline operation in contrast to corrosion damages which are typical for GTS of Ukraine due to its general wear-out. Therefore, increase of corresponding risks by 15–20 % (at hydrogen concentration up to 20 %) has to be justified by additional calculations of the risks of a limit state of separate sections of pipelines with the detected defects of corrosion thinning for the moment of diagnostics as well as under conditions of defect development in process of MGP further operation. Excessive strength of a pipeline section with corrosion damages should be sufficient in order to compensate corresponding increase of the risks in GHM transportation. It should be noted that provided calculations consider different types of pipeline materials (pipe steel, polymers etc.), therefore these indices in relation to Ukrainian GTS are to be considered more as qualitative. However, they notably demonstrate effect of hydrogen of different concentration in GHM content on a tendency of the main pipelines to leakage failure.

The fact that most of the main pipelines lied under ground, to some extent, reduces the possible consequences of gas or GHM leakage. Nevertheless, analysis of the possibility of application of separate section of existing GTS requires consideration of a pipeline location in relation to other infrastructure objects such as residential houses, bridges, roads and railways, power supply networks etc. The construction standards [22], which determine the requirements to lying of main pipelines, include the dependencies of a distance from pipeline axis to an object of certain type depending on pipeline diameter and its class (see example Table 2). However, it is natural to expect that the fatal consequences of ignition or explosion of GHM (first of all, human casualties) are higher than in the case of natural gas. Therefore, it is necessary to formulate more rigid conditions as for mutual location of main or gas distribution pipeline and other objects or constructions.

The available results of investigation of a risk of fatal consequences of explosion of GHM with different concentration of hydrogen [21] showed that a typical peculiarity is increase of risks from accidents at more significant localizing of high risks to direct place of leakage. Thus, (as shown in Figure 2) at the distance around 265 m from the axis of pipeline with GHM leakage the risks of fatal consequences due to

Table 1. Calculated failure risk of MGP depending on failure nature and composition of gas-hydrogen mixture [21]

Accident reason	Probability, %	Risk factor, %				Total risk, %			
		Natural gas	<20 % H_2	20–50 % H_2	>50 % H_2	Natural gas	<20 % H_2	20–50 % H_2	>50 % H_2
Corrosion damage	36.42	24.54	29.54	29.54	44.54	8.94	10.76	10.76	16.22
Material defect	6.98	34.16	39.16	39.16	54.16	2.38	2.73	2.73	3.78
Distributed load	8.47	25.58	35.58	35.58	45.58	2.17	3.01	3.01	3.86
Defect of technological nature	15.39	50.00	60.00	70.00	70.00	7.69	9.23	10.77	10.77
Other load	1.86	10.00	15.00	15.00	30.00	0.19	0.28	0.28	0.56
Malfunction of equipment	6.75	30.00	35.00	35.00	50.00	2.02	2.36	2.36	3.37
Error in design or operation	2.53	30.00	35.00	35.00	50.00	0.76	0.89	0.89	1.27
Other	21.60	10.00	15.00	15.00	30.00	2.16	3.24	3.24	6.48
Total	100.00	214	264	274	374	26	33	34	46

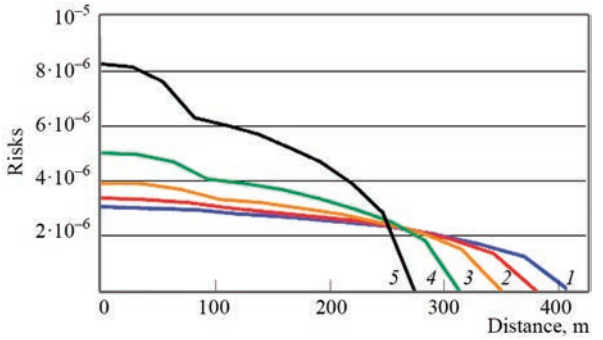

Figure 2. Dependence of risk (for 1 year) of fatal case as a result of accident on distance to pipeline (914 mm diameter, 7 MPa pressure) at different hydrogen concentration in GHM being transported: *1* — pure natural gas; *2* — 25 % of hydrogen; *3* — 50 % of hydrogen; *4* — 75 % of hydrogen; *5* — pure hydrogen [21]

ignition virtually do not depend on hydrogen concentration and equal that for natural gas, and at larger distances high volatility of hydrogen even reduces corresponding risks. However, for smaller distances it is necessary to introduce additional adjustments to existing requirements [22]. This additional adjustment to the distance for hydrogen concentration in GHM up to 25 % makes approximately 100 m, and at 50 % of hydrogen it is around 150 m. If location of the infrastructure objects on separate sections of the pipeline does not fulfil such more rigid requirements, direct usage of these sections for transportation of GHM without previous relocation of pipeline or protection of corresponding objects is unacceptable. The same conclusions should be used for parallel pipeline lines, that are located in the immediate proximity one from another as well as when planning laying of new MGP along the existing ones.

Special attention shall be given to the pipelines, where fatigue failure is possible, namely sections at the exist of compressor stations, underground, underwater or aboveground passages through natural and artificial barriers etc. It is known fact that conditions of increased hydrogen concentration provoke increase of material tendency to spontaneous development of fatigue cracks [23]. Therefore, in order to use these MGP sections for GHM transportation it is necessary to reduce a period of monitoring of their technical state for the purpose of detection of appearance of crack-like defects. This is in particular refers to the places of assembly and repair welding, where additional residual tensile stresses in a weld area and HAZ promote increased susceptibility to crack nucleation under conditions of external cyclic loading.

According to the requirements [22] main pipelines and their sections are divided on categories depending on conditions of laying, pipe dimension-type and operation parameters. Depending on the category of specific section (B, I, II, III, IV) the safety factors of operation conditions are determined in strength and resistance calculations, norms of amount of welded joins, that are subjected to non-destructive testing, testing parameters etc. In order to guarantee corresponding safety of pipelines in GHM transportation it is necessary to change the category of specific sections. In particular, it is related to aerial crossings and crossings through railway rails and roads as the places of increased danger. The standard [22] determines for this case an increase for one category and check of virtual correspondence of these sections to increased category.

PROCEDURE OF EVALUATION OF MAIN GAS PIPELINE TECHNICAL STATE TAKING INTO ACCOUNT INCREASED CONCENTRATION OF HYDROGEN IN A MIXTURE BEING TRANSPORTED

Periodic technical diagnostics of MGP state includes non-destructive testing activities, in particular flaw detection, and following expert analysis of corresponding bearing capacity of the specific sections to design conditions. The main scope of information on

Table 2. Example of reference distances from the axis of buried gas pipeline to different objects depending on class and diameter of pipe [22]

Objects, constructions, buildings	Minimum distance from gas pipeline axis, m							
	Pipeline class							
	I							II
	Nominal diameter of pipe, mm							
	< 300	300–600	600–800	800–1000	1000–1200	1200–1400	≤ 300	> 300
Cities and other settlements; separate industrial enterprises; separate buildings with mass accumulation of people; airports	100	150	200	250	300	350	75	125
Territories of gas-distribution stations	50	75	100	125	150	175	50	75
Mouths of oil, gas and artesian wells	30	50	100	150	175	200	30	50
General network railways	75	125	150	200	225	250	75	100

condition of kilometres-long sections of a linear part of pipelines is obtained based on the results of in-line inspection (ILI). It lies in running of series of pigs together with a product being transported [24, 25]. Today there is a wide spectrum of ILI tools which allow with sufficient accuracy to determine, measure and quantitatively evaluate defects of different type. Besides, in addition to increased danger of a flaw detector operation in a hydrogen medium, their application is related with the same complex of problems of negative effect of hydrogen on metal component properties that are typical for pipeline metal. Therefore, the flaw detectors used in GHM with hydrogen content more than 10 % should be made of materials with the highest resistance to hydrogen degradation. Also the negative effect of hydrogen on long-term integrity of constant magnets of rear-earth metals is known [25, 26]. It is necessary to be considered in usage of corresponding elements, in particular at magnetic flux leakage (MFL).

In case of detection of the discontinuity defects it is necessary to make a decision as for their allowability and planning the activities on restoration of bearing capacity of the pipeline. The allowability of defects (two-dimension — cracks, three-dimension — corrosion damages, shape defects etc.) of main pipelines in Ukraine is regulated with the reference document [27], which contains a complex of the requirements and algorithms of static strength calculation of the pipeline sections with certain type defects. Fields of application [27] allow its usage for evaluation of the gas pipeline state in GHM transportation, but this requires certain formal corrections.

Thus, comparison of the calculation and design values of the safety factor of pipeline specific section is used as a criterion of a limit state in static strength calculations. At that in accordance with the design requirements [22] the pipeline safety factor is determined, also, corresponding to a category of specific pipeline section, which, as was shown above, should be corrected in case of GHM transportation. Thus, the minimum allowable safety factor can also be recalculated that can change the conclusions as for bearing capacity of the defective pipeline section.

An expert conclusion as for allowability of certain found defect of MGP lies, in particular, in determination of this defect category, namely: minor, moderate, major, critical ones. Corresponding to a determined category it is recommended to carry out repair operations, decrease pressure of product being transported or limit an operational life with additional monitoring of a state of defective section every 6 or 2 months and once and twice a year. A period of the additional monitoring in case of GHM transportation can be changed due to insufficient information on intensity of defect development. A proof is necessary that for the specified period the natural increase of the defect will not result in change of its category.

A separate task of analysis of actual MGP state by flaw detection results is determination of its life. For this it is necessary to take into account the next damaging factors, namely degradation of mechanical properties of material, corrosion damage, stress-corrosion, cyclic loading.

Degradation of material properties from point of view of resistance to various types of failure under conditions of increased hydrogen concentration in the product being transported, on the one hand, requires the more conservative expert analysis of defect allowability and, on the other hand, needs a determination of time intervals of additional inspection or removal of found defects. As it was mentioned above, hydrogen has the largest effect on strength parameters (yield stress σ_y and ultimate strength σ_t), crack resistance (fracture toughness K_{Ic}, K_{Jc}) and fatigue strength (threshold value of stress intensity factor ΔK_{th}, fatigue crack growth rate da/dN). Specific current values of the indicated physical-chemical characteristics of pipeline material in the area of found defect are to be determined by means of performance of corresponding laboratory investigations with available samples of pipe metal that allows considering additional negative effect of hydrogenation in GHM transportation. However, performance of corresponding number of the laboratory tests is difficult to realize in practice, therefore, during calculations of static strength and life it is agreed to use certain conservative values of the corresponding parameters. Approaches recommended in [27] as for interpretation of the results of measurements of material hardness and its impact toughness for determination of current value of σ_y and σ_t (degradation can reach 10 %) as well as K_{Ic} (to 40 %) can be inapplicable in the case of significant development of scattered damage of pipe material as a result of its hydrogenation. Particularly, this should be expected for sections of the pipelines with high operating time, number of which is high in the Ukrainian GTS.

If the order of calculation of effect of defect corrosion development in GHM transportation is not changed in comparison with the conditions of natural gas pumping, than excessive content of hydrogen in the pipeline metal can significantly change metal tendency to nucleation of stress-corrosion cracks. The peculiarity of main stress-corrosion cracks is their elongation, which is caused by growth mechanism. Nucleation of such type cracks is multi-central with further coalescence of small cracks to the main one. This complicates detection of such type defects by

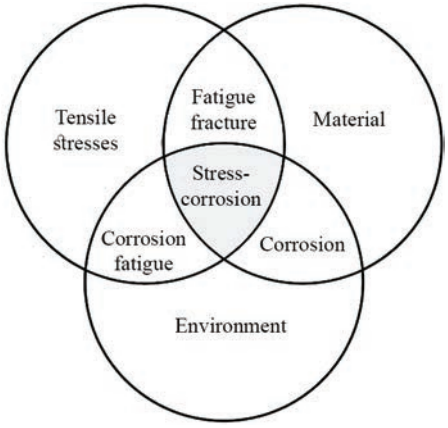

Figure 3. Conditional scheme of effect of interaction of different external factors on fracture mechanism of structural materials

means of express-monitoring, in particular ILI, therefore a prior determination of the pipeline sections having the highest tendency to stress-corrosion is important.

It is known that the necessary condition for nucleation of stress-corrosion cracks is simultaneous fulfilment of three conditions, namely tensile stresses higher that the threshold limit; sensitive metal structure; unfavourable corrosion medium (Figure 3) [28]. Each medium, which stipulates additional flow of hydrogen into metal and corresponding growth of microstresses in the areas of available discontinuities can result in stress-corrosion cracking. Therefore, determination of the possibility of application of the existing GTS for GHM transporting requires performance of the laboratory investigations of susceptibility of pipe metal of different sections to stress-corrosion damage.

If certain MGP section is subjected to effect of cyclic loads then in case of nucleation of fatigue cracks the life time of such sections is determined using crack resistance parameters as well as fatigue crack growth rate *da/dN*. The available results of investigations [29] show that in presence of hydrogen the typical pipe steels are characterized not only with rise of *da/dN,* but also with possibility of change of the failure nature (Figure 4) from intergranular to transgranular. So, in GHM transportation the frequency of technical diagnostics of such pipeline sections should be increase and conservativeness of the analysis of crack-like defects be higher.

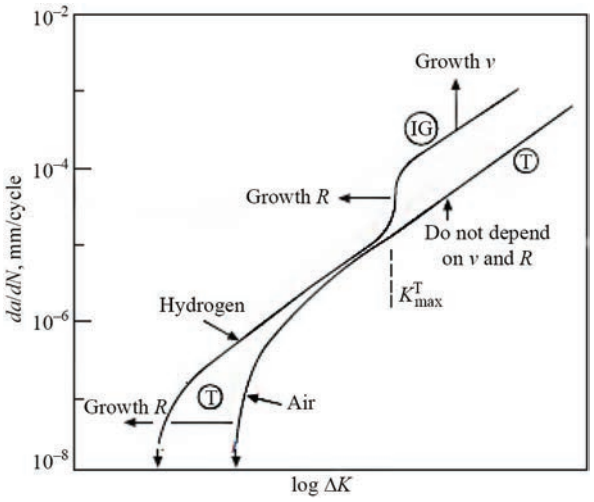

Figure 4. Schematic diagram of effect of hydrogen gas on fatigue crack growth rate in steels: *R* — coefficient of asymmetry of loading cycle; ν — loading frequency; T — mainly transgranular fracture; IG —mainly intergranular fracture [29]

APPLICABILITY OF REPAIR WELDING METHODS TO ELEMENTS OF MAIN GAS PIPELINES WITH DETECTED OPERATION DEFECTS IN GHM TRANSPORTATION

The methods of repair pressure welding [30] become more and more widespread in restoration of design strength and workability of MGP elements with discontinuity defects, which were determined during diagnostics. This allows increasing bearing capacity of the pipelines without a need of stop of product transportation reducing labour content as well as negative effect on environment. Performance of such repair is regulated by a series of standards, in particular [31]. The latter covers the sequence of evaluation of repair necessity, selection of its type depending on level of damage of specific pipeline section, sequence of selection of welding technological parameters etc. However, in case of GHM transportation and significant pipeline metal hydrogenation it is necessary to take into account specific features of MGP state.

First of all, any repair activity on the operating MGP should be preceded by investigation of possibility of hydrogen leakage that can result in explosion dangerous situation. Another factor, limiting application of repair welding technologies on operating pipelines is possible cold cracking of metal in welding area and occurrence of accident. It is known that formation of cold cracks on the specific sections of structure, being welded, needs simultaneously fulfilment of three conditions, namely presence of metal martensite structure, diffusion hydrogen and tensile stresses [32]. Therefore, in order to prevent appearance of cold cracks it is decided to eliminate additional inleak of hydrogen by means on preparation of place of welding and corresponding selection of filler materials as well as application of preheating in repair area at 100–150 °C level depending on pipe dimension-type, its strength and temperature of environment [31]. However, accelerated degradation of pipe metal properties in GHM transporting increases the susceptibility to cold cracking, therefore the recommendations to preparation of pipeline to repair have to be more rigid. Performance of such type of works at environment temperature lower than 0 °C and inten-

sive cooling of welding area can create unfavourable conditions as for tendency of metal structure to cold cracking. Besides, preheating temperature should be increased (to minimum allowable level 150 °C) and be maintained at each step of multipass repair welding or surfacing.

Presence of additional repair welds, which were made under field conditions, reduces life time of the pipeline in case of intensive hydrogen degradation of WM and HAZ [33]. Thus, in case of usage of the existing GTS for hydrogen transportation at its concentration in GHM more than 20 % the repair pressure welding should be considered, first of all, as temporary with next replacement of a repaired pipe spool in a period of planned shutdown of the pipeline section. A period, for which carried repair-restoration works guarantee corresponding pipeline reliability, are to be determined based on the results of prediction of long-term strength depending on operation conditions, actual state of pipe and repair type.

CONCLUSIONS

1. The paper provides a generalization of typical peculiarities of hydrogen effect on the main pipeline material from point of view of decrease of their design strength and operation life. It is shown that the hydrogen degradation of steel properties depends on their strength and the maximum negative effect is caused to ductility and resistance parameters to various fracture types. At that, the most significant metal degradation is observed in the areas of assembly welds, for which coarser microstructure is typical.

2. The typical problems were considered for providing the reliability of main pipelines in transportation of mixtures of hydrogen and natural gas. Based on the available data of the risk-analysis of MGP accident rate due to hydrogen leakage it is shown that its concentration up to 20 % in gas-hydrogen mixture being transported provokes notable increase of the risks due to leakages in the area of corrosion damages. Therefore, a decision making on possibility of application of the existing GTS should be based on the corresponding evaluation of actual defectiveness and proof of the required residual strength of pipelines with corrosion damage.

3. It is shown the need of overview of the categories of separate sections of MGP in case of transportation by them of GHM. In particular, it relates to aerial crossings through artificial and natural barriers as well as underground crossings through railway rails and roads, as places of increased danger, for which rise for one category is necessary.

4. The peculiarities of evaluation of pipeline technical state at consideration of increased hydrogen concentration in a mixture being transported were discussed. It is shown the necessity of clarification of a period of non-destructive testing taking into account more intensive influence of typical damaging factors in GHM transportation in order to guarantee the required static strength and service life of MGP. Besides, the methods of express-evaluation of actual properties of pipelines recommended by the existing reference documents are limitedly used in case of GHM transportation.

5. The analysis was carried out on applicability of the methods of repair pressure welding of gas pipelines in transportation by them of a mixture of natural gas and hydrogen. It is shown that the main technological task at that is a prevention of cold crack formation in hydrogenized pipe metal. It can be fulfilled by selection of the corresponding preheating temperature of a place of repair welding and more rigid requirements to allowable environmental temperatures. Moreover, presence of additional repair welds reduces general resistance of the pipeline to brittle and fatigue fracture that should be considered at its further operation.

REFERENCES

1. Golombek, R., Lind, A., Ringkjøb, H.-K., Seljom, P. (2022) The role of transmission and energy storage in European decarbonization towards 2050. *Energy*, **239**, Pt C, 122159. DOI: https://doi.org/10.1016/j.energy.2021.122159
2. (2022) *Rising to the challenge of a hydrogen economy. Report*. Norway, DNV.
3. Gondal, I.A. (2016) *Hydrogen transportation by pipelines. Compendium of hydrogen energy.* Vol. 2: Hydrogen Storage, Transportation and Infrastructure. UK, Woodhead Publ., 301–322. DOI: https://doi.org/10.1016/B978-1-78242-362-1.00012-2
4. Quarton, C.J., Samsatli, S. (2018) Power-to-gas for injection into the gas grid: What can we learn from real-life projects, economic assessments and systems modelling? *Renewable and Sustainable Energy Reviews*, **98**, 302–316. DOI: https://doi.org/10.1016/j.rser.2018.09.007
5. Melaina, M.W., Penev, M., Zuboy, J. (2015) *Hydrogen Blending in Natural Gas Pipelines*. Handbook of Clean Energy Systems. USA, John Wiley & Sons Ltd. DOI: https://doi.org/0.1002/9781118991978.hces205
6. Martin, M.L., Connolly, M., Buck, Z.N. et al. (2022) Evaluating a natural gas pipeline steel for blended hydrogen service. *J. of Natural Gas Science and Engineering*, **101**, 104529. DOI:https://doi.org/10.1016/j.jngse.2022.104529
7. Ishaq, H., Dincer, I. (2020) A comprehensive study on using new hydrogen-natural gas and ammonia-natural gas blends for better performance. *J. of Natural Gas Science and Engineering*, **81**, 103362. DOI: https://doi.org/10.1016/j.jngse.2020.103362
8. Nykyforchyn, H., Unigovskyi, L., Zvirko, O. et al. (2021) Pipeline durability and integrity issues at hydrogen transport via natural gas distribution network. *Procedia Structural Integrity*, **33**, 646–651.
9. Nechaiev, Yu.S. (2008) Physical complex problems of aging, embrittlement and fracture of metallic materials of hydrogen energy and main pipelines. *Uspekhi Fizicheskikh Nauk*, 178(**7**), 709–726 [in Russian].

10. Sun, Y., Cheng, Y.F. (2022) Hydrogen-induced degradation of high-strength steel pipeline welds: *A critical review. Engineering Failure Analysis*, **133**, 105985. DOI: https://doi.org/10.1016/j.engfailanal.2021.105985
11. Li, W., Cao, R., Xu, L., Qiao, L. (2021) The role of hydrogen in the corrosion and cracking of steels — a review. *Corrosion Communications*, **4**, 23–32. DOI: https://doi.org/10.1016/j.corcom.2021.10.005
12. Esaklul, K.A. (2017) *Hydrogen damage. Trends in oil and gas corrosion research and technologies production and transmission*. UK, Woodhead Publ., 315–340. DOI: https://doi.org/10.1016/B978-0-08-101105-8.00013-9
13. Zhou, D., Li, T., Huang, D. et al. (2021) The experiment study to assess the impact of hydrogen blended natural gas on the tensile properties and damage mechanism of X80 pipeline steel. *Inter. J. of Hydrogen Energy*, 46(**10**), 7402–7414. DOI: https://doi.org/10.1016/j.ijhydene.2020.11.267
14. Dmytrakh, I., Syrotyuk, A., Leshchak, R. (2022) Specific mechanism of hydrogen influence on deformability and fracture of low-alloyed pipeline steel. *Procedia Structural Integrity*, **36**, 298–305. DOI: https://doi.org/10.1016/j.prostr.2022.01.038
15. Kryzhanivskyi, Ye.I., Taraievskyi, O.S., Petryna, D.Yu. (2005) Influence of flooding on corrosion-mechanical properties of welds of gas pipelines. *Rozvidka ta Rozrobka Naftovykh i Gazovykh Rodovyshch*, 14(**1**), 29–34 [in Ukrainian].
16. Nykyforchyn, H., Lunarska, E., Tsyrulnyk, O.T. et al. (2009) Influence of service dispersed damage on regularities of degradation of structural steel properties. *Visnyk TDTU*, 14(**4**), 38–45 [in Ukrainian].
17. Nykyforchyn, H., Lunarska, E., Tsyrulnyk, O.T. et al. (2010) Environmentally assisted «in-bulk» steel degradation of long term service gas trunkline. *Engineering Failure Analysis*, 17(**3**), 624–632. DOI: https://doi.org/10.1016/j.engfailanal.2009.04.007
18. Kryzhanivskyi, Ye.I., Nykyforchyn, H. (2011) Peculiarities of corrosion-hydrogen degradation of steels of oil and gas pipelines and oil storage tanks. *Fizyko-Khimichna Mekhanika Materialiv*, **2**, 11–20 [in Ukrainian].
19. Doroshenko, Ya.V. (2020) Modeling of gas leakage from gas pipelines in emergency situation. *Visnyk VPI*, **3**, 22–28 [in Ukrainian]. DOI: https://doi.org/10.31649/1997-9266-2020-150-3-22-28
20. Li, X., Wang, J., Abbassi, R., Chen, G. (2022) A risk assessment framework considering uncertainty for corrosion-induced natural gas pipeline accidents. *J. of Loss Prevention in the Process Industries*, **75**, 104718. DOI: https://doi.org/10.1016/j.jlp.2021.104718.
21. Melaina, M.W., Antonia, O., Penev, M. (2013) *Blending hydrogen into natural gas pipeline networks: A review of key issues.* Technical Report. National Renewable Energy Laboratory, Denver West Parkway Golden, Colorado.
22. (2005) SNiP 2.05.06–85: *Main pipelines. Construction norms and regulations*. Moscow, FGUP [in Russian].
23. Murakami, Y. (2019) Hydrogen embrittlement. Metal fatigue. Effects of small defects and nonmetallic inclusions. Second Edition. USA. *Academic Press*, 567–607. DOI: https://doi.org/10.1016/B978-0-12-813876-2.00021-2
24. Xie, M., Tian, Z. (2018) A review on pipeline integrity management utilizing in-line inspection data. *Engineering Failure Analysis*, **92**, 222–239. DOI: https://doi.org/10.1016/j.engfailanal.2018.05.010
25. Barker, T. (2020) In-line inspection tool design and assessment of hydrogen pipelines. In: Proc. of *TDW — PPSA Seminar (17–18 November 2020, UK)*. Pigging Products & Services Association, 41–45.
26. Sagawa, M., Une, Y. (2022) *The status of sintered NdFeB magnets. Modern Permanent Magnets.* UK, Woodhead Publ., 135–168. DOI: https://doi.org/10.1016/B978-0-323-88658-1.00010-8
27. (2008) DSTU-N B V.2.3-21:2008: *Directive. Determination of residual strength of main pipelines with defects.* Kyiv, Ministry of Regional Development and Construction of Ukraine [in Ukrainian].
28. Raja, V.S., Shoji, T. (2011) *Stress corrosion cracking. Theory and Practice.* UK, Woodhead Publ.
29. Xu, K. (2012) Hydrogen embrittlement of carbon steels and their welds. *Gaseous Hydrogen Embrittlement of Materials in Energy Technologies*, **2**, UK, Woodhead Publ., 526–561.
30. Milenin, A.S. (2013) On planning of repair of pressurized main pipelines based on the results of in-pipe diagnostics. *The Paton Welding J.*, **5**, 29–38 [in Ukrainian].
31. (2011) GBN V.3.1-00013741-12:2011: *Main pipelines. Arc welding repair in service conditions.* Kyiv, PWI [in Ukrainian].
32. Makhnenko, V.I., Milenin, A.S., Olejnik, O.I. (2011) Current problems of repair of overland main pipelines without taking them out of service. In*: Proc. of Sci.-Techn. Seminar on Assurance of Service Reliability of Pipeline Transportation Systems (Kyiv, Ukraine, 10–11 June 2011).* PWI, 13–20 [in Russian].
33. Petryna, D.Yu., Kozak, O.L., Petryna, Yu.D. (2013) Corrosion-mechanical properties of main pipeline welded joints. *Rozvidka ta Rozrobka Naftovykh i Gazovykh Rodovyshch*, 46(**1**), 37–49 [in Ukrainian].

ORCID
O.S. Milenin: 0000-0002-9465-7710

CONFLICT OF INTEREST
The Authors declare no conflict of interest

CORRESPONDING AUTHOR
O.S. Milenin
E.O. Paton Electric Welding Institute of the NASU
11 Kazymyr Malevych Str., 03150, Kyiv, Ukraine.
E-mail: asmilenin@ukr.net

SUGGESTED CITATION
O.S. Milenin, O.A. Velykoivanenko, G.P. Rozynka, N.I. Pivtorak (2022) Features of analysis of the technical state and support of reliability of the main gas pipelines at transportation of gas-hydrogen mixtures (Review). *The Paton Welding J.*, **6**, 49–56.

JOURNAL HOME PAGE
https://pwj.com.ua/en

Received: 07.04.2022
Accepted: 15.08.2022